Large Eddy Simulation Studies of Island Effects in the Caribbean Trade Wind Region

Von der Fakultät für Physik und Geowissenschaften
der Universität Leipzig
genehmigte
DISSERTATION
zur Erlangung des akademischen Grades

DOCTOR RERUM NATURALIUM
(Dr. rer. nat.)

vorgelegt
von Diplom-Meteorologe Michael Jähn
geboren am 11. Mai 1986 in Marienberg

Gutachter: Prof. Dr. Ina Tegen
Prof. Dr. Bjorn Stevens

Tag der Verleihung: 21. März 2016

Bibliographische Beschreibung

Jähn, Michael

Large Eddy Simulation Studies of Island Effects in the Caribbean Trade Wind Region

Universität Leipzig, Dissertation

165 Seiten, 63 Abbildungen, 17 Tabellen, 119 Literaturangaben

Referat

In dieser Dissertation wird das kompressible, nicht-hydrostatische und dreidimensionale Modell *All Scale Atmospheric Model* (ASAM) für Grobstruktur- bzw. Large-Eddy-Simulationen (LES) angewendet, um lokale Inseleffekte in der karibischen Passatwindzone zu untersuchen. Da das Modell bis dato noch keine Anwendung im Bereich von LES feuchter atmosphärischer Grenzschichten und heterogener Oberflächen fand, wurden einige Bestandteile zum Modellcode hinzugefügt oder überarbeitet. Ein Hauptaugenmerk liegt dabei auf das Einbeziehen orographischer Strukturen mittels angeschnittener Zellen (engl. *cut cells*). Sowohl die räumliche und zeitliche Diskretisierung der Modellgleichungen als auch die nötigen physikalischen Parameterisierungen werden in einer umfassenden Modellbeschreibung zusammengefasst. Die Robustheit und Stabilität der Modellformulierung wird durch eine Reihe von Simulationen idealisierter Testfälle bestätigt.

Large-Eddy-Simulationen werden für das Gebiet der Karibikinsel Barbados zur Untersuchung von Inseleffekten bezüglich Grenzschichtmodifikation, Wolkenbildung und vertikaler Durchmischung von Aerosolen durchgeführt. Durch das Vorhandensein einer topographisch strukturierten Inseloberfläche in der Mitte des Modellgebietes muss das Modellsetup offene seitliche Randbedingungen beinhalten. Damit das einströmende Windfeld konsistent mit der Dynamik einer turbulenten, marinen Grenzschicht ist, wird eine neue Methode implementiert und angewendet, welche auf Störungen des potentiellen Temperaturfeldes mittels finiter Amplituden basiert.

Beobachtungen aus der SALTRACE-Messkampagne werden benutzt, um die Modellläufe anzutreiben. Die Ergebnisse einiger Sensitivitätstests zeigen Probleme der Modellierung im Bereich der „Terra incognita“ auf. Dabei handelt es sich um die Modellierung auf räumlichen Skalen, welche zwischen denen von LES und wolkenauflösenden Modellen liegen. Außerdem werden Auswirkungen von entweder turbulent oder laminar anströmenden Windfeldern auf die Simulationsergebnisse untersucht. Besonders die Wolkeneigenschaften im Lee von Barbados werden in diesen Simulationen merklich beeinflusst. Ergebnisse einer weiteren Simulation mit einer sehr starken Passatinversion bringt deren Einfluss auf die Dicke und Höhe der simulierten Wolkenschichten zum Vorschein. Die Veränderung von Saharastaubschichten, welche Barbados über weiträumigen Transport über den Atlantik erreichen, wird analysiert. Die Auswirkungen beinhalten sowohl eine Ausdünnung und ein Absinken dieser Schichten als auch turbulenter Transport in Richtung Erdoberfläche. Die genaue Position der beeinflussten Schichten und die Stärke des turbulenten Mischens werden hauptsächlich von der atmosphärischen Schichtung, der Inversionsstärke und Windscherung gesteuert. Vergleiche zwischen den LES-Modellergebnissen und Daten aus Doppler-Windlidarmessungen zeigen gute Übereinstimmungen in der Formierung der konvektiven Strukturen tagsüber und des Vertikalwindfeldes.

Abstract

In this thesis, the fully compressible, three-dimensional, nonhydrostatic atmospheric model called All Scale Atmospheric Model (ASAM) is utilized for large eddy simulations (LES) to investigate local island effects at the Caribbean. Since the model has not been applied to LES for moist boundary layers and heterogeneous surfaces so far, several parts are added to the model code or reworked. A special focus lies on the inclusion of orographical structures via the cut cell method. Spatial and temporal discretization as well as necessary physical parameterizations are summarized in a thorough model description. The robustness of the model formulation is confirmed by a set of idealized test case simulations.

Large eddy simulations are performed for the area of the Caribbean island Barbados to investigate island effects on boundary layer modification, cloud generation and vertical mixing of aerosols. Due to the presence of a topographically structured island surface in the domain center, the model setup has to be designed with open lateral boundaries. In order to generate inflow turbulence consistent with the upstream marine boundary layer forcing, the newly developed cell perturbation method based on finite amplitude perturbations is applied.

Observations from the SALTRACE field campaign are used to initialize the model runs. Several numerical sensitivity tests are carried out to demonstrate the problems related to “gray zone modeling” beyond LES scales or when the turbulent marine boundary layer flow is replaced by laminar winds. Especially cloud properties west of Barbados (downwind) are markedly affected in these simulations. Results of an additional simulation with a strong trade-wind inversion reveal its effect on cloud layer depth and height. The modification of Saharan dust layers reaching Barbados via long-range transport over the North Atlantic is analyzed. Effects of layer thinning, subsidence and turbulent downward transport near the layer bottom become apparent. The position of these layers and strength of downward mixing is found to be mainly controlled atmospheric stability, inversion strength and wind shear. Comparisons of LES model output with wind lidar data show similarities in the formation of the daytime convective plume and the vertical wind structure.

Contents

Chapter 1

Introduction

1.1 Motivation

The understanding of the interaction between a topographically structured island, trade winds, the trade inversion layer and daytime dependent heating is a very challenging topic in boundary layer (BL) meteorology. One example of these kinds of “island effects” is a leeward updraft zone, which is commonly visualized by satellite imagery in the shape of cloud streets or atmospheric wakes. In the latter case, island mountains act as mechanical obstacles and cause a significant flow distortion, which is sometimes manifested as impressive-looking van Kármán vortex streets. The effects of islands on meteorological parameters like atmospheric stability, dynamics, cloud properties or turbulence are often difficult to detect with measurements because of a) the presence of synoptic disturbances in the course of the days or b) the need of covering a wide spatial area mostly the over ocean surface. For that reason, numerical models are essential tools to improve the understanding of these effects. Island-induced clouds, even originating from small and flat islands, result in an enhancement of vertical heat and moisture exchange and can cause severe rainfall events in extreme cases. Considering a string of islands (e.g., Hawaiian Islands) where, depending on wind strength and direction, a one-sided influence of a windward island on another one can occur. There, the local weather and even climate statistics due to modified temperature, precipitation and wind regimes can be affected. These effects can hardly be simulated operationally used weather forecast models and have therefore to be investigated with fine-scale models. Island effects also play a role for measurements that are conducted on islands, both long-term observations and field campaigns. Due to the fact that it is easier to deploy measurement devices on land rather then over the ocean, the location issue has to be well thought out. Once the measurement system is set up at a certain site, island effects have to be taken into consideration when evaluating and interpreting the observational data.

Since the main drive of island effects is the daytime solar heating, the term *heat island* becomes handy regarding the island effect issue. However, this term is widely used in urban meteorology, especially in the context of the *urban heat island* (UHI) effect, which describes the problem of developing urban areas connected with rising temperature spots compared to their rural area (e.g., Oke, 1973; Sodoudi et al., 2014). Nevertheless, cities as well as oceans island create their own circulation patterns, which are related to the size of the city or island (Garstang et al., 1975). It is interesting to note that these two different research subjects have several aspects in common.

Returning to the original topic of island effect studies in the trade wind regime, the next sections provide a brief overview of the most important notions and processes. They include the concepts of internal boundary layers as well as a more detailed look into island effects on boundary layer dynamics and meteorology. After that, the basics of the used numerical technique are presented, followed by the main objectives of this thesis.

1.2 Internal boundary layers

The earth surface acts as the lower boundary of the atmospheric system. After Stull (1988), the *atmospheric* or *planetary boundary layer* (ABL, PBL) can be defined as the part of the troposphere that is directly influenced by the earth surface, including its forcings and interactions. With the assumption of a flat and horizontally homogeneous bottom boundary and stable atmospheric conditions without synoptical disturbances (e.g., at high-pressure systems), there is a well-defined boundary layer structure that evolves with the diurnal cycle (Fig. 1.1). This BL structure consists of three main components: the turbulent *mixed layer*, the *residual layer* and the *stable boundary layer*. The mixed layer is mainly convectively driven and capped by the stable entrainment zone at its top. But also wind shear near the top of the mixed layer contributes to turbulence generation. Shortly before sunset, turbulence in the mixed layer starts to decay due to the absence of convective forcing from the ground and the resulting layer is called residual

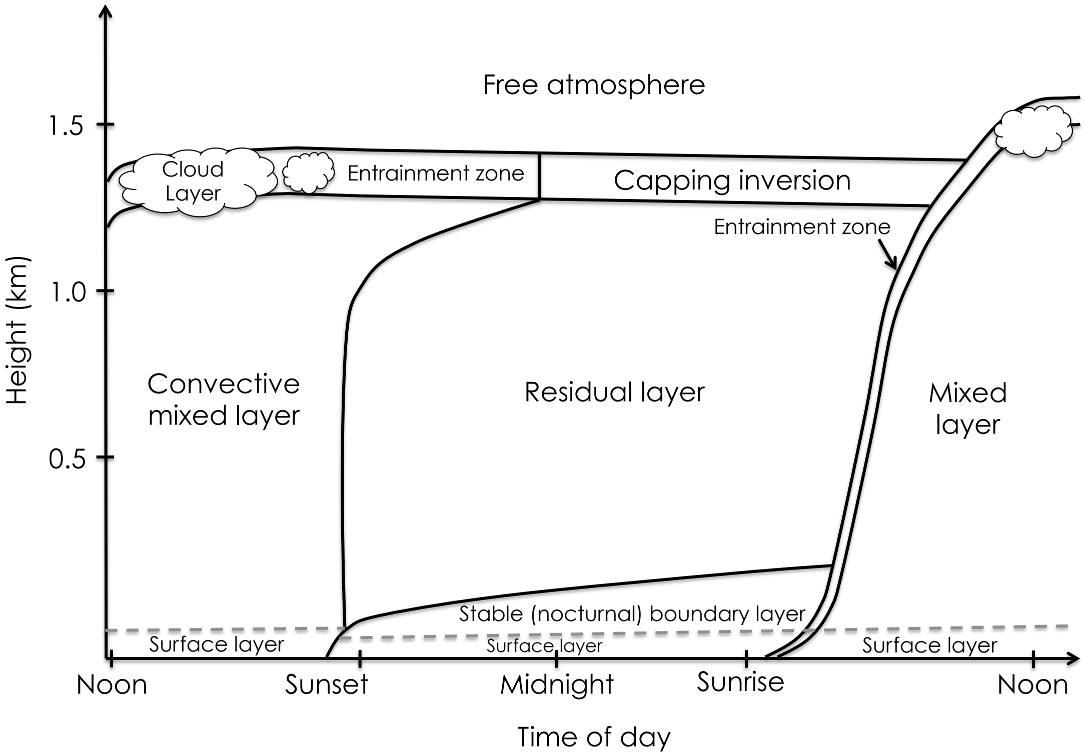

Figure 1.1: Idealized depiction of an undisturbed diurnal boundary layer development over land surface. The boundary layer consists of three major parts: a turbulent (convective) mixed layer, a less turbulent residual layer with former mixed-layer air and a stable (nocturnal) boundary layer with sporadic turbulence. The mixed layer is further divided into a cloud layer and a subcloud layer. Adopted from Stull (1988).

layer. This layer does not have direct contact to the ground because the nocturnal stable boundary layer develops and is characterized by statistically stable air and weak turbulence. However, winds aloft can become supergeostrophic, which is commonly denoted to *nocturnal* or *low-level jets*.

While these idealized concepts help to understand and classify BL structures, the real earth surface is not homogeneous but rather dominated by geographic variations. These variations include different topographic features as well as land-use characteristics. Considering a mountain slope for example, air adjacent to the mountain can be warmed or cooled by radiation and thus has a different temperature compared to ambient air over a valley at the same altitude. Then, the buoyant forces create a circulation pattern. The same effect can occur over flat surfaces with different albedos (i.e., the ratio of reflected flux density to incoming flux density) or heat capacities (Stull, 1988). The problems of separating these effects in a real environment are that they can a) interact with each other and b) be modified or even eliminated by mesoscale or synoptic circulations.

A more concrete example of circulations as a result of different surface characteristics are sea breezes. After the nocturnal BL is eliminated during the morning, rising air parcels develop over the heated land mass while cooler air from the sea flows in to replace it. This low-level convergence together with a marked temperature drop, a moisture increase and upward motion are related to the so-called sea-breeze front. The circulation is closed by the anti sea-breeze in higher altitudes, where the warm air is laterally transported over the sea and descends toward the sea surface. Again, this circulation pattern can be modified or totally eliminated by synoptic winds. In the case of moderate background winds, another type of BL can be formed when surface heat flux differences between neighboring surfaces are present: the *thermal internal boundary layer* (TIBL). It develops when an isolated island is heated by radiation and the air flows from a cooler (ocean) to a warmer (island) surface. More details about this particular boundary layer type and subsequent effects are subject to the next section.

1.3 Island effects on boundary layer dynamics and meteorology

The term "island effect" refers to every change of the boundary layer state of the surrounding area. The exact physical mechanisms are depending on the size and the height of the island. For that reason, Matthews et al. (2007) appointed three types of circulation patterns associated to islands.

1. **Tall islands.** Mountains with highest elevations $> 1\,\text{km}$ serve as mechanical obstacles, generating a wake and thus dominating the downwind flow characteristics. Examples: Hawaii, Dominica, St. Vincent.
2. **Large islands.** Islands with $> 40\,\text{km}$ in diameter that are in low-wind speed regimes generate their own mesoscale convection of the island area, which is driven by the convergence of coastal sea-breezes. Examples: Tiwi Islands,

Puerto Rico.

3. **Small islands.** Islands with smaller diameter and stronger winds than those of the large island category do not generate proper sea-breezes but may rather produce convective clouds connected with long plumes. Examples: Nauru, Barbados.

A conceptual model of island effects valid for small islands is presented in Figure 1.2. During daytime, solar radiation heats the interior of the island. Rising air starts to form low and shallow cumulus clouds, which continue to develop, travel offshore with the wind and can develop into a cloud street (Long and McFarlane, 2012). Being embedded into the (neutrally stratified) marine boundary layer, the island forms its own TIBL. Besides turbulence that is generated by the diurnal heating, topographical structures can lead to a further enhancement of turbulence. Moreover, the leeward flow is distorted due to different heating intensity and different surface roughness. The downwind convective plume narrows and decouples from the surface with increasing distance to the island.

There are several works regarding the understanding of airflow and thermodynamic quantities around Barbados. A first detailed observational study using pilot balloon measurements was done by DeSouza (1972) and further interpreted by Garstang et al. (1975). DeSouza's calculated vertical wind velocity fields showed a daytime divergence and nighttime convergence over the island. Mahrer and Pielke (1976) did a series of two- and three-dimensional numerical studies and found that DeSouza's calculations only hold for a flat island, because he neglected significant effects of terrain slope in his divergence calculations. Taking the topographical structures into account, Mahrer and Pielke (1976) pointed out some main characteristics, e.g., diurnal changes in the vertical wind velocity fields downwind (i.e., west coast of Barbados) with sinking motions over the center and western part of the island and an upwind cell off the west coast. Considering numerical sensitivity studies by Savijärvi and Matthews (2004, SM04 hereafter), the general conclusion was that these forced rising and sinking motions and their consecutive effects can only be explained if island orography is included in the numerical models. In their 2D study, SM04 added a 200-m-high central mountain to a 20 km wide island and showed that see-breeze circulations are enhanced by upslope winds during the day. These topographically forced components will dominate if the large-scale mean geostrophic wind is in the order of magnitude of at least 10 m s^{-1}, which is the case for Barbados. Smith et al. (1997) assigned different island structures

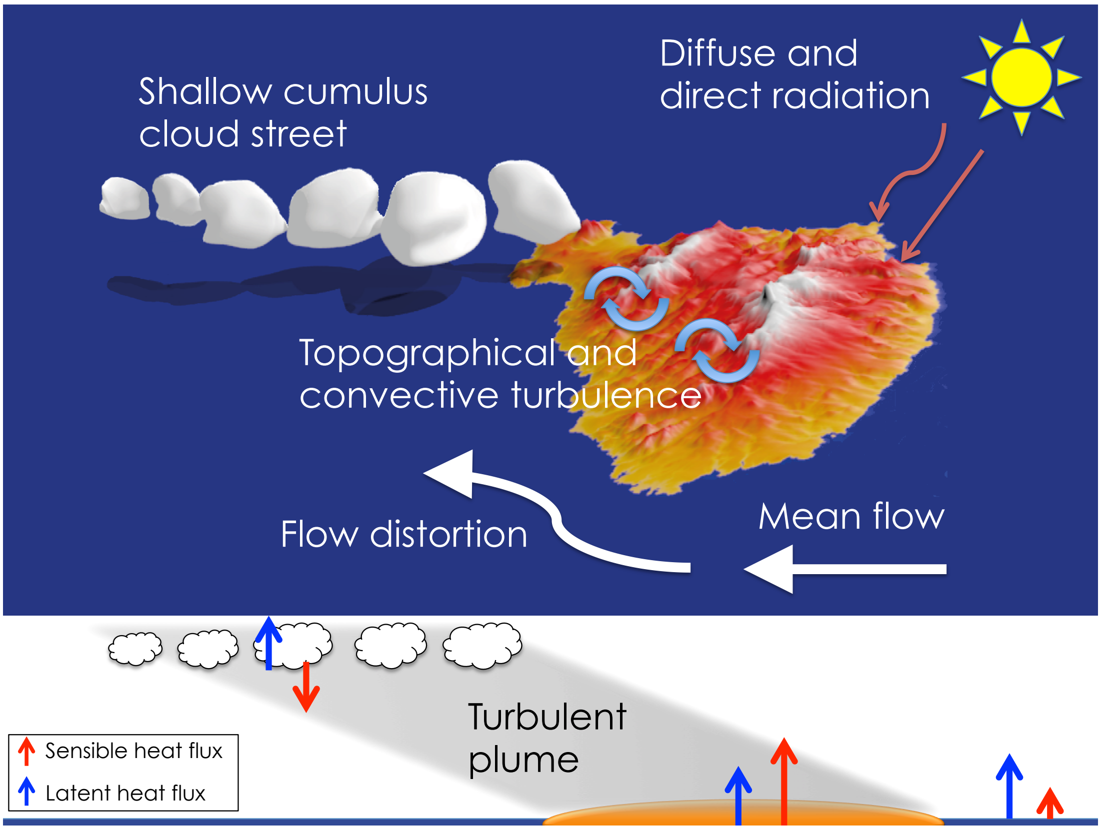

Figure 1.2: Conceptual model of meteorological effects around and isolated island. Top panel: three-dimensional sketch showing the most important processes related to island effects. Daytime solar radiation induces heating of the island surface and triggers convective turbulence. Rising air causes the formation of shallow cumulus clouds that can develop into a cloud street. Bottom panel: vertical cut plane with strongest turbulent activity along the cloud street. Different sensible (red arrows) and latent (blue arrows) heat fluxes at the island and ocean surfaces and at cloud base are shown. The lengths of arrows indicate the heat flux intensities.

to different mountain wake types. Since the highest elevation of Barbados, Mt. Hillaby with 340 m asl (above sea level) does not exceed the critical height for wave breaking, no wind wake can develop. However, a long trail of cumulus clouds extending westwards can evolve during the afternoon hours (cumulus cloud street). Kirshbaum and Fairman (2015) found that surface fluxes control the downwind circulation strength and the trade inversion controls precipitation and thus the disruption of cloud trails. Other influence factors like terrain height, wind speed and their interactions have multiple impacts on flow regimes, turbulence, cloud trail lengths etc. Another study on island effects with similar topographical heights compared to Barbados has been done by Minda et al. (2010). They investigated the evolution of the convective boundary layer (CBL) above Okinawa Island, Japan. It was found that for a flat island simulation, the warmed land already induces a distinct roll cloud that is in agreement with the observations. However, the inclusion of island terrain leads to a reinforced moisture uplifts, which in turn induce strong convection that can penetrate into the free atmosphere. Idealized numerical studies have been conducted by Kirshbaum and Grant (2012) to investigate the impact of mesoscale ascent (with an island height of 500 m) on cumulus convection. A particular important process with regard to the mean horizontal cloud size has been found. The broader the clouds are, the lower is the fractional entrainment rate in these clouds, which in the end leads to an increase in precipitation rates downstream. A key result from another combined theoretical and numerical study by Kirshbaum and Wang (2014) was that nonlinear interactions between mechanical and thermal flow over taller mountains were significant and thus lead to a strengthening of the lee-side convergence band. Heat island effects on vertical mixing of aerosols at Cape Verde islands were studied by Engelmann et al. (2011) using aircraft lidar measurements and idealized large eddy simulations (LES) with flat island surfaces. They found indications that the differential heating and the orographic impact control downward mixing of African aerosols, which results in a complex vertical layering over the Cape Verde region.

There are also many studies where the focus lies on the orographic influence of tall islands (e.g., Hawaii Island or Dominica with mountain heights above 1 km) on the leeward flow and precipitation patterns. Esteban and Chen (2008) state that for a strong trade wind flow, the daily rainfall totals at the windward side of the island of Hawaii show a nocturnal maximum due to the convergence of katabatic flow, whereas for weak trades ($\leq 5\,\mathrm{m\,s^{-1}}$) the rainfall amounts have its maximum in the late afternoon due to anabatic winds. In a work by Smith et al. (2009), orographic precipitation for the Caribbean island Dominica was studied. There, the conditionally unstable trade wind layer together with terrain-forced lifting leads to convective triggering over the windward slope. The reduced instability on the leeward side destroys convective clouds and creates a rainless area. A complementary study with airborne observations and cloud-resolving modeling for the same island was performed by Minder et al. (2013). The comparison showed that the dynamical structures are very well reproduced but it was difficult to reproduce of the observed rainfall by the model. Overall, mesoscale flow controls convection and rainfall over Dominica. At lower wind speeds, the circulations seem to be more thermally driven by solar heating.

1.4 Large eddy simulation technique

To model the complex internal BL structures and island effects, it is advisable to utilize large eddy simulations. To understand the meaning of this modeling technique, Fig. 1.3 shows the transition of the energetic mean flow to large eddies yet to even smaller eddies down to the molecular scale. This transfer of energy is also known as *energy cascade*, which is solely observed in small scale motion. To get a better idea of the particular scales and to describe the energy cascade more mathematically, Fig. 1.4 shows a schematic *turbulence spectrum* of the kinetic energy of atmospheric motion, where the different magnitudes of atmospheric turbulence are displayed. The energy spectrum can be related to certain time periods τ (or frequencies f) or wavelengths L (or wavenumbers k). Note that temporal and spatial scales can be connected using the Taylor hypothesis. A motion process with the time period τ is related to a length scale L by the mean wind speed $\overline{u}$:

$$L = \overline{u}\tau. \tag{1.1}$$

The maximum in the energy spectrum corresponds to energy production due to mechanical turbulence (i.e., wind shear in the BL) and thermal convection. Going toward smaller scales, there is a nearly constant slope in the *inertial subrange*. This part of the spectrum can be derived by theoretical considerations and observed by high-frequent measurements. It known as Kolmogorov's similarity hypotheses where the spectral energy density $E(k)$ follows a 5/3-law (Etling, 2008):

$$E(k) \propto k^{-5/3}\,. \tag{1.2}$$

In LES, the first part of the inertial subrange is directly resolved. The limiting factor

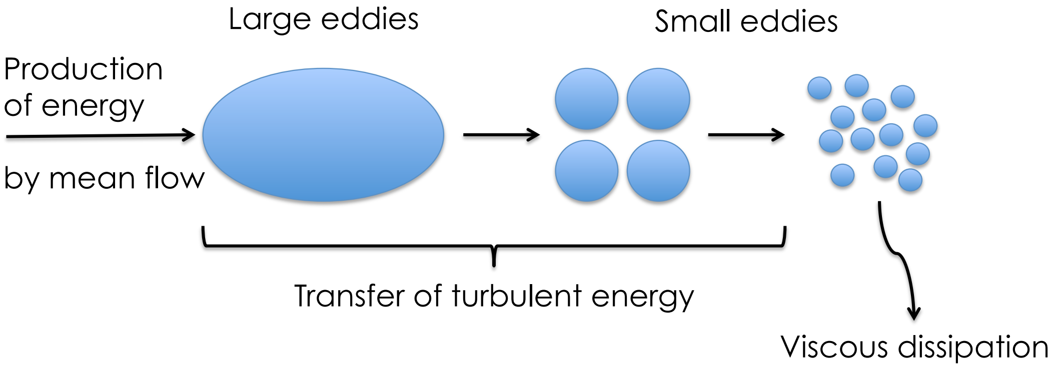

Figure 1.3: Illustration of the energy cascade. Kinetic energy is extracted from the mean flow and transformed into turbulent energy in terms of smaller scales eddies. Modified after Etling (2008).

here is the used grid spacing Δ of the model with the corresponding wavenumber k_Δ. The other missing part of the spectrum has be modeled by applying a spatial filter. The effect of the small scales on the larger scales are represented by subgrid scale (SGS) models, which serve as a turbulence closure. Details on the model equations, spatial filtering and the SGS parameterization will be shown in Chapter 2.

It is noteworthy that the LES modeling technique is not limited to only atmospheric problems. Deardorff (1972) extended LES to engineering plane channel flow. Since then, it has been employed as a useful tool to solve problems in engineering fluid dynamics (e.g., Galperin and Orszag, 1993; Lesieur et al., 2005).

There are several challenges when applying LES to atmospheric flows over complex terrain and inhomogeneous surface characteristics. To accommodate the real and complex terrain, the range of scales has to be expanded, which often requires a coarser resolution than in traditional LES studies. In this context, 'traditional' means idealized simulations with periodic boundary conditions of flat, homogeneous surfaces. Initially, the SGS models were not designed for this range of scales. However, the fundamental equations for LES are theoretically applicable at all scales (Chow et al., 2013). Further issues with open boundary conditions and the behavior of a 'realistic' development of turbulence in these kinds of LES setup have to be addressed and are thus further subject of this thesis.

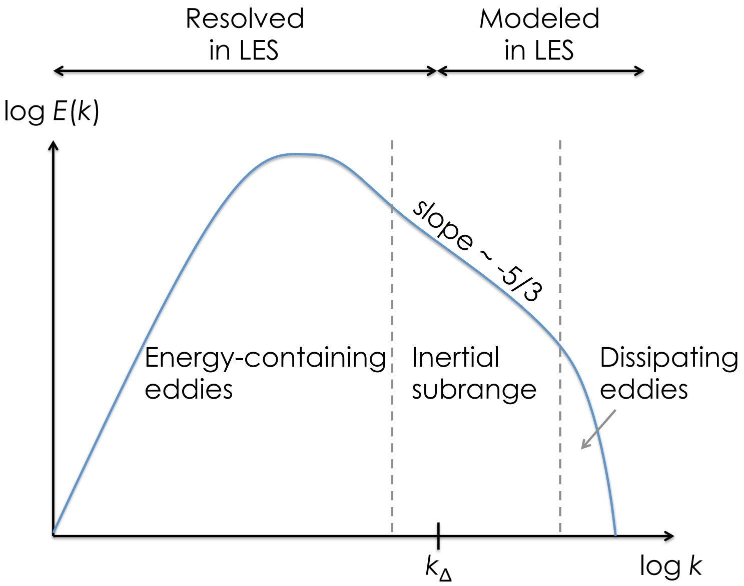

Figure 1.4: Schematic turbulence spectrum as spectral Energy E over the wavenumber k. Here, k_Δ denotes the wavenumber corresponding to the LES grid spacing Δ, which separates the resolved from the modeled scales.

1.5 Objectives of this thesis

The present dissertation mainly reflects the two major parts of the work:

1. **Model development.**
   An existing numerical code is taken up and further developed to obtain necessary features for the given atmospheric problem. This includes adding new and editing existing modules as well as testing, verification and documentation. For that reason, an extensive model description is presented, covering all relevant information that are necessary for the application of the model.

2. **Model application.**
   The model is applied to a well-defined question in the field of atmospheric research. In particular, a detailed analysis of local island effects at Barbados with LES is carried out.

In connection with the island effect analysis, the main interest is to gain an improved insight into the modification of the boundary layer structure, microphysical properties and downwind vertical mixing of aerosols. Regarding aerosols, especially Saharan dust, it is known from several studies that notable amounts of mineral dust reach Barbados via long-range transport over the North Atlantic, e.g., from first observations at the end of the 1960s (Prospero et al., 1970; Prospero and Carlson, 1970) or from back-trajectory calculations by Ellis and Merrill (1995). Within this work, the following scientific questions are addressed:

- How has the LES model setup to be chosen to get an as realistic as possible representation of an island-ocean-system in the trade wind regime through the example of Barbados?
- Can the inland-induced change of relevant meteorological parameters be quantitatively recorded and evaluated?
- How do turbulent inflow characteristics, grid spacing, surface characteristics and different background states affect the simulation results?
- Can the daytime convective island boundary layer explain downward mixing of low-altitude Saharan dust layers?
- Are the simulation results comparable with lidar measurements over and in the lee of the island?

This thesis is structured as follows. In Chapter 2 the numerical model for which all simulations are carried out is described, including numerics and discretization as well as physical parameterizations. Results of idealized test cases demonstrate the capability of the model to produce reasonable and comparable results for simulating different atmospheric flow problems. Chapter 3 describes the Saharan Aerosol Long-range Transport and Aerosol-Cloud-Interaction Experiment (SALTRACE), which consists of altogether three measurement campaigns in 2013/2014. There, observational data has been obtained that is used for model initialization and comparisons as well. Marine boundary layer simulations of shallow cumulus convection are performed in Chapter 4, followed by the results of the SALTRACE simulations as well as their discussion and interpretation in Chapter 5. This dissertation concludes with a summary and an outlook for possible future work including development and application in Chapter 6.

Chapter 2

The All Scale Atmospheric Model (ASAM)

2.1 Overview

The All Scale Atmospheric Model (ASAM) is a numerical code that has been developed at the Leibniz Institute for Tropospheric Research, Leipzig. To summarize the main features of the model, the different parts of its name are described in the following:

1. **All scale.** The model can be used with Cartesian, spherical or cylindrical grids with grid spacings ranging from the micro- to the macroscale.
2. **Atmospheric.** The equations are valid for a moist atmosphere and were derived from fundamental thermodynamic concepts. A set of physical parameterizations is implemented, which is necessary to describe the most relevant processes in the atmosphere.
3. **Model.** Spatial discretization is a mixture of finite volumes and finite differences. Structures and orography can be represented by cut cells. Different state-of-the-art time integration schemes are available and well coordinated with the spatial discretization concept.

ASAM was initially designed for computational fluid dynamics (CFD) simulations around buildings. For that reason, the grid structure had to be adapted to represent any kinds of obstacles, structures and topography. Thus it was appropriate to use the so-called cut (or shaved) cell method where the respective cells are directly intersected. Advantages and disadvantages of this approach will be discussed in Section 2.3.1. The model has been used as a research code and was further developed in the course of time. Evolving from a CFD code to an atmospheric model, the fundamental Euler equations had to be extended in a way that they are valid for a moist and cloudy atmosphere. By now, the user is able to choose between a large number of different options like numerical methods (e.g., split-explicit Runge–Kutta or partially implicit peer schemes), number of prognostic variables, physical parameterizations or the change to a spherical grid type, to name a few examples. With these features, large eddy simulations with spatial resolutions of $\mathcal{O}(1\text{-}100\,\mathrm{m})$ can be performed with respect to a sufficiently resolved terrain structure.

In previous studies, ASAM was at first used to demonstrate the volume-of-fluid (VOF) method for non-dissipative cloud transport (Hinneburg and Knoth, 2005). In that work, it was shown that the numerical diffusion of clouds can be totally suppressed by the VOF method. ASAM also took part at an intercomparison study of mesoscale, two-dimensional mountain-wave simulations for idealized and real terrain profiles, where altogether 11 different nonhydrostatic numerical models were compared with each other (Doyle et al., 2011). New numerical methods like an explicit two-step peer method and a partially implicit peer method were presented in Jebens et al. (2009, 2011), respectively. In the latter case, it could be shown that the used method is very suitable to overcome the small cell problem around orography when using cut cells. König (2013) used the model in an LES setup for the first time. He studied dynamic flow structures in a turbulent urban environment with a building-resolving resolution. There, the implementation of a dynamic Smagorinsky SGS model is tested for a dry convective atmospheric boundary layer was presented. Furthermore, a synthetic inflow generation approach that produces a turbulent flow field was developed for this particular study.

An offshoot of ASAM that was separately developed and designed to run on Graphics Processing Units (GPUs) is called ASAMgpu (Horn, 2012). In that model, the basic numerical features of ASAM were transferred to ASAMgpu. These features are the usage of the fully-compressible Euler equations with a 3rd-order advection scheme and an explicit three-step Runge Kutta scheme with a time-splitting algorithm. ASAMgpu is focused on scales between LES and cloud-resolving models (CRMs), whereat for LES the turbulent diffusion is treated implicitly, i.e., no subgrid scale models are used (Hickel, 2008). A detailed technical description together with a series of test cases and simulations of marine boundary layers can be found in Horn (2015). Observational studies of heat island effects and vertical mixing of aerosols at the Cape Verde islands were compared with ASAMgpu LES results in Engelmann et al. (2011).

Going back to the original ASAM, there were some key features missing to perform the large eddy simulations for Barbados at the time when this PhD work started:

- Only the conversion of water vapor to cloud water was available. Therefore, a sophisticated two-moment cloud microphysics scheme had to be implemented, tested and verified. This scheme has to include a new class 'rain water' and new classes for number concentrations of CCN, cloud droplets and rain drops.
- Real orographical data has to be used and pre-processed for the computational grid. A smoothing algorithm has to be implemented to compensate sharp gradients without compromising the accuracy.
- Appropriate open boundary conditions with minimal wave reflections have to be selected and tested for the island simulations.
- The interaction of all these components has to be assured.

In the following sections, a complete model description is presented showing all required aspects for performing LES studies. It should provide insights into similarities and differences to other existing LES models like UCLALES (University of California, Los Angeles Large-Eddy Simulation Code, used by MPI-M, Hamburg, Germany) (Stevens et al., 1999, 2005; Stevens and Seifert, 2008; Heus and Seifert, 2013), PALM (PArallelized Large-Eddy Simulation Model) (Raasch and Schröter, 2001; Maronga et al., 2015), DALES (Dutch Atmospheric Large-Eddy Simulation) (Heus et al., 2010) or the WRF (Weather Research and Forecasting) model that can also be used in LES mode (Moeng et al., 2007). This chapter is based on the model description that was already published in Jähn et al. (2015a).

2.2 Governing equations

The flux-form compressible Euler equations for the atmosphere are

$$\frac{\partial \rho}{\partial t} + \nabla \cdot (\rho \vec{v}) = 0 \tag{2.1}$$

$$\frac{\partial (\rho \vec{v})}{\partial t} + \nabla \cdot (\rho \vec{v} \vec{v}) = -\nabla \cdot \vec{\tau} - \nabla p - \rho \vec{g} - 2\vec{\Omega} \times (\rho \vec{v}) \tag{2.2}$$

$$\frac{\partial (\rho \phi)}{\partial t} + \nabla \cdot (\rho \vec{v} \phi) = -\nabla \cdot \vec{q}_\phi + S_\phi \tag{2.3}$$

where ρ is the total air density, $\vec{v} = (u, v, w)^\mathrm{T}$ the three-dimensional velocity vector, p the air pressure, $\vec{g}$ the gravitational acceleration, $\vec{\Omega}$ the angular velocity vector of the earth, ϕ a scalar quantity and S_ϕ the sum of its corresponding source terms. The subgrid scale terms are $\vec{\tau}$ for momentum and $\vec{q}_\phi$ for a given scalar.

The energy equation in the form of Eq. (2.3) is represented by the (dry) potential temperature θ. In the presence of water vapor and cloud water, this quantity is replaced by the density potential temperature θ_ρ (Emanuel, 1994; Bryan and Fritsch, 2002) as a more generalized form of the virtual potential temperature θ_v:

$$\theta_\rho = \theta \left(1 + q_\mathrm{v} \left[\frac{R_\mathrm{v}}{R_\mathrm{d}} - 1\right] - q_\mathrm{l}\right) \tag{2.4}$$

where the equation of state can be expressed as follows:

$$p = \rho R_\mathrm{d} \theta_\rho \left(\frac{p}{p_0}\right)^{\kappa_\mathrm{m}} \tag{2.5}$$

In the above two equations $\theta = T(p_0/p)^{\kappa_\mathrm{m}}$ is the potential temperature, $q_\mathrm{v} = \rho_\mathrm{v}/\rho$ is the mass ratio of water vapor in the air (specific humidity), $q_\mathrm{l} = \rho_\mathrm{l}/\rho$ is the mass ratio of liquid water in the air, p_0 a reference pressure and $\kappa_\mathrm{m} = (q_\mathrm{d} R_\mathrm{d} + q_\mathrm{v} R_\mathrm{v})/(q_\mathrm{d} c_\mathrm{pd} + q_\mathrm{v} c_\mathrm{pv} + q_\mathrm{l} c_\mathrm{pl})$ the Poisson constant for the air mixture (dry air, water vapor, cloud water) with $q_\mathrm{d} = \rho_\mathrm{d}/\rho$. R_d and R_v are the gas constants for dry air and water vapor, respectively. When deriving the prognostic equations for θ_ρ in the formulation of (2.4), additional terms involving the spatial derivatives of q_v and q_l have to be considered. A thorough derivation of the density potential temperature tendency equation is presented in Appendix A. The resulting equation includes source terms for water vapor, phase changes and precipitation.

The number of additional equations like Eq. (2.3) depends on the complexity of the used microphysical scheme. Furthermore, tracer variables can also be included. The values of all relevant physical constants are listed in Table 2.1.

Table 2.1: Physical constants.

Symbol	Quantity	Value
p_0	Reference pressure	10^5 Pa
R_d	Gas constant for dry air	$287\,\mathrm{J\,kg^{-1}\,K^{-1}}$
R_v	Gas constant for water vapor	$461\,\mathrm{J\,kg^{-1}\,K^{-1}}$
c_pd	Specific heat capacity at constant pressure for dry air	$1004\,\mathrm{J\,kg^{-1}\,K^{-1}}$
c_pv	Specific heat capacity at constant pressure for water vapor	$1885\,\mathrm{J\,kg^{-1}\,K^{-1}}$
c_pl	Specific heat capacity at constant pressure for liquid water	$4186\,\mathrm{J\,kg^{-1}\,K^{-1}}$
c_vd	Specific heat capacity at constant volume for dry air	$717\,\mathrm{J\,kg^{-1}\,K^{-1}}$
c_vv	Specific heat capacity at constant volume for water vapor	$1424\,\mathrm{J\,kg^{-1}\,K^{-1}}$
L_{00}	Latent heat at 0 K	$3.148 \times 10^6\,\mathrm{J\,kg^{-1}}$
g	Gravitational acceleration	$9.81\,\mathrm{m\,s^{-2}}$

2.3 Cut cells and spatial discretization

2.3.1 Advantages of a cut cell formulation and state of the art

For simulating the flow around obstacles, buildings or orography, the cut cell approach is used in ASAM. With this attempt one remains within the Cartesian grid and the numerical pressure derivative in the vicinity a structure is zero if the cut cell geometry is not taken into account. This is not the case in terrain-following coordinate systems due to the slope of the lowest cells (Lock et al., 2012). Since this skewness is also reproduced in upper levels, a cut cell model produces reduced or greatly reduced errors in comparison models with terrain-following coordinates (Good et al., 2014). Several techniques have been developed to overcome these non-physical errors associated with terrain-following grids, especially when spatial scales of three-dimensional models become finer (which leads to a steepening of the model orography). Tripoli and Smith (2014a) introduced a Variable-Step Topography (VST) surface coordinate system within a nonhydrostatic host model. Unlike the traditional discrete-step approach, the depth of a grid box intersecting with a topographical structure is adjusted to its height, which leads to straight cut cells. Numerical tests show that this technique produces better results than conventional approaches for different topography (severe and smooth) types (Tripoli and Smith, 2014b). In their cases, also the computational costs with the VST approach are reduced because there is no need of extra functional transform calculations due to metric terms. Steppeler et al. (2002) derived approximations for z-coordinate nonhydrostatic atmospheric models by using the shaved-element finite-volume method. There, the dynamics are computed in the cut cell system, whereas the physics computation remains in the terrain-following system. Using a z-coordinate system can also improve the prediction of meteorological parameters like clouds and rainfall due to a better representation of the atmospheric flow near mountains in a numerical weather prediction (NWP) model (Steppeler et al., 2006; Steppeler et al., 2013). The cut cell method is also used in the Ocean–Land–Atmosphere Model (OLAM) (Walko, 2008a), which extends the Regional Atmospheric Modeling System (RAMS) to a global model domain. In OLAM, the shaved-cell method is applied to an icosahedral mesh (Walko, 2008b). Yamazaki and Satomura (2008) simulated a two-dimensional flow over different mountain slopes and compared the results of their cut cell model with a model using terrain-following coordinates. Especially for steep slopes, significant errors were reported in the terrain-following model. A drawback is the generation of low-volume cells when a cut cell method is used. To avoid instability problems around these small cells, the time integration scheme has to be adapted. This can be achieved by using semi-implicit or semi-Langrangian methods, for example. In ASAM, a linear-implicit Rosenbrock time integration scheme is used (Hairer and Wanner, 2010). Another option to handle the small cells problem is to merge small cut cells with neighboring cells in either horizontal or vertical direction (Yamazaki and Satomura, 2010). However, this approach becomes more complicated when applying it to three spatial dimensions, since a lot of special cases have to be considered. To achieve reasonable vertical solutions near the ground, the usage of local mesh refinement techniques becomes interesting for large scale models (Yamazaki and Satomura, 2012).

2.3.2 Definition of cut cells

The spatial discretization is done on a Cartesian grid with grid intervals of lengths $\Delta x_i, \Delta y_j, \Delta z_k$ and can easily be extended to any orthogonal, logically rectangular

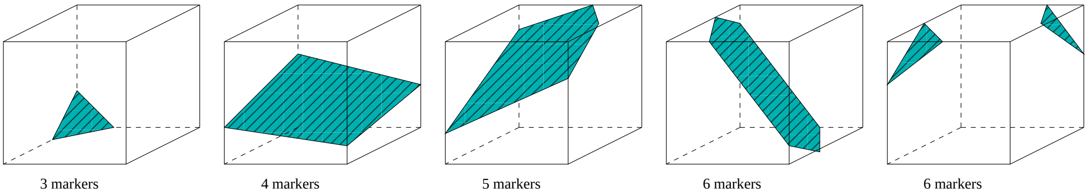
3 markers 4 markers 5 markers 6 markers 6 markers

Figure 2.1: Possible configurations for cut cell intersection (cases 1–3) for different numbers of face intersection points (markers). The last two cases are excluded.

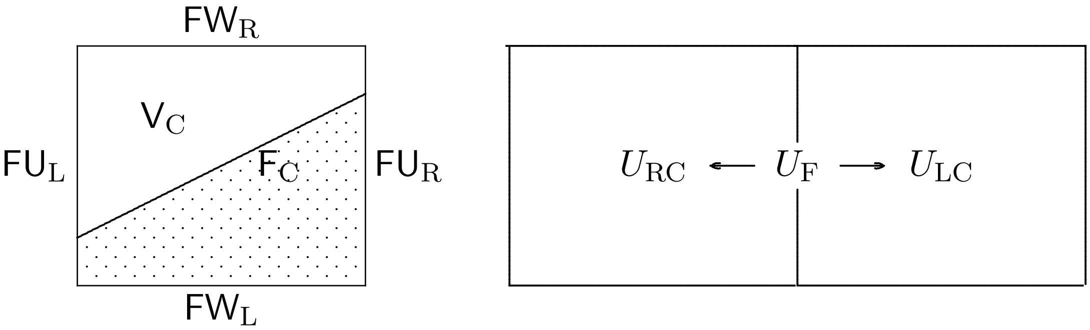

Figure 2.2: Cut cell with face and volume area information (left) and arrangement of face and cell centered momentum (right).

structured grid (i.e., it has the same logical structure as a regular Cartesian grid) like spherical or cylindrical coordinates. First, it is described for the Cartesian case and generalizations are discussed afterwards. Orography and other obstacles like buildings are presented by cut cells, which are the result of the intersection of the obstacle with the underlying Cartesian grid. In Fig. 2.1 different possible and excluded configurations are shown for the three-dimensional case. For the spatial discretization only the six partial face areas and the partial cell volume and the grid sizes of the underlying Cartesian mesh are used. For a proper representation the orography is smoothed in such a way that the intersection of a grid cell and the orography can be described by a single possible non-planar polygon. Or in other words, a Cartesian cell is divided in at most two parts, a free part and a solid part. For each Cartesian cell, the free face area of the six faces and the free volume area of the cell are stored, which is the part outside of the obstacle. These values are denoted for the grid cell i, j, k by $\mathrm{FU}_{i-1/2,j,k}$, $\mathrm{FU}_{i+1/2,j,k}$, $\mathrm{FV}_{i,j-1/2,k}$, $\mathrm{FV}_{i,j+1/2,k}$, $\mathrm{FW}_{i,j,k-1/2}$, $\mathrm{FW}_{i,j,k+1/2}$ and $\mathrm{V}_{\ i,j,k}$, respectively. In the following, the relative notations $\mathrm{FU_L}$ and $\mathrm{FU_R}$ (L: left, R: right) are used, e.g., as shown in Fig. 2.2.

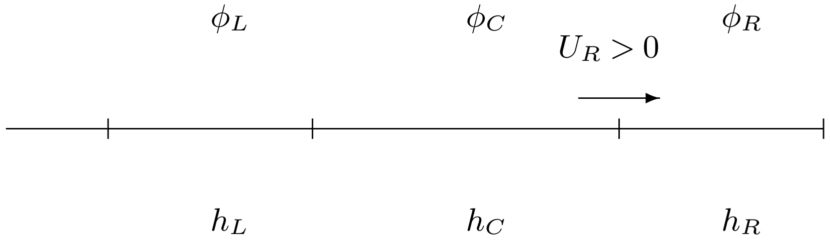

Figure 2.3: Stencil for third-order approximation.

2.3.3 Spatial discretization

The spatial discretization is formulated in terms of the grid interval length and the face and volume areas. The variables are arranged on a staggered grid with momentum $\mathbf{V} = (U, V, W) = (\rho u, \rho v, \rho w)$ at the cell faces and all other variables at the cell center (Arakawa C-grid). The discretization is a mixture of finite volumes and finite differences. In the finite volume context the main task is the reconstruction of values and gradients at cell faces from cell centered values. The discretization of the advection operator is performed for a generic cell centered scalar variable ϕ. In the context of a finite volume discretization point values of the scalar value ϕ are needed at the faces of this grid cell. Knowing these face values, the advection operator in x-direction is discretized by $(\mathrm{FU_R} U_{\mathrm{FR}} \phi_{\mathrm{R}} - \mathrm{FU_L} U_{\mathrm{FL}} \phi_{\mathrm{L}})/\mathrm{V_C}$ where U_{F} is the discretized momentum at the corresponding faces. To approximate these values at the faces, a biased upwind third-order procedure with additional limiting is used (Van Leer, 1994).

Assuming a positive flow in the x-direction, the third order approximation at $x_{i+1/2}$ is obtained by quadratic interpolation from the three values as shown in Fig. 2.3. The interpolation condition is that the three cell-averaged values are fitted:

$$\begin{aligned}\phi_{\mathrm{FR}} &= \phi_{\mathrm{C}} + \frac{h_{\mathrm{C}}(h_{\mathrm{L}} + h_{\mathrm{C}})}{(h_{\mathrm{C}} + h_{\mathrm{R}})(h_{\mathrm{L}} + h_{\mathrm{C}} + h_{\mathrm{R}})}(\phi_{\mathrm{R}} - \phi_{\mathrm{C}}) \\ &\quad + \frac{h_{\mathrm{C}} h_{\mathrm{R}}}{(h_{\mathrm{L}} + h_{\mathrm{C}})(h_{\mathrm{L}} + h_{\mathrm{C}} + h_{\mathrm{R}})}(\phi_{\mathrm{C}} - \phi_{\mathrm{L}}) \\ &= \phi_{\mathrm{C}} + \alpha_1(\phi_{\mathrm{R}} - \phi_{\mathrm{C}}) + \alpha_2(\phi_{\mathrm{C}} - \phi_{\mathrm{L}}). \end{aligned} \tag{2.6}$$

To achieve positivity in Eq. (2.6), state limiting is applied. For this task, Eq. (2.6) is rewritten in slope-ratio formulation

$$\phi_{\mathrm{FR}} = \phi_{\mathrm{C}} + K(\phi_{\mathrm{C}} - \phi_{\mathrm{L}}), \tag{2.7}$$

where

$$K = \alpha_1 \frac{\phi_\mathrm{R} - \phi_\mathrm{C}}{\phi_\mathrm{C} - \phi_\mathrm{L}} + \alpha_2. \tag{2.8}$$

Then K is replaced by limiter function Ψ and (2.7) is rewritten as

$$\phi_\mathrm{FR} = \phi_\mathrm{C} + \Psi \left(\frac{\phi_\mathrm{R} - \phi_\mathrm{C}}{\phi_\mathrm{C} - \phi_\mathrm{L}} \right) (\phi_\mathrm{C} - \phi_\mathrm{L}) \tag{2.9}$$

$$\Psi(r) = \max\left(0, \min\left[r, \min(\delta, \alpha_1 r + \alpha_2)\right]\right), \quad \delta = 2 \tag{2.10}$$

as proposed by Sweby (1984). This limiter has the property that the unlimited higher order scheme (Eq. 2.6) is used as much as possible and it is utilized only then when it is needed. In the case of $\Psi = 0$, the scheme degenerates to the simple first-order upwind scheme. The coefficients α_1 and α_2 can be computed in advance to minimize the overhead for a non-uniform grid. In the case of a uniform grid the coefficients are constant, i.e., they are equal to $\alpha_1 = 1/3$ and $\alpha_2 = 1/6$. For a detailed discussion of the benefits of this approach and numerical experiments cf. Hundsdorfer et al. (1995). This procedure is applied in all three grid directions, where the virtual grid sizes h are defined by

$$h_\mathrm{L} = \mathrm{V_L}/\mathrm{F_L} \tag{2.11}$$

$$h_\mathrm{C} = 0.5\mathrm{V_C}/(\mathrm{F_L} + \mathrm{F_R}) \tag{2.12}$$

$$h_\mathrm{R} = \mathrm{V_R}/\mathrm{F_R} \tag{2.13}$$

2.3.4 Momentum

To solve the momentum equation, the non-linear advection term is needed on the cell face. This is achieved by a shifting technique introduced by Hicken et al. (2005) for the incompressible Navier–Stokes-Equation. For each cell two cell-centered values of each of the three components of the Cartesian velocity vector are computed and transported with the presented advection scheme for a cell-centered scalar value. The obtained tendencies are then interpolated back to the faces. This approach avoids separate advection routines for the momentum components. For a normal cell the shifted values are obtained from the six momentum face values, whereas for a cut cell the shift operation takes the weights of the faces of the two opposite sides into account (cf. Fig. 2.2 for the used notation).

$$U_\mathrm{LC} = \begin{cases} U_\mathrm{FL} & \text{if } \mathrm{FU_L} \geq \mathrm{FU_R} \\ \left(U_\mathrm{FL}\mathrm{FU_L} + U_\mathrm{FR}\left[\mathrm{FU_R} - \mathrm{FU_L}\right]\right)/\mathrm{FU_R} & \text{else.} \end{cases} \tag{2.14}$$

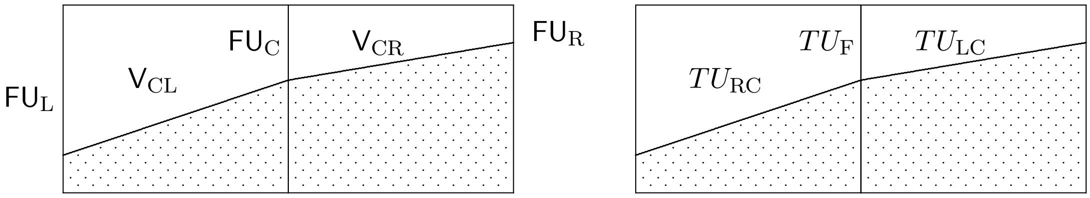

Figure 2.4: Two neighbored cut cells with face and volume area information (left) and arrangement of face and cell centered tendency of momentum (right).

The interpolation of the cell tendencies TU_{LC}, TU_{RC} back to a face tendency TU_{F} is obtained by the arithmetic mean of the two tendencies of the two shifted cell components originated from the same face. For a cut face the interpolation takes the form (see Fig. 2.4):

$$TU_{\mathrm{F}} = \left(\frac{TU_{\mathrm{RC}} \mathrm{V}_{\mathrm{L}}}{\mathrm{FU}_{\mathrm{L}} + \mathrm{FU}_{\mathrm{C}}} + \frac{TU_{\mathrm{LC}} \mathrm{V}_{\mathrm{R}}}{\mathrm{FU}_{\mathrm{R}} + \mathrm{FU}_{\mathrm{C}}} \right) \cdot \left(\frac{\mathrm{V}_{\mathrm{L}}}{\mathrm{FU}_{\mathrm{L}} + \mathrm{FU}_{\mathrm{C}}} + \frac{\mathrm{V}_{\mathrm{R}}}{\mathrm{FU}_{\mathrm{R}} + \mathrm{FU}_{\mathrm{C}}} \right)^{-1}, \tag{2.15}$$

The pressure gradient and the Buoyancy term are computed for all faces with standard difference and interpolation formulas with the grid sizes taken from the underlying Cartesian grid. To approximate the pressure gradient at the interface of two grid cells with only the pressure values of the two grid cells there is some freedom in choosing the grid size. Whereas in Adcroft et al. (1997) the grid size is chosen to preserve energy in their model, the approach of Ng et al. (2009) is used where the cut cell structure is not taken into account. Both versions are implemented in the ASAM code and it became apparent that the second one is more suitable to simulate flows in hydrostatic balance.

2.3.5 Boundary flux distribution near cut cells

Due to small cell volumes around cut cells, boundary fluxes such as sensible and latent surface heat fluxes have to be distributed to the surrounding cells to avoid instability problems because of sharp gradients in the respective scalar fields. For simplicity a two-dimensional case in x- and z-direction is considered. An example configuration is displayed in Fig. 2.5.

The common partial face area of two neighboring cells is greater than the opposite face (i.e., left vs. right in x- and y-direction, bottom vs. top in z-direction),

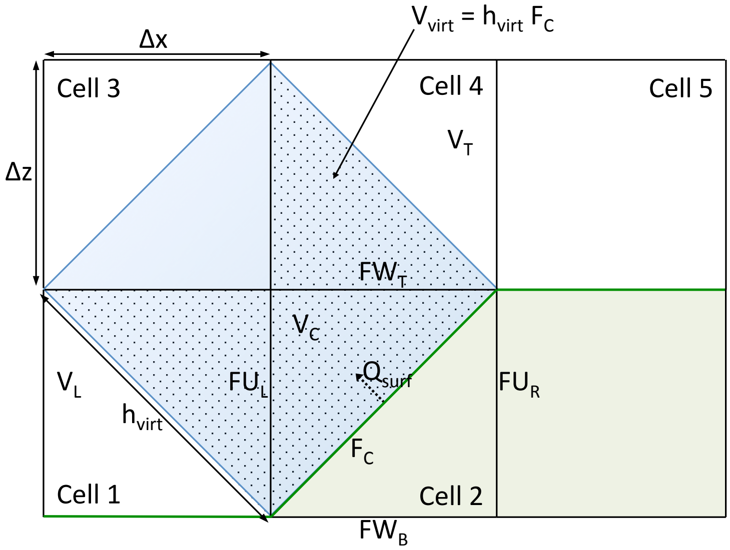

Figure 2.5: Example configuration for surface flux distribution around a cut cell. Green shading represents the solid part of the cells, whereas blue shading is the "virtual volume" normal to the cut cell face. The total surface flux Q_{surf} is distributed within the dotted area.

e.g., in our case $\text{FU}_\text{L} > \text{FU}_\text{R}$ and $\text{FW}_\text{T} > \text{FW}_\text{B}$. For the flux distribution a virtual volume over the cut cell face F_C is defined through

$$V_{\text{virt}} = \text{F}_\text{C} h_{virt} \,, \tag{2.16}$$

where

$$h_{\text{virt}} = \Delta x |n_x| + \Delta z |n_z| \,. \tag{2.17}$$

Here, $(n_x, n_z)^\text{T}$ is the normal unit vector of the cut cell face F_C. Then the flux fraction with a weight of $\text{V}_\text{C}/V_{\text{virt}}$ is added to the cut cell (cell 2 in Fig. 2.5). The remaining part that has to be distributed is weighted by the face values $|\text{FU}_\text{L} - \text{FU}_\text{R}|/\text{F}_{\text{surf}} \cdot \text{V}_\text{C}/(\Delta x \Delta y \Delta z)$ to the neighbored cells in x-direction (cell 1 in the example) and $|\text{FW}_\text{B} - \text{FW}_\text{T}|/\text{F}_{\text{surf}} \cdot \text{V}_\text{C}/(\Delta x \Delta y \Delta z)$ in z-direction (cell 4 in the example), where $\text{F}_{\text{surf}} = |\text{FU}_\text{L} - \text{FU}_\text{R}| + |\text{FW}_\text{B} - \text{FW}_\text{T}|$. With this approach, only the available information of the considered cut cell (volume and common face areas with neighboring cells) and not of its surrounding cells is needed. The extension of this method to the third spatial dimension is done analogously.

2.4 Time integration

After spatial discretization an ordinary differential equation

$$y'(t) = F(y(t)) \tag{2.18}$$

is obtained that has to be integrated in time (method of lines). To tackle the small time step problem connected with tiny cut cells, linear implicit Rosenbrock-W-methods are used (Knoth, 2006; Jebens et al., 2011; John and Rang, 2010).

A Rosenbrock method has the form

$$\begin{aligned} (\mathbf{I} - \tau\gamma\mathbf{J})\, k_i &= \tau F(y_n + \sum_{j=1}^{i-1} \alpha_{ij} u_j) + \sum_{j=1}^{i-1} \gamma_{ij} k_j, \quad i = 1, \dots, s \\ y_{n+1} &= y_n + \sum_{j=1}^{s} \alpha_{s+1j} k_j, \end{aligned} \tag{2.19}$$

where y_n is a given approximation at $y(t)$ at time t_n and subsequently y_{n+1} at time $t_{n+1} = t_n + \tau$. In addition, $\mathbf{J}$ is an approximation to the Jacobian matrix $\partial F/\partial y$. A Rosenbrock method is therefore fully described by the two matrices $\mathcal{A} = (\alpha_{ij})$, $\Gamma = (\gamma_{ij})$ and the parameter γ.

Among the available methods are a second order two stage method after Lanser et al. (2001).

$$\mathbf{S}k_1 = \tau F(y_n)\,, \tag{2.20}$$

$$\mathbf{S}k_2 = \tau F\left(y_n + \frac{2}{3}k_1\right) - \frac{4}{3}k_1\,, \tag{2.21}$$

$$y_{n+1} = y_n + \frac{5}{4}k_1 + \frac{3}{4}k_2\,, \tag{2.22}$$

$$\mathbf{S} = \mathbf{I} - \gamma\tau\mathbf{J}, \quad \mathbf{J} \approx F'(y_n)\,. \tag{2.23}$$

with $\gamma = \frac{1}{2} + \frac{1}{6}\sqrt{3}$ or in matrix form in Table 2.2.

Moreover, a new Rosenbrock method was constructed from a low storage three stage second-order Runge–Kutta method, which is used in split-explicit time integration methods in the Weather Research and Forecasting (WRF) Model (Skamarock et al., 2008) or in the Consortium for Small-scale Modeling (COSMO) model (Doms et al., 2011). Its coeffcients are given in Table 2.3.

Table 2.2: Coefficient table for the ROS2 scheme.

0			
2/3			
−5/4	3/4	−4/3	$\frac{1}{2}+\frac{1}{6}\sqrt{3}$
$\mathcal{A}$-Matrix		Γ-Matrix	γ

Table 2.3: Coefficient table for the ROSRK3 scheme.

0			0		
1/3			−11/27		1
11/54	1/2		17/27	−11/4	
−17/27	11/4	1			
$\mathcal{A}$-Matrix			Γ-Matrix		γ

The above described Rosenbrock-W-methods allow a simplified solution of the linear systems without losing the order. When $\mathbf{J} = \mathbf{J}_\mathrm{A} + \mathbf{J}_\mathrm{B}$ the matrix $\mathbf{S}$ can be replaced by $\mathbf{S} = (\mathbf{I} - \gamma\tau\mathbf{J}_\mathrm{A})(\mathbf{I} - \gamma\tau\mathbf{J}_\mathrm{B})$. Further simplification can be reached by omitting some parts of the Jacobian or by replacing of the derivatives by the same derivatives of a simplified operator $\tilde{F}(w^n)$. For instance higher-order interpolation formula are replaced by the first-order upwind method. The structure of the Jacobian is

$$\mathbf{J} = \begin{pmatrix} \frac{\partial F_\rho}{\partial \rho} & \frac{\partial F_\rho}{\partial \vec{V}} & 0 \\ \frac{\partial F_{\vec{V}}}{\partial \rho} & \frac{\partial F_{\vec{V}}}{\partial \vec{V}} & \frac{\partial F_{\vec{V}}}{\partial \Theta} \\ 0 & \frac{\partial F_\Theta}{\partial \vec{V}} & \frac{\partial F_\Theta}{\partial \Theta} \end{pmatrix}. \tag{2.24}$$

A zero block 0 indicates that this block is not included in the Jacobian or is absent. The derivative with respect to ρ is only taken for the buoyancy term in the vertical momentum equation. Note that this type of approximation is the standard approach in the derivation of the Boussinesq approximation starting from the compressible Euler equations. The matrix $\mathbf{J}$ can be decomposed as

$$\mathbf{J} = \mathbf{J}_\mathrm{T} + \mathbf{J}_\mathrm{P} = \begin{pmatrix} \frac{\partial F_\rho}{\partial \rho} & 0 & 0 \\ \frac{\partial F_{\vec{V}}}{\partial \rho} & \frac{\partial F_{\vec{V}}}{\partial \vec{V}} & 0 \\ 0 & 0 & \frac{\partial F_\Theta}{\partial \Theta} \end{pmatrix} + \begin{pmatrix} 0 & \frac{\partial F_\rho}{\partial \vec{V}} & 0 \\ 0 & 0 & \frac{\partial F_{\vec{V}}}{\partial \Theta} \\ 0 & \frac{\partial F_\Theta}{\partial \vec{V}} & 0 \end{pmatrix} \tag{2.25}$$

or

$$\mathbf{J} = \mathbf{J}_{\mathrm{T}} + \mathbf{J}_{\mathrm{P}} = \begin{pmatrix} \frac{\partial F_\rho}{\partial \rho} & 0 & 0 \\ 0 & \frac{\partial F_{\vec{V}}}{\partial \vec{V}} & 0 \\ 0 & 0 & \frac{\partial F_\Theta}{\partial \Theta} \end{pmatrix} + \begin{pmatrix} 0 & \frac{\partial F_\rho}{\partial \vec{V}} & 0 \\ \frac{\partial F_{\vec{V}}}{\partial \rho} & 0 & \frac{\partial F_{\vec{V}}}{\partial \Theta} \\ 0 & \frac{\partial F_\Theta}{\partial \vec{V}} & 0 \end{pmatrix}. \tag{2.26}$$

The first part of the splitting $\mathbf{J}_{\mathrm{T}}$ is called the transport or source part and contains the advection, diffusion and source terms like Coriolis, curvature, buoyancy, latent heat release and so on. The second matrix $\mathbf{J}_{\mathrm{P}}$ is called the pressure part and involves the derivatives of the pressure gradient with respect to the density weighted potential temperature and of the divergence with respect to momentum of the density and potential temperature equation. The difference between the two splitting approaches is the insertion of the derivative of the gravity term in the transport or pressure matrix. The first splitting (Eq. 2.25) damps sound waves. For this splitting the second linear system with the pressure part of the Jacobian can be reduced to a Poisson-like equation. The second splitting (Eq. 2.26) damps sound and gravity waves but the dimension of the pressure system is doubled. Both systems are solved by preconditioned conjugate gradient (CG)-like methods (Dongarra et al., 1998).

For the transport/source system the Jacobian can be further split into

$$\mathbf{J}_{\mathrm{T}} = \mathbf{J}_{\mathrm{AD}} + \mathbf{J}_{\mathrm{S}} \tag{2.27}$$

where the matrix $\mathbf{J}_{\mathrm{AD}}$ is the derivative of the advection and diffusion operator where the unknowns are coupled between grid cells. The matrix $\mathbf{J}_{\mathrm{S}}$ assembles the source terms. Here, the coupling is between the unknowns of different components in each grid cell. With this additional splitting the linear equation

$$(\mathbf{I} - \gamma\tau\mathbf{J}_{\mathrm{AD}} - \gamma\tau\mathbf{J}_{\mathrm{S}})\Delta w = R \tag{2.28}$$

is preconditioned from the right with the matrix

$$\mathbf{P}_{\mathrm{r}} = (\mathbf{I} - \gamma\tau\mathbf{J}_{\mathrm{AD}})^{-1} \tag{2.29}$$

and from the left with the matrix

$$\mathbf{P}_{\mathrm{l}} = (\mathbf{I} - \gamma\tau\mathbf{J}_{\mathrm{S}})^{-1}. \tag{2.30}$$

The matrix

$$\mathbf{P}_{\mathrm{l}}(\mathbf{I} - \gamma\tau\mathbf{J}_{\mathrm{AD}} - \gamma\tau\mathbf{J}_{\mathrm{S}})\mathbf{P}_{\mathrm{r}} \tag{2.31}$$

can be written in the following form by using the Eisenstat trick (Eisenstat, 1981):

$$(\mathbf{I} - \gamma\tau \mathbf{P}_\mathrm{l} \mathbf{J}_\mathrm{AD})\mathbf{P}_\mathrm{r} = (\mathbf{I} + \mathbf{P}_\mathrm{l}((\mathbf{I} - \gamma\tau \mathbf{J}_\mathrm{AD}) + \mathbf{I}))\mathbf{P}_\mathrm{r}. \tag{2.32}$$

Therefore only the LU-decomposition of the matrix $(\mathbf{I} - \gamma\tau\mathbf{J}_\mathrm{S})$ has to be stored. The matrix $(\mathbf{I} - \gamma\tau\mathbf{J}_\mathrm{AD})$ is inverted by a fixed number of Gauss–Seidel iterations.

The second matrix of the splitting approach writes in case of the first splitting (Eq. 2.25) as follows:

$$(\mathbf{I} - \gamma\tau\mathbf{J}_\mathrm{P}) = \begin{pmatrix} \mathbf{I} & \gamma\tau \mathrm{GRAD}\,\mathbf{D}_\Theta \\ \gamma\tau \mathrm{DIV}\,\mathbf{D}_{\vec{V}} & \mathbf{I} \end{pmatrix}, \tag{2.33}$$

where $\mathbf{D}_{\vec{V}}$ and $\mathbf{D}_\Theta$ are diagonal matrices. GRAD and DIV are matrix representations of the discrete gradient respectively divergence operator. The entries of the matrix $\mathbf{D}_{\vec{V}}$ are the potential temperature at cell faces and the entries of the matrix $\mathbf{D}_\Theta$ are the derivative of the pressure in the cell center with respect to the density weighted potential temperature. Elimination of the momentum part gives a Helmholtz equation for the increment of the potential temperature. This equation is solved by a CG-method with a multigrid as a preconditioner. For the second splitting (Eq. 2.26) the resulting matrix is twice in dimension and not symmetric anymore.

As basic iterative solvers BiCGStab is applied for the transport/source system and GMRES for the pressure part (Dongarra et al., 1998). The number of iterations for the two iterative methods are problem dependent. They increase with increasing time step and are usually in the range of 2 to 5 iterations.

Furthermore, different types of split-explicit time integration methods are available, which are especially suitable for simulations over flat surfaces (Wensch et al., 2009; Knoth and Wensch, 2014).

2.5 Extension to other grids

The presented discretization is also valid for grids described by cylindrical and spherical coordinates with a suitable choice for the computation of the face and volume area. For a lat-lon grid on the sphere the weights have to be computed through

$$\mathrm{F_W} = r_C \Delta\varphi \Delta z\,, \tag{2.34a}$$

$$\mathrm{F_E} = r_C \Delta\varphi \Delta z\,, \tag{2.34b}$$

$$\mathrm{F_S} = r_C \Delta\lambda \cos\varphi_S \Delta z\,, \tag{2.34c}$$

$$\mathrm{F_N} = r_C \Delta\lambda \cos\varphi_N \Delta z\,, \tag{2.34d}$$

$$\mathrm{F_B} = r_B^2 \Delta\lambda \Delta\varphi \cos\varphi_C\,, \tag{2.34e}$$

$$\mathrm{F_T} = r_T^2 \Delta\lambda \Delta\varphi \cos\varphi_C\,, \tag{2.34f}$$

$$\mathrm{V_C} = r_C^2 \Delta\lambda \Delta\varphi \cos\varphi_C \Delta z\,. \tag{2.34g}$$

In the formulas above $\Delta\varphi$, $\Delta\lambda$, and Δz are the grid increments in meridional, zonal and vertical direction, respectively. The terms r_B, r_C, and r_T are the radii of the bottom, central and top layer of a grid cell, respectively. The same applies for the latitudes φ_S, φ_C and φ_N, where the subscript S denotes South, C stands for center and N refers to North. Besides the addition of a curvature term, which has to be discretized for the momentum components, no further changes are necessary in the algorithm. The stability problems near the poles are again circumvented through the implicit time integration.

2.6 Parallelization

Parallelization is realized by using the Message Passing Interface (MPI) and the domain decomposition method. There, the computational domain is horizontally divided (i.e., in x- and y-direction) into subdomains of the same size, at which each processor element saves the data of the subdomain and solves the model equations at its grid points. The number of grid points per processor element should be of about $\mathcal{O}(10^5)$, e.g., $32 \times 32 \times 100$ grid points. This enables a good utilization rate regarding computation and exchange of data, the latter being necessary since values of neighbored processor elements have to be stored in ghost cells to solve the model equations.

The ASAM code is portable between different platforms like Linux, IBM, Mac OS and high-performance computing (HPC) clusters. The computational expensive large eddy simulations performed in Chapter 5 were conducted at the Center for Information Services and High Performance Computing (ZIH, *Zentrum für Informationsdienste und Hochleistungsrechnen*) of TU Dresden. In particular, the simulations ran on the Bull clusters "Taurus" with a computing power of 1.02 PFlops on CPUs, 210 TFlops on GPUs and a 2.5 PByte file system.

2.7 Physical parameterizations

2.7.1 Smagorinsky subgrid-scale model

The set of coupled differential equations can be solved for a given flow problem. For simulating turbulent flows with large eddy simulations, the Euler equations mentioned at the beginning have to be modified. Within the technique of LES it is necessary to characterize the unresolved motion. By solving Eq. (2.1)–(2.3) numerically with a grid size that is above the size of the smallest turbulent scales, the equations have to be filtered. Large eddy simulation employs a spatial filter to separate the large scale motion from the small scales. Large eddies are resolved explicitly by the prognostic Euler equations down to a pre-defined filter-scale Δ, while smaller scales have to be modeled. Due to the filtering operation, additional terms that cannot be derived trivially occur in the set of the Euler equations.

Nevertheless, to solve the filtered set of equations, it is necessary to parameterize the additional subgrid-scale stress terms $\tau_{ij} = \overline{u_i u_j} - \overline{u}_i \overline{u}_j$ for momentum and $q_{ij} = \overline{u_i q_j} - \overline{u}_i \overline{q}_j$ for scalars. Note that τ_{ij} expresses the effect of subgrid-scale motion on the resolved large scales and is often represented as an additional viscosity ν_t with the following formulation:

$$\tau_{ij} = -2\nu_\mathrm{t}\overline{S}_{ij}\,, \tag{2.35}$$

where $\overline{S}_{ij} = \frac{1}{2}\left(\frac{\partial \overline{u}_i}{\partial x_j} + \frac{\partial \overline{u}_j}{\partial x_i}\right)$ is the strain rate tensor and ν_t the turbulent eddy viscosity. To determine the additional eddy viscosity, the standard Smagorinsky subgrid-scale model (Smagorinsky, 1963) is used:

$$\nu_\mathrm{t} = (C_\mathrm{s}\overline{\Delta})^2|\overline{\mathbf{S}}|\,, \tag{2.36}$$

where $\overline{\Delta}$ is a length scale, C_s the Smagorinsky coefficient, and using the Einstein summation notation for standardization $|\overline{\mathbf{S}}| = \sqrt{2\overline{S}_{ij}\overline{S}_{ij}}$. The grid spacing is used as a measure for the length scale. This standard Smagorinsky subgrid-scale model is widely used in atmospheric and engineering applications. The Smagorinsky coefficient C_s has a theoretical value of about 0.2, as estimated by Lilly (1967).

Applying this value to a turbulence-driven flow with thermal convection fields results in a good agreement with observations as shown by Deardorff (1972).

To take stratification effects into account, Lilly (1962) modified the standard Smagorinsky formulation by changing the eddy viscosity to

$$\nu_{\mathrm{t}} = (C_{\mathrm{s}}\overline{\Delta})^2 \max\left[0, \left(|\overline{\mathbf{S}}|^2\left(1-\frac{Ri}{Pr}\right)\right)\right]^{1/2} \tag{2.37}$$

with

$$Ri = \frac{\frac{g}{\theta_\rho}\frac{\partial\theta_\rho}{\partial z}}{|\overline{\mathbf{S}}|^2}\,. \tag{2.38}$$

Here Ri is the Richardson number and Pr is the turbulent Prandtl number. In a stable boundary layer the vertical gradient of the potential temperature is greater than zero (positive), which leads to a positive Richardson number and, thus, the additional term Ri/Pr reduces the square of the strain rate tensor and decreases the turbulent eddy viscosity. Therefore, less turbulent vertical mixing takes place.

The implementation in the ASAM code is accomplished in the main diffusion routine of the model. It develops the whole term of $\partial/\partial x_j\,[\rho D S_{ij}]$ for every time step. The coefficient D represents D_{mom} for the momentum and D_{pot} for the potential subgrid-scale stress. Further routines describe the computation of D_{mom} and D_{pot} the following way:

$$D_{\mathrm{mom}} = (C_{\mathrm{s}}\overline{\Delta})^2|\overline{\mathbf{S}}|\,. \tag{2.39}$$

The potential subgrid-scale stress is related to the Prandtl similarity and can be developed by dividing the subgrid-scale stress tensor for momentum by the turbulent Prandtl number Pr that typically has a value of 1/3 (Deardorff, 1972). The length scale $\overline{\Delta}$ in the Standard Smagorinsky formulation is set to the value of grid spacing. However, the cut cell approach makes it difficult because of tiny and/or anisotrope cells. To overcome this deficit the value is defined after Scotti et al. (1993):

$$\overline{\Delta} = (\Delta x \Delta y \Delta z)^{1/3} f(a_1, a_2)\,. \tag{2.40}$$

Δ is the grid spacing in orthogonal directions, and a correction function f is applied as follows:

$$f(a_1, a_2) = \cosh\left[\frac{4}{27}\left(\ln^2 a_1 - \ln a_1 \ln a_2 + \ln^2 a_2\right)\right]^{1/2}$$
$$\text{with} \quad a_1 = \frac{\Delta x}{\Delta z}, \quad a_2 = \frac{\Delta y}{\Delta z}. \tag{2.41}$$

Here a_1 and a_2 are the ratios of grid spacing in different directions with the assumption that $\Delta x \leq \Delta y \leq \Delta z$. For an isotropic grid $f = 1$.

2.7.2 Two-moment warm cloud microphysics scheme

The implemented microphysics scheme is based on the work of Seifert and Beheng (2006). This scheme explicitly represents two moments (mass and number density) of the hydrometeor classes cloud droplets and rain drops. Ice phase hydrometeors are currently not implemented in the model. Altogether, seven microphysical processes are included: condensation/evaporation ("COND"), cloud condensation nuclei (CCN) activation to cloud droplets at supersaturated conditions ("ACT"), autoconversion ("AUTO"), self-collection of cloud droplets ("SCC"), self-collection of rain drops ("SCR"), accretion ("ACC") and evaporation of rain ("EVAP"):

$$\frac{\partial(\rho q_\mathrm{v})}{\partial t} + \nabla \cdot (\rho \vec{v} q_\mathrm{v}) = -S_\mathrm{COND} - S_\mathrm{ACT} + S_\mathrm{EVAP}\,, \tag{2.42}$$

$$\frac{\partial(\rho q_\mathrm{c})}{\partial t} + \nabla \cdot (\rho \vec{v} q_\mathrm{c}) = +S_\mathrm{COND} + S_\mathrm{ACT} - S_\mathrm{AUTO} - S_\mathrm{ACC}\,, \tag{2.43}$$

$$\frac{\partial(\rho q_\mathrm{r})}{\partial t} + \nabla \cdot (\rho \vec{v} q_\mathrm{r}) = +S_\mathrm{AUTO} + S_\mathrm{ACC} - S_\mathrm{EVAP}\,, \tag{2.44}$$

$$\frac{\partial N_\mathrm{CCN}}{\partial t} + \nabla \cdot (\vec{v} N_\mathrm{CCN}) = -S_{\mathrm{COND}_\mathrm{N}} - S_{\mathrm{ACT}_\mathrm{N}} + S_{\mathrm{EVAP}_\mathrm{N}}\,, \tag{2.45}$$

$$\frac{\partial N_\mathrm{c}}{\partial t} + \nabla \cdot (\vec{v} N_\mathrm{c}) = +S_{\mathrm{COND}_\mathrm{N}} + S_{\mathrm{ACT}_\mathrm{N}} - S_{\mathrm{AUTO}_\mathrm{N}} - S_{\mathrm{ACC}_\mathrm{N}} - S_\mathrm{SCC}\,, \tag{2.46}$$

$$\frac{\partial N_\mathrm{r}}{\partial t} + \nabla \cdot (\vec{v} N_\mathrm{r}) = +S_{\mathrm{AUTO}_\mathrm{N}} + S_{\mathrm{ACC}_\mathrm{N}} - S_{\mathrm{EVAP}_\mathrm{N}} - S_\mathrm{SCR}\,. \tag{2.47}$$

Details on the conversion rates can be found in Seifert and Beheng (2006). Additionally, a limiter function is used to ensure numerical stability and avoid non-physical negative values (Horn, 2012). Since there is no saturation adjustment technique in ASAM, the condensation process is taken as an example to demonstrate the physical meaning of the limiter functions. Considering the available water vapor density ρ_v and the cloud water density ρ_c, the process of condensation (or evaporation of cloud water, respectively) is forced by the water vapor density deficit and limited by the available cloud water.

$$\mathrm{FOR} = \rho_\mathrm{v} - (p_\mathrm{vs} T / R_\mathrm{v}) \tag{2.48}$$

$$\mathrm{LIM} = \rho_\mathrm{c} \tag{2.49}$$

$$S_\mathrm{COND} = \frac{\mathrm{FOR} - \mathrm{LIM} + (\mathrm{FOR}^2 + \mathrm{LIM}^2)^{1/2}}{\tau_\mathrm{COND}} \tag{2.50}$$

Here, p_{vs} is the saturation vapor pressure and the relaxation time is set to $\tau_{\mathrm{COND}} = 5\,\mathrm{s}$. The numerator term is called Fischer–Burmeister function and has originally been used in optimization of complementary problems (cf. Kong et al., 2010). A simple model after Horn (2012) is applied to determine the corresponding changes in the number concentrations and to ensure a reduction of the cloud droplet number density to zero if there is no cloud water present. This means that N_{c} reduces when droplets are getting too small

$$S_{\mathrm{COND_N}} = \min\left(0, C\left[\frac{\rho_{\mathrm{c}}}{x_{\mathrm{min}}} - N_{\mathrm{c}}\right]\right) \tag{2.51}$$

and increases when droplets are getting too large

$$S_{\mathrm{COND_N}} = \max\left(0, C\left[\frac{\rho_{\mathrm{c}}}{x_{\mathrm{max}}} - N_{\mathrm{c}}\right]\right)\ , \tag{2.52}$$

where x_{min} and x_{max} are limiting parameters for cloud water. This ensures that the cloud droplet number concentration is within a certain range defined by distribution parameters in Seifert and Beheng (2006) if condensate is present. A time scale factor of $C = 0.01\,\mathrm{s}^{-1}$ controls the speed of this correction and appears to be reasonable for this particular process.

2.7.3 Precipitation

The sedimentation velocity of raindrops is derived as in the operationally used COSMO model from the German Weather Service (Doms et al., 2011), There, the following assumptions are made. The precipitation particles are exponentially distributed with respect to their drop diameter (Marshall–Palmer distribution):

$$f_{\mathrm{r}}(D) = N_0^{\mathrm{r}} \exp -\lambda_{\mathrm{r}} D \tag{2.53}$$

Here, λ_{r} is the slope parameter of the distribution function and $N_0^{\mathrm{r}} = 8 \times 10^6\,\mathrm{m}^{-4}$ is an empirically determined distribution parameter. The terminal fall velocity of raindrops is then assumed to be uniquely related to drop size, which is expressed by the following empirical function:

$$W_{\mathrm{f}}(D) = c_{\mathrm{r}} D^{1/2} \tag{2.54}$$

with $c_{\mathrm{r}} = 130\,\mathrm{m}^{1/2}\,\mathrm{s}^{-1}$. Finally, the precipitation flux of rainwater can be calculated by

$$\mathbf{P}_{\mathrm{r}} = \rho_{\mathrm{r}} W_{\mathrm{f}}(\rho_{\mathrm{r}}) = \int_0^{\infty} m(D) W_{\mathrm{f}}(D) f_{\mathrm{r}}(D)\,\mathrm{d}D. \tag{2.55}$$

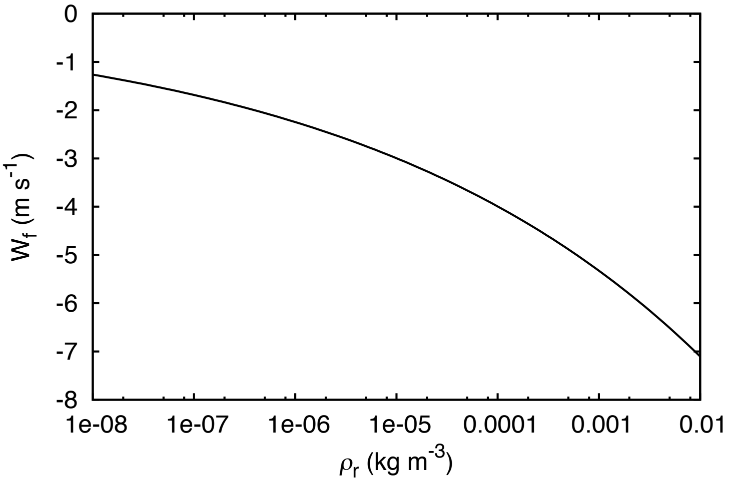

Figure 2.6: Terminal fall velocity of raindrops after Eq. (2.57).

with the raindrop mass

$$m(D) = \pi \rho_W D^3/6\,, \tag{2.56}$$

where $\rho_W = 1000\,\mathrm{kg\,m^{-3}}$ is the mass density of water. This leads to an expression for the terminal fall velocity of raindrops in dependence on their density (Fig. 2.6):

$$W_\mathrm{f}(\rho_\mathrm{r}) = -c_\mathrm{r} \frac{\Gamma(4,5)}{6} \left(\frac{\rho_\mathrm{r}}{\pi \rho_W N_{0r}} \right)^{1/8} . \tag{2.57}$$

This takes place at the tendency equation for the rain water density:

$$\frac{\partial(\rho q_\mathrm{r})}{\partial t} + \nabla_h \cdot (\rho \vec{v}_h q_\mathrm{r}) + \frac{\partial}{\partial z} (\rho q_\mathrm{r} [w + W_\mathrm{f}]) = S_{q_\mathrm{r}}\,. \tag{2.58}$$

2.7.4 Surface fluxes

A simple way to parameterize surface heat fluxes is the usage of a constant flux layer. There, the energy flux is directly given and does not depend on other variables. With the density potential temperature formulation (Eq. 2.3), the source term for this quantity has to be calculated:

$$\begin{aligned}\frac{\partial(\rho\theta_\rho)}{\partial t}+\frac{\partial}{\partial x_j}(\rho\theta_\rho u_j) &= \rho\frac{\partial\theta_\rho}{\partial t}+\theta_\rho\frac{\partial\rho}{\partial t}+\theta_\rho\frac{\partial\rho u_j}{\partial x_j}+\rho u_j\frac{\partial\theta_\rho}{\partial x_j}\\ &= \rho\left(\frac{\partial\theta_\rho}{\partial t}+u_j\frac{\partial\theta_\rho}{\partial x_j}\right)+\theta_\rho\left(\frac{\partial\rho}{\partial t}+\frac{\partial\rho u_j}{\partial x_j}\right)\\ &= \rho\frac{\mathrm{d}\theta_\rho}{\mathrm{d}t}+\theta_\rho S_\mathrm{v}\,. \end{aligned} \tag{2.59}$$

S_v is the source term of water vapor in units of [$\mathrm{kg\,m^{-3}\,s^{-1}}$]. Considering Eq. (A.34), adding the sensible heat flux and neglecting phase changes leads to

$$\frac{\partial(\rho\theta_\rho)}{\partial t}+\frac{\partial}{\partial x_j}(\rho\theta_\rho u_j)=S_{\theta_\rho} \tag{2.60}$$

with

$$S_{\theta_\rho}=\rho\theta_\rho\left(\frac{S_\mathrm{h}}{T}+\frac{S_\mathrm{v}}{\rho_\mathrm{d}}\left[\frac{R_\mathrm{v}}{R_\mathrm{m}}-\ln\pi\left(\frac{R_\mathrm{v}}{R_\mathrm{m}}-\frac{c_\mathrm{pv}}{c_\mathrm{pml}}\right)\right]\right) \tag{2.61}$$

where S_h is the heat source in units of [$\mathrm{K\,s^{-1}}$], $R_\mathrm{m}=R_\mathrm{d}+r_\mathrm{v}R_\mathrm{v}$ and $c_\mathrm{pml}=c_\mathrm{pd}+r_\mathrm{v}c_\mathrm{pv}+r_\mathrm{l}c_\mathrm{pl}$ are the gas constant and the specific heat capacity for the air mixture, respectively. The corresponding surface fluxes in [$\mathrm{W\,m^{-2}}$] are:

$$S_\mathrm{sens}=S_\mathrm{h}\frac{\rho_\mathrm{d}c_\mathrm{pml}}{\rho A}\,, \tag{2.62}$$

$$S_\mathrm{lat}=S_\mathrm{v}L_\mathrm{v}(T)\frac{V}{A}\,. \tag{2.63}$$

Here, $L_\mathrm{v}=L_{00}+(c_\mathrm{pv}-c_\mathrm{pl})T$ is the latent heat of vaporization, A is the cell surface at the bottom boundary and V the cell volume.

2.7.5 Soil model

In order to account for the interaction between land and atmosphere and the high diurnal variability of the meteorological variables in the surface layer, a soil model has been implemented into ASAM. In contrast to the constant flux layer model, the computation of the heat and moisture fluxes are now dependent on radiation, evaporation and the transpiration of vegetated area. Phase changes are not covered yet and intercepted water is only considered in liquid state.

The implemented surface flux scheme follows the description of Jiménez et al., 2012, which is the revised flux scheme used in the WRF model. The surface fluxes of momentum, heat and moisture are parameterized in the following way, respectively:

$$\tau_{zx} = \rho C_{\mathrm{m}} |\vec{v_h}| u \,, \tag{2.64a}$$

$$-\rho c_p \overline{w'\theta'} = \rho c_p C_{\mathrm{h}} |\vec{v_h}| \left(\theta - \theta(z_{0T})\right) \,, \tag{2.64b}$$

$$-\rho L \overline{w'q'} = \rho L_v C_{\mathrm{q}} |\vec{v_h}| \left(q - q(z_{0q})\right) \,. \tag{2.64c}$$

Here, C_{m}, C_{h} and C_{q} are the bulk transfer coefficients and it is considered that $C_{\mathrm{h}} = C_{\mathrm{q}}$. In Jiménez et al. (2012) the bulk transfer coefficients are defined as follows

$$C_{\mathrm{m,\,h}} = \frac{k_K^2}{\Psi_{\mathrm{M}} \Psi_{\mathrm{M,\,H}}} \tag{2.65}$$

with

$$\Psi_{\mathrm{M,H}} = \ln\left(\frac{z+z_0}{z_0}\right) - \phi_{\mathrm{m,h}}\left(\frac{z+z_0}{L}\right) + \phi_{\mathrm{m,h}}\left(\frac{z_0}{L}\right) \tag{2.66}$$

and $\phi_{\mathrm{m,\,h}}$ representing the integrated similarity functions. L stands for the Obukhov length and k_K is the von-Kármán-constant. In neutral to highly stable conditions $\phi_{\mathrm{m,h}}$ follows Cheng and Brutsaert (2005) and in unstable situations the ϕ-functions follow Fairall et al. (1996). For further details concerning limitations and restrictions see Jiménez et al. (2012).

The transport of the soil water as a result of hydraulic pressure due to diffusion and gravity within the soil layers is described by Richard's equation:

$$\frac{\partial W_{\mathrm{soil},k}}{\partial t} = \frac{\partial}{\partial z}\left(D_{\mathrm{diff}} \frac{\partial W_{\mathrm{soil},k}}{\partial z} + \kappa_{\mathrm{soil},k}\right) \tag{2.67}$$

with the diffusion coefficient

$$D_{\mathrm{diff}} = \kappa_{\mathrm{soil},k} \frac{\partial \Psi_{\mathrm{soil},k}}{\partial W_{\mathrm{soil},k}} \,. \tag{2.68}$$

$W_{\mathrm{soil},k}$ is the volumetric water content in the kth soil layer. Ψ_{soil} stands for the matric potential and κ_{soil} is the hydraulic conductivity. Ψ_{soil} and κ_{soil} are parameterized based on Van Genuchten (1980):

$$\kappa_{\mathrm{soil}} = \kappa_{\mathrm{sat}} \sqrt{W_{\mathrm{eff}}} \left(1 - \left[1 - (W_{\mathrm{eff}})^{\frac{1}{m}}\right]^m\right)^2 \tag{2.69}$$

$$\Psi_{\mathrm{soil}} = \Psi_{\mathrm{sat}} \left[(W_{\mathrm{eff}})^{-\frac{1}{m}} - 1\right]^{\frac{1}{n}} \tag{2.70}$$

W_{eff} describes the effective soil wetness, which takes a residual water content W_{res} into account, restricting the soil from complete desiccation. κ_{sat} and Ψ_{sat} are the hydraulic conductivity and the matric potential at saturated conditions, respectively. The parameters m and n describe the pore distribution (Braun, 2002) with $m = 1 - 1/n$.

Further addition/extraction of soil water is controlled by the percolation of intercepted water into the ground and the evaporation and transpiration of water from bare soil and vegetation. The mechanisms implemented are based on the Multi-Layer Soil and Vegetation Model TERRA_ML as described in Doms et al. (2011). The evaporation of bare soil is adjusted to the parameterization proposed by Noilhan and Planton (1989). The variation of the soil temperature is a result of heat conductivity depending on the soil texture and the soil water content of the respective soil layer:

$$\frac{\partial T_{\mathrm{soil}}}{\partial t} = \frac{1}{\rho c}\frac{\partial}{\partial z}\left[\lambda_{\mathrm{h}}\frac{\partial T_{\mathrm{soil}}}{\partial z} + E_q \rho_{\mathrm{w}} c_{\mathrm{w}} \overline{T}_{\mathrm{soil}}\right] . \tag{2.71}$$

T_{soil} is the absolute temperature in the kth soil layer in [K], $\overline{T}_{\mathrm{soil}}$ is the mean soil temperature of two neighboring soil layers. The change in internal energy due to changes in moisture by the inner soil water flux, evapotranspiration and evaporation from the upper soil layer and the interception reservoir is treated by the second term in square brackets. The heat conductivity λ_{h} and the volumetric heat capacity ρc are variables that depend on the soil texture. The heat capacity of the soil ρc formulated by Chen and Dudhia (2001) is the sum of the heat capacity of dry soil ($\rho_0 c_0$), the heat capacity of wet soil ($\rho_{\mathrm{w}} c_{\mathrm{w}}$) and the heat capacity of the air within the soil pores ($\rho_{\mathrm{a}} c_{\mathrm{a}}$).

$$\rho c = W_{\mathrm{soil}} \rho_{\mathrm{w}} c_{\mathrm{w}} + (1 - W_{\mathrm{pv}})\, \rho_0 c_0 + (W_{\mathrm{pv}} - W_{\mathrm{soil}})\, \rho_{\mathrm{a}} c_{\mathrm{a}} \tag{2.72}$$

with W_{pv} corresponding to the soil pores and $\rho_{\mathrm{w}} c_{\mathrm{w}} = 4.18 \times 10^6\,\mathrm{J\,m^{-3}\,K^{-1}}$ and $\rho_{\mathrm{a}} c_{\mathrm{a}} = 1298\,\mathrm{J\,m^{-3}\,K^{-1}}$. The heat conductivity λ_{h} is defined after Pielke (1984):

$$\lambda_{\mathrm{h}} = \begin{cases} 418 \exp\{-\Psi_{\log} - 2.7\} & \text{if } \Psi_{\log} \leq 5.1 \\ 0.172 & \text{if } \Psi_{\log} > 5.1 \end{cases} \tag{2.73}$$

with $\Psi_{\log} = \log_{10} |100\Psi_{\mathrm{soil}}|$.

The topmost layer is exposed to the incoming radiation and thus has the strongest variation in temperature in comparison to the other soil layers within the ground. The temperature equation of the first layer is, in addition to the incoming radiation, determined by the latent and sensible heat flux.

$$\frac{\partial T_{\mathrm{soil},1}}{\partial t} = \frac{1}{\rho c}\frac{\partial}{\partial z}\left[\left(\lambda_{\mathrm{h}}\frac{\partial T_{\mathrm{soil},1}}{\partial z}\right) + \Delta Q\right] \tag{2.74}$$

with

$$\Delta Q = Q_{\mathrm{dir}} + Q_{\mathrm{dif}} - \sigma T_{\mathrm{sfc}}^4 - c_p Q_{\mathrm{Sens}} - L_{\mathrm{v}} Q_{\mathrm{Lat}} \tag{2.75}$$

Here Q_{Lat} is the latent heat flux, describing the moisture flux between soil and atmosphere as the sum of evaporation and transpiration and Q_{Sens} is the sensible heat flux. Q_{dir} and Q_{dif} represents the direct and diffusive irradiation, respectively.

2.8 Test cases

Idealized test cases are a useful tool for numerical models to evaluate parts of the model formulation. In some cases, an analytical solution of the case is available, which enables an easy comparison with modeling results. But even if there is no analytical solution, results produced by different models can be compared with each other and evaluated with respect to physical considerations or symmetry criteria. In this section, six example test cases are presented. In five of these cases, orography or obstacles are included to test conservation properties and model accuracy. The first test case is rising heat bubble prescribed in Wicker and Skamarock (1998). The bubble is initially defined by a radial temperature perturbation, which leads to rising motion due to buoyant forces. This test can be used to check the correctness and accuracy of the discretization schemes. The next test case simulates two-dimensional gravity waves (Schaer et al., 2002) induced by an idealized mountain ridge. Two sub-cases with different atmospheric stabilities and reference temperatures are examined. The third case is a sinking cold bubble in a dry environment, from which a density current develops (Straka et al., 1993). A 1 km tall hill is added at the left side of the domain so that the resulting current overflows over the mountain. Considering moisture effects and phase changes, the moist bubble case by Bryan and Fritsch (2002) with the addition of a mid-air zeppelin (Klein et al., 2009; Jebens et al., 2011) is performed. Besides analyzing the flow field in the vicinity of the obstacles, conservation studies regarding total energy are performed for both cases. Another idealized benchmark case is carried out to analyze the accuracy of the presented discretization method for cut cells. There, a scalar field is advected by a radial wind field in an annulus

(Berger and Helzel, 2012). This is also a suitable test for convergence studies by calculating L_1 and L_∞ error norms since an analytical solution can be used for comparison. The last test case is a three-dimensional simulation study regarding flow dynamics around an idealized mountain and orographic precipitation by Kunz and Wassermann (2011).

2.8.1 Dry bubble

A two-dimensional simulation of a rising thermal is presented in Wicker and Skamarock (1998). This test case is also used as dry reference case for the moist bubble simulation in Bryan and Fritsch (2002). The domain is 20 km in horizontal direction and 10 km in vertical direction with a uniform grid spacing of 125 m. A mean flow of $U = 20\,\mathrm{m\,s^{-1}}$ is applied. After 1000 s the bubble has been transported through the lateral periodic boundaries and is again located at the center of the domain. The perturbation field takes the following form:

$$\theta' = 2\cos^2\left(\frac{\pi L}{2}\right) \tag{2.76}$$

with

$$L = \sqrt{\left(\frac{x - x_\mathrm{c}}{x_\mathrm{r}}\right)^2 + \left(\frac{z - z_\mathrm{c}}{z_\mathrm{r}}\right)^2} \leq 1\,. \tag{2.77}$$

The parameters $x_\mathrm{c} = 10\,\mathrm{km}$, $z_\mathrm{c} = 2\,\mathrm{km}$ and $x_\mathrm{r} = z_\mathrm{r} = 2\,\mathrm{km}$ determine the position and radius of the heat bubble. The atmosphere is in hydrostatic balance and neutrally stable with a surface pressure $p_0 = 1000\,\mathrm{hPa}$ and a constant potential temperature $\theta = 300\,\mathrm{K}$. Results of this simulation are displayed in Fig. 2.7. The overall shape is reproduced and comparable to the reference solution. Slight asymmetries are observed due to lateral transport. However, it becomes apparent that third-order Runde–Kutta time integration together with a fifth-order advection scheme produces better results in terms of minimum/maximum values and symmetry (cf. Bryan and Fritsch, 2002) than the third-order advection scheme that is used here.

2.8.2 2-D mountain gravity waves

In this test case, a flow over a mountain ridge is simulated (Schaer et al., 2002). Skamarock et al. (2012) A dry stable atmosphere is defined by a constant Brunt–

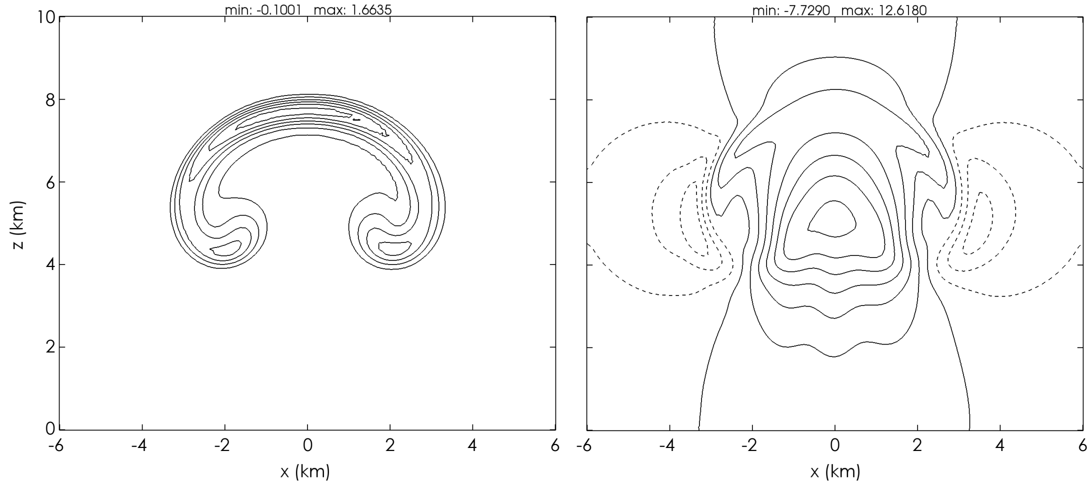

Figure 2.7: Results for the dry bubble simulation after Wicker and Skamarock (1998) at $t = 1000$ s: contours of perturbation potential temperature (left panel) and vertical velocity (right panel). Solid (dashed) lines indicate positive (negative) values. Contour intervals are 0.25 K (zero contour omitted) and 2 m s^{-1}, respectively.

Väisälä frequency N, upstream surface temperature T_0, surface pressure p_0 and a uniform inflow velocity U. The domain extends 200 km horizontally and 19.5 km vertically with grid spacings of $\Delta x = 500$ m and $\Delta z = 300$ m. The structure of the mountain ridge is represented by a bell curve shape with superposed variations:

$$h(x) = h_0 \exp\left(-[x/a]^2\right) \cos^2\left(\pi x/\lambda\right) \tag{2.78}$$

with $h_0 = 250$ m, $a = 5$ km and $\lambda = 4$ km. The simulation result for the steady state is shown in Fig. 2.8. There are no non-physical distorted wave patterns and the result agrees well with the analytical and reference solutions shown in Schaer et al. (2002).

2.8.3 Cold bubble with orography interaction

A non-linear test problem is the density current simulation study documented in Straka et al. (1993). In this case, the computational domain extends from -18 to $+18$ km in horizontal direction and from 0 to 6.4 km in vertical direction with isotropic grid spacing of $\Delta x = \Delta z = 100$ m. Boundary conditions are periodic in x-direction and the free-slip condition is applied for the top and bottom model

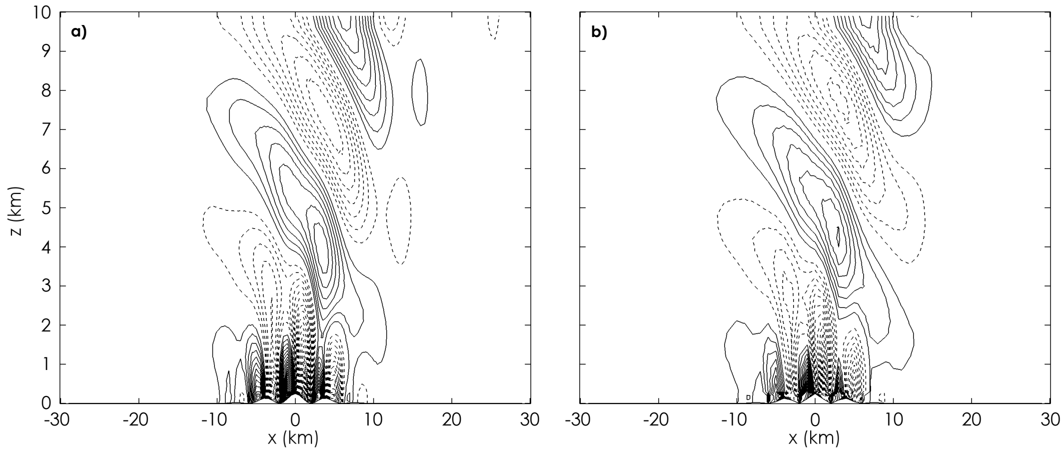

Figure 2.8: Steady-state solution for the simulation of the Schaer et al. (2002) test case: contours of vertical velocity for a) $N = 0.01\,\mathrm{s}^{-1}$ and b) $N = 0.01871\,\mathrm{s}^{-1}$. Solid (dashed) lines indicate positive (negative) values. Contour intervals are a) $0.05\,\mathrm{m\,s}^{-1}$ and b) $0.09355\,\mathrm{m\,s}^{-1}$, respectively.

boundary. The total integration time is $t = 1800\,\mathrm{s}$. The initial atmosphere is in a dry and hydrostatically balanced state and there is a horizontally homogeneous environment with $\overline{\theta} = 300\,\mathrm{K}$ (i.e., neutrally stratified). The perturbation (cold bubble with negative buoyancy) is defined by a temperature perturbation of

$$T' = \begin{cases} 0.0\,^\circ\mathrm{C} & \text{if } L > 1.0, \\ -15.0\,^\circ\mathrm{C}(\cos[\pi L] + 1.0)/2 & \text{if } L \leq 1.0 \end{cases} \tag{2.79}$$

where

$$L = \left(\left[(x - x_\mathrm{c}) x_\mathrm{r}^{-1} \right]^2 + \left[(z - z_\mathrm{c}) z_\mathrm{r}^{-1} \right]^2 \right)^{0.5} \tag{2.80}$$

and $x_\mathrm{c} = 0.0\,\mathrm{km}$, $x_\mathrm{r} = 4.0\,\mathrm{km}$, $z_\mathrm{c} = 3.0\,\mathrm{km}$ and $z_\mathrm{r} = 2.0\,\mathrm{km}$. At first, there is no fixed physical viscosity turned on like in the original test case (with $\nu = 75\,\mathrm{m}^2\,\mathrm{s}^{-1}$) since a conservation test regarding total energy is carried out. For this test, two simulation runs are performed with a) the above described standard setup and b) a modificated setup where a mountain is added at the left part of the domain. The mountain follows the 'Witch of Agnesi' curve:

$$h(x) = \begin{cases} H/(1 + [(x - x_M)/a_1]^2) & \text{if } x < x_M, \\ H/(1 + [(x - x_M)/a_2]^2) & \text{if } x \geq x_M \end{cases} \tag{2.81}$$

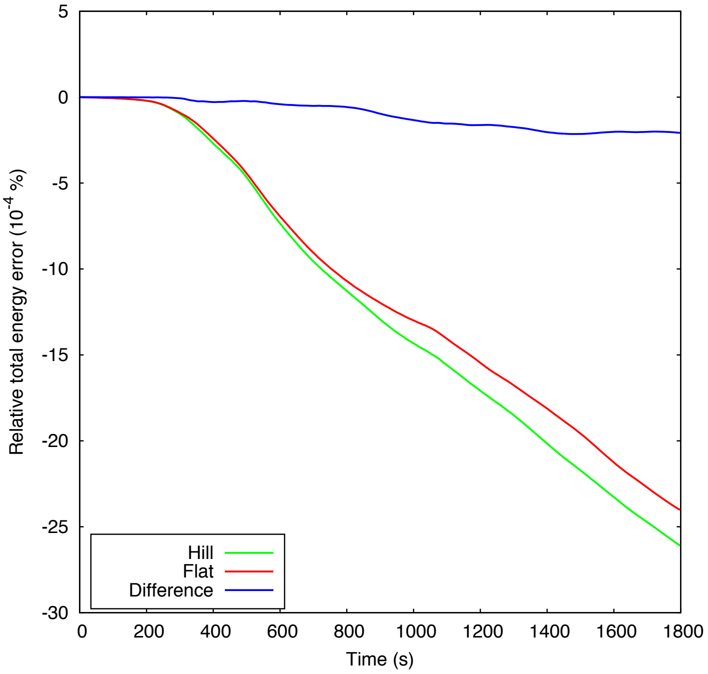

Figure 2.9: Time series of total energy error for the density current test case with and without the hill. The error is expressed as 10^{-4} % of the total energy at the beginning of the simulation.

with half-width lengths $a_1 = a_2 = 1$ km, mountain peak center position $x_M = -6$ km and mountain height $H = 1$ km. Fig. 2.9 shows the temporal evolution of the total energy error for both simulations. In a dry atmosphere, the total energy is

$$E_d = \rho(q_d c_{vd} T + gz + 0.5|\vec{v}|^2) \tag{2.82}$$

Since exact energy conservation is not expected due to the model design, there is some kind of energy loss for both simulations in the order of 10^{-3} % at the end of the integration time. However, this is still acceptable due to the fact that in the test case there are very sharp gradients in potential temperature and wind speeds. Also, the difference of the total energy error between the two cases is very small (10^{-4} %). This means that in this case, cut cells do not affect the conservation properties in the model at all. Total mass is always conserved within machine precision.

Another analysis is carried out by switching on the physical viscosity of $\nu = 75\,\mathrm{m^2\,s^{-1}}$ like in Straka et al. (1993). Four simulations are performed with different isotropic grid spacings of 200 m, 100 m, 50 m and 25 m, respectively. The potential temperature field after 900 s integration time for these spatial resolutions

Table 2.4: Convergence study for the density current test case with a 1 km tall hill. Minimum/maximum values of horizontal velocity and potential temperature for different grid spacings.

Δx	u_{min} ($\mathrm{m\,s^{-1}}$)	u_{max} ($\mathrm{m\,s^{-1}}$)	θ_{min} (K)	θ_{max} (K)
200	−25.93	35.64	291.89	300.01
100	−28.87	38.52	290.85	300.01
50	−28.90	38.31	290.71	300.00
25	−28.91	37.89	290.70	300.00

is shown in Fig. 2.10. Table 2.4 shows minimum/maximum values of horizontal wind speed and potential temperature at this time. Skamarock et al. (2012) pointed out that their solutions show convergence at the 50 m spacing for this test case (without hill) with a fully compressible nonhydrostatic model. The same behavior can be observed with ASAM simulations (not shown here), which does also not change when the mountain is added to the domain. Despite there is a slight change in maximum wind speed, the potential temperature field for the 25 and 50 m resolutions are nearly identical. Some notable differences in the field can be observed for the 100 m resolution, which is even more pronounced for the 200 m simulation.

2.8.4 Moist bubble with mid-air zeppelin

The moist bubble benchmark case after Bryan and Fritsch (2002) is based on its dry counterpart described in Wicker and Skamarock (1998). There, a hydrostatic and neutrally balanced initial state is realized by a constant potential temperature. A warm perturbation in the center of the domain leads to the rising thermal. For the present test case, a moist neutral state can be expressed with the equivalent potential temperature θ_{e} and two assumptions: the total water mixing ratio $r_{\mathrm{t}} = r_{\mathrm{v}} + r_{\mathrm{l}}$ remains constant and phase changes between water vapor and liquid water are exactly reversible. The perturbation field is identical to the dry bubble test case (Eq. (2.76) and (2.77)) The domain is 20 km long in x direction and the vertical extent is 10 km. Grid spacing is again isotropic with $\Delta x = \Delta z = 100\,\mathrm{m}$. Periodic boundary conditions are applied in lateral direction, whereas free-slip conditions are used for the top and bottom boundary. Again, a total energy test is performed by comparing two modifications of the present test case: a) A uniform

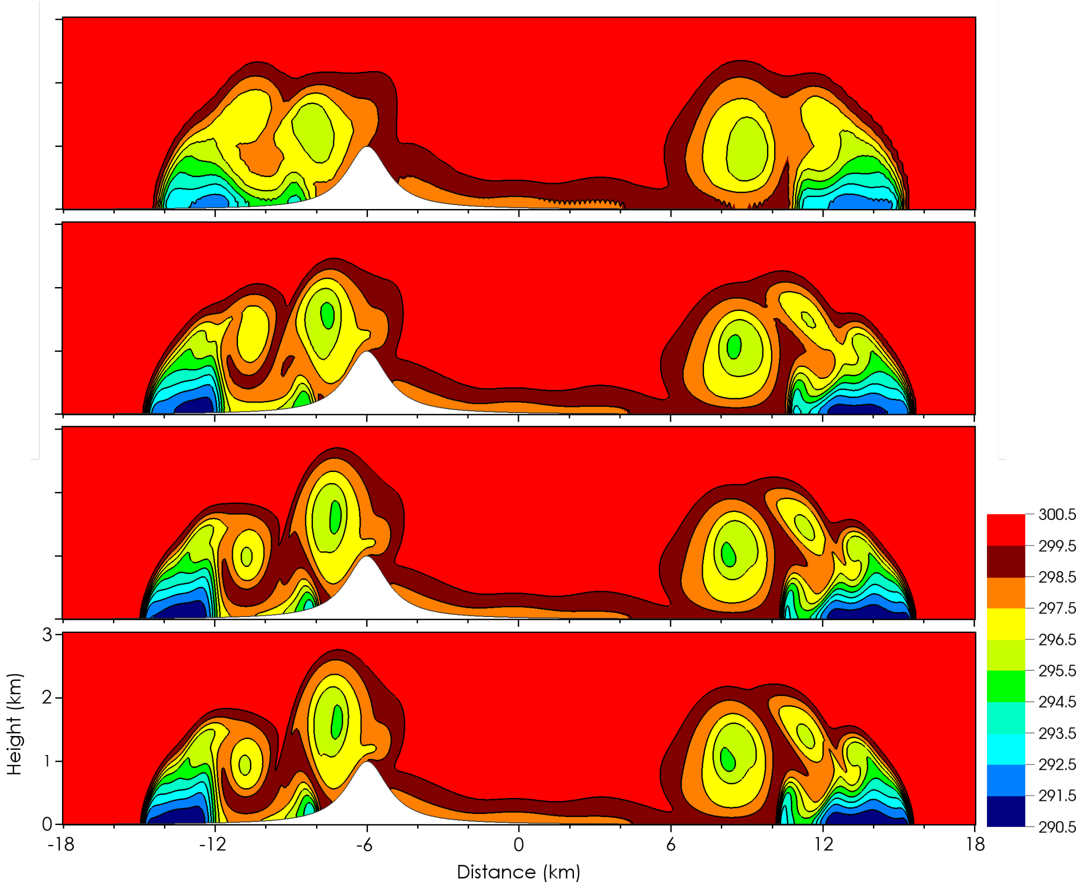

Figure 2.10: Potential temperature field at $t = 900\,\mathrm{s}$ for the density current test case with an 'Agnesi' hill on the left side of the domain and for different grid spacings $\Delta x = \Delta z = 200,\ 100,\ 50,\ 25\,\mathrm{m}$ (top to bottom).

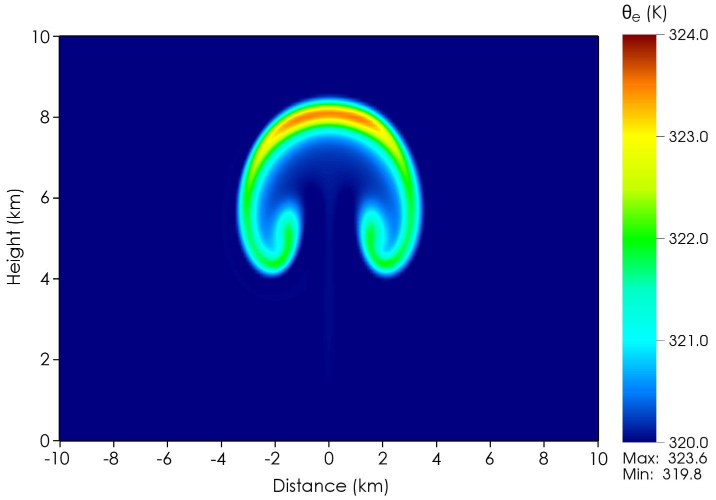

Figure 2.11: Equivalent potential temperature field for the moist rising bubble test case with background wind of $U = 20\,\mathrm{m\,s^{-1}}$. Snapshot taken at $t = 1000\,\mathrm{s}$ simulation time.

horizontal wind speed of $U = 20\,\mathrm{m\,s^{-1}}$ is applied. With that, the center of the bubble is again located at $x = 0\,\mathrm{m}$ at $t = 1000\,\mathrm{s}$ after passing through the periodic boundaries. b) In the center of the domain, a zeppelin-shaped region is cut out and acts as an obstacle for the rising bubble. A similar test like this was already introduced in Klein et al. (2009) and Jebens et al. (2011). However, their tests were carried out with the dry bubble, which was also shifted 1 km to the left. The result for the first case is shown in Fig. 2.11. The equivalent potential temperature field is very close to the benchmark simulation, despite the maximum value of θ_e is a little bit lower in our case compared to the literature values and there is a slight asymmetry at the top of the thermal due to lateral transport.

The position of the rising thermal for the zeppelin case after $t = 1250\,\mathrm{s}$ is shown in Fig. 2.12. Because of the centered obstacle, the bubble is split up into two parts and deformed, but still two typical rotors are formed by each bubble and the result remains symmetric. When moisture and liquid water are present, the total energy can be expressed in the form of

$$E_t = \rho\left(\left[q_d c_{vd} + q_v c_{vv} + q_l c_{pl}\right] T + q_v L_{00} + gz + 0.5|\vec{v}|^2\right) \tag{2.83}$$

Again, energy is not fully conserved, but the total relative energy error after 2000 s simulation time (there, in both cases, the bubbles reach the top boundary resulting in zonal divergence) stays in an acceptable range of $10^{-4}\,\%$ (Fig. 2.13), which is one order of magnitude smaller than in the cold bubble test case. The difference

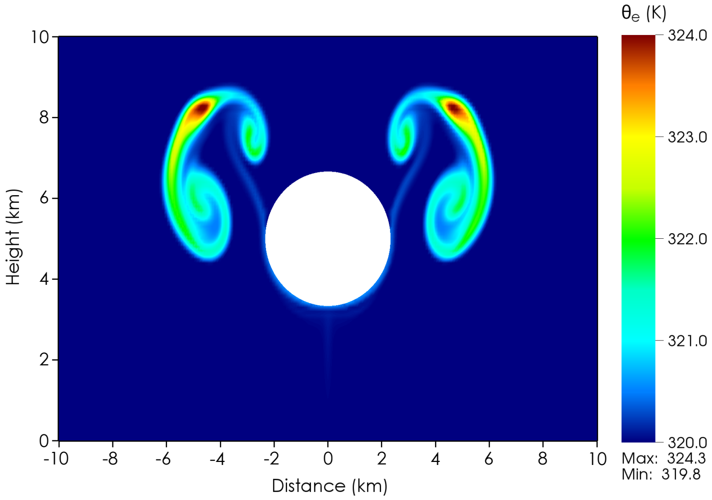

Figure 2.12: Equivalent potential temperature field for the moist rising bubble test including a zeppelin-shaped cut area in the center of the domain. Snapshot taken at $t = 1250\,\mathrm{s}$ simulation time.

of the error in total energy between the zeppelin and the classical case is again very small. So even with very small cut cells ($\approx 1\,\%$ of full cell volume) and microphysical conversions there is no indication that conservation properties are deteriorated. For all cases, total mass is conserved within the numerical accuracy. After Bryan and Fritsch (2002), both mass and energy conservation are required to obtain the benchmark result.

2.8.5 Annulus advection test

The test problem reported in Berger and Helzel (2012) describes the advection of a smooth bump by a radial wind field in an annulus. It is described by the radius of the inner circle $R_1 = 0.75$ and the radius of the outer circle $R_2 = 1.25$ within a rectangular domain $[-1.5,\, 1.5] \times [-1.5,\, 1.5]$. The initial scalar field takes the following form:

$$\phi = 0.5\,(\mathrm{erf}\,[5\,\{\vartheta - \pi/3\}] + \mathrm{erf}\,[5\,\{2\pi/3 - \vartheta\}])\ , \tag{2.84}$$

where $\vartheta = \arctan(y/x)$. Deriving the velocity field from the stream function $\psi(x, y) = \pi(R_2^2 - r^2)/5$ with $r = (x^2 + y^2)^{1/2}$, one full rotation is reached at $t = 5\,\mathrm{s}$. Figs. (2.14a-e) show the difference fields between the analytical and numerical solution ($\Delta\phi$) for different mesh sizes, where N is the amount of grid

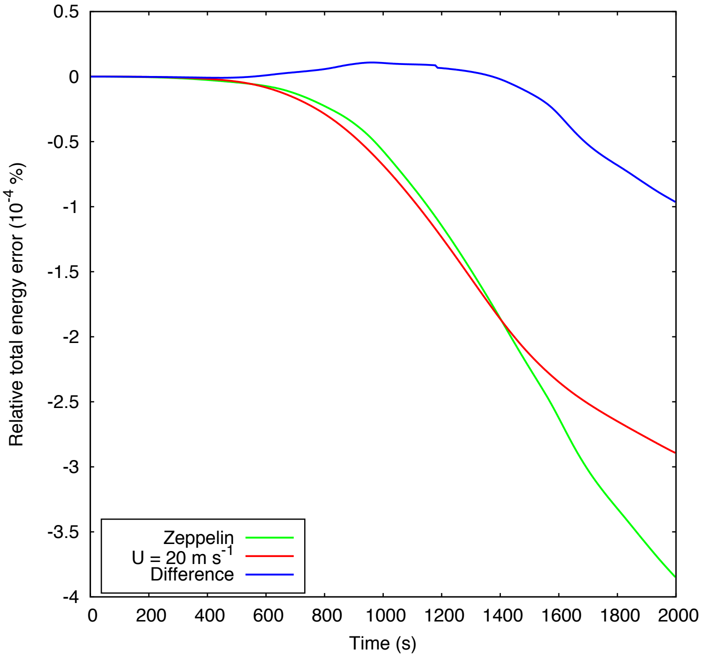

Figure 2.13: Same as Fig. 2.9, but for the zeppelin and the lateral transported moist bubble test cases.

cells in each spatial direction. Fig. (2.14f) shows the final field after 5 s integration time for $N = 400$. With greater N, the order of magnitude of the error reduces for the inner and outer boundary and the intermediate part of the annulus is less affected. Table 2.5 shows the results of the convergence study, including error norms, experimental orders of convergence (EOC) as well as minimum and maximum values of the tracer field for different mesh sizes. For a fixed time step (0.01, 0.005, 0.0025 and 0.00125 s, respectively) the advection scheme used in ASAM together with the Koren limiter shows almost second order convergence in the L_1 norm, whereas the L_∞ norm is nearly first order accurate (see Fig. 2.15).

2.8.6 3-D mountain flow in a moist atmosphere

In this section, a test case described in Kunz and Wassermann (2011) is chosen. It includes forced lifting around a 1 km high mountain (see Fig. 2.16), latent heat release and orographic precipitation. Compared to the first three test cases, this case is now three-dimensional and uses a more realistic initial profile, which mimic atmospheric conditions when it comes to orographically-dominated precipitation

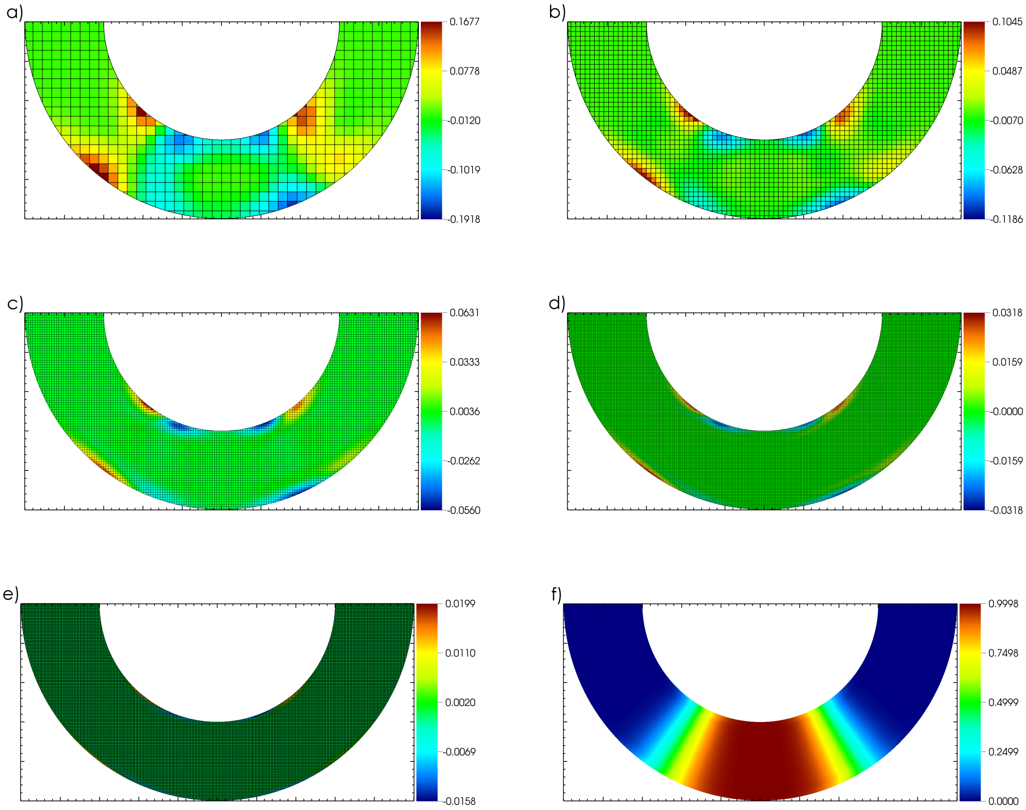

Figure 2.14: Computational meshes and difference scalar fields of ϕ for a) $N = 50$, b) $N = 100$, c) $N = 200$, d) $N = 400$, e) $N = 800$, f) scalar field for $N = 400$ after one rotation.

Table 2.5: Convergence study for the annulus advection test. L_1 error norm (full domain), experimental order of convergence (EOC), L_∞ error norm, minimum and maximum tracer values for different meshes.

N	Domain L_1 error	EOC	L_∞ error	ϕ_{min}	ϕ_{max}
50	1.6377×10^{-2}	–	1.9176×10^{-1}	-2.0022×10^{-3}	1.00048
100	4.9439×10^{-3}	1.73	1.1860×10^{-1}	-8.3884×10^{-4}	1.00066
200	1.3653×10^{-3}	1.86	6.3112×10^{-2}	-8.5424×10^{-13}	0.99977
400	3.7196×10^{-4}	1.88	3.1822×10^{-2}	-2.6209×10^{-16}	0.99977
800	9.7302×10^{-5}	1.93	1.9877×10^{-2}	-1.0274×10^{-12}	0.99978

in the mountainous area of southwest Germany. In their work, they used the three-dimensional, non-hydrostatic weather prediction model COSMO with terrain-following coordinates to describe the orography of the idealized mountain. The model setup for the ASAM simulations is as follows: the domain extends 553 km × 553 km with a horizontal grid spacing of 2.765 km and 70 vertical layers with uniform spacing of $\Delta z = 200\,\text{m}$. A Bell-shaped mountain is located at the center of the domain:

$$h(x,y) = \frac{H}{\left(\frac{x^2+y^2}{a^2}+1\right)^{1.5}} \tag{2.85}$$

with the mountain peak height $H = 1\,\text{km}$ and the half-width length $a = 11\,\text{km}$. Inflow and outflow boundary conditions are set according to the initial conditions. A Rayleigh damping layer above 11 km is applied to suppress gravity wave reflections from the top boundary. Surface heat fluxes and Coriolis force are turned off. For turbulence parameterization, the standard Smagorinsky subgrid-scale model is used. Microphysics are parameterized by the warm (i.e., no ice phase present) two-moment scheme described in Section 2.7.2. Initial profiles are obtained by assuming hydrostatic equilibrium, a near-surface temperature $T_s = 283.15\,\text{K}$, a constant mean flow $U = 10\,\text{m}\,\text{s}^{-1}$, a constant dry static stability $N_d = 11 \times 10^{-3}\,\text{s}^{-1}$ and a relative humidity profile, which is constant up to $z_m = 5\,\text{km}$ and rapidly decreases above this level according to

$$\text{RH}(z) = \text{RH}_\text{S}\left[0.5 + \pi^{-1}\arctan\left(\frac{z - z_m}{500}\right)\right] \tag{2.86}$$

with the near-surface humidity $\text{RH}_\text{S} = 95\,\%$ (RH95 case). To compare the results with its dry counterpart, another simulation with $\text{RH}_\text{S} = 50\,\%$ is performed (RH50 case). Fig. 2.17 shows the wind field at 200 m height around the mountain for

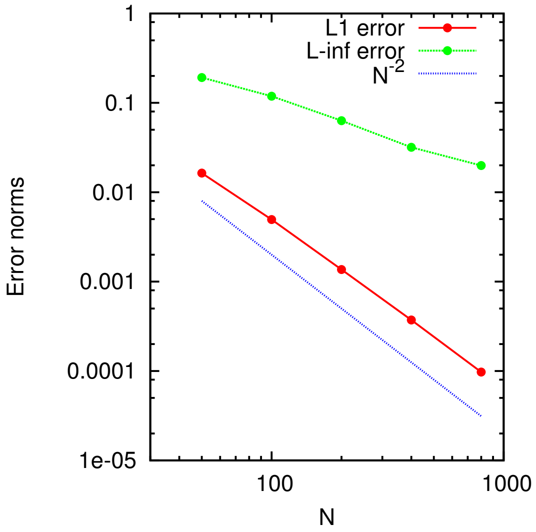

Figure 2.15: Convergence study for the annulus advection test. L1 (red) and L-infinity (green) error norms for the full domain and reference line (blue dotted) for "perfect" 2nd order convergence.

both cases. In the nearly saturated atmosphere, there is a more direct overflow over the mountain, which is caused by the reduced stability due to high moisture. These different flow characteristics also affect gravity wave structure (Fig. 2.18). The resulting waves are steeper and have a greater wave length, which is in agreement with gravity wave theory and the results from Kunz and Wassermann (2011). Most notable differences in the numerical results are discrepancies in vertical wind strength in the lowest model layer at the windward side the mountain ($w \approx 0.6\,\mathrm{m\,s^{-1}}$ in ASAM vs. $w \approx 0.2\,\mathrm{m\,s^{-1}}$ in COSMO), which can be explained by the different surface coordinate systems of the models (Cartesian grid with cut cells in ASAM and generalized terrain-following coordinates in COSMO). Overall, the amplitude of vertical wind is higher for the resulting gravity waves. Typical patterns of orographic clouds (one cloud upstream of the mountain and a larger cloud with a high amount of liquid water content (LWC) and precipitation that reaches the ground in the lee of the mountain) are also reproduced (Fig. 2.19). In this particular case the resulting patterns as well as the cloud and rain water contents are comparable to the literature results, despite using different coordinate systems and cloud microphysical schemes.

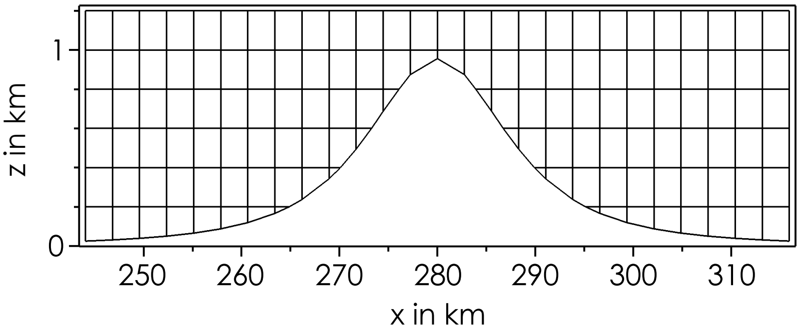

Figure 2.16: Computational grid around the mountain for an x-z cut plane at $y = 1.38\,\text{km}$ (cell center).

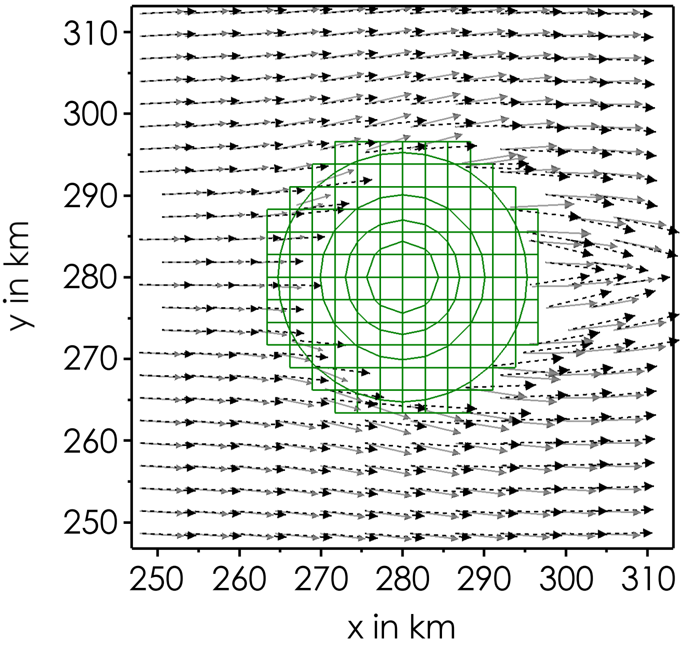

Figure 2.17: Horizontal cross-section of horizontal wind vectors at $z = 200$ m height for the RH95 case (black) and the RH50 case (gray). Surface grid cells around the mountain in green, circle lines represent 200 m orography intervals.

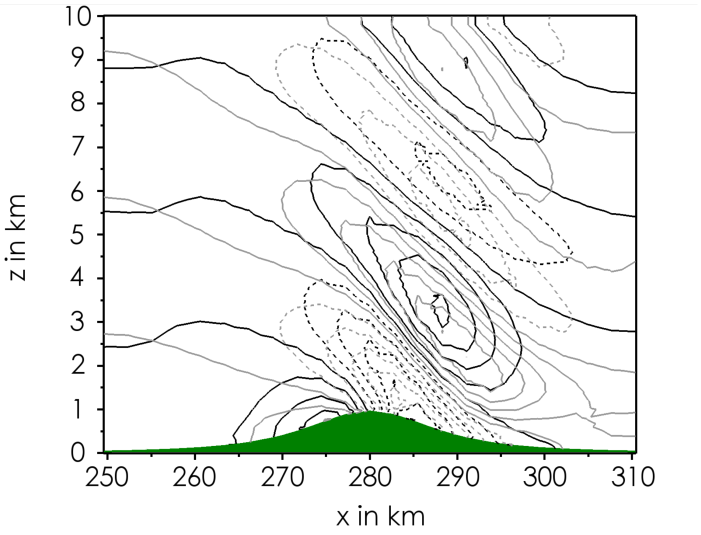

Figure 2.18: Vertical cross-section (x-z plane) of vertical wind speed for the RH95 case (black) and the RH50 case (gray). Updrafts in solid lines (0.2 m s^{-1} contour interval, zero line included), downdrafts in dashed lines (0.2 m s^{-1} contour interval, zero line excluded).

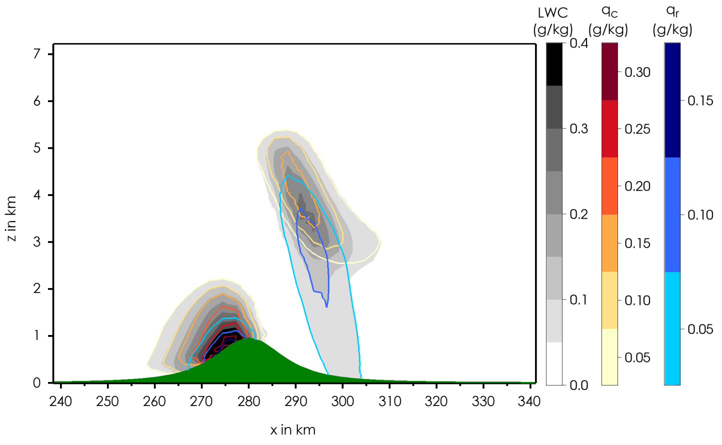

Figure 2.19: Vertical cross-section (x-z plane) of microphysical properties for the RH95 case. Liquid water content (shaded), contours of specific cloud water content q_c (red-yellow) and specific rain water content q_r (blue).

2.9 Code availability and visualization

The ASAM code is managed with Git, a distributed revision control and source code management (SCM) system. To get access to the source code and additional scripts for pre- and postprocessing, a registration at the TROPOS Git hosting website `https://gitorious.tropos.de/` is mandatory. Additional information can be found at the ASAM webpage (`http://asam.tropos.de`).

As visualization tool, the free and open source software VisIt (`https://wci.llnl.gov/codes/visit/`) is used. VisIt can read over 120 scientific file formats and offers opportunity to include own scripts, if necessary. It is available for Unix, Windows and Mac workstations.

Chapter 3

The SALTRACE field campaign and data base

3.1 The SALTRACE field campaign

The Saharan Aerosol Long-range Transport and Aerosol Cloud Interaction Experiment (SALTRACE) is an initiative of the German Aerospace Center (*Deutsches Zentrum für Luft- und Raumfahrt*, DLR) and the Leibniz Institute for Tropospheric Research (TROPOS) Leipzig. It is additionally supported by scientists from the Ludwig-Maximilians-Universität (LMU) Munich, the Technische Universität (TU) Darmstadt, the Max Planck Institute for Meteorology (MPI-M) Hamburg, the University of Valladolid (UVa), the Caribbean Institute for Meteorology and Hydrology (CIMH) at Barbados, the University of Puerto Rico (UPR), the Laboratoire Interuniversitaire des Systèmes Atmosphériques (LISA) Paris and the National Aeronautics and Space Administration (NASA). The main purpose of the campaign is to investigate the physical, chemical and optical properties of dust in the Saharan air layer (SAL) and its distribution. These studies should give a better understanding of the impact of mineral dust on the radiation budget and atmospheric dynamics within the area of transport at 2,000–8,000 km west of the dust sources over the tropical Northern Atlantic. The specific objectives of SALTRACE can be summarized as follows:

- Investigation of dust transport and changes in dust properties during long-range transport.
- Impact of cloud processes, sedimentation, and turbulent downward mixing

on aerosol vertical distribution and removal of dust.

- Impact of aged Saharan dust on the radiation field and atmospheric dynamics (and feedbacks on dust transport).
- Impact of aged Saharan dust on cloud processes: cloud condensation nuclei (CCN) characterization, heterogeneous ice formation in layered clouds.

For this large field experiment, researchers from the above-mentioned institutes used state-of-the-art active remote sensing and ground-based and airborne in-situ particle measurement instrumentation at the Caribbean island of Barbados (13° 10' N; 59° 32' W) in June/July 2013. This first campaign is further denoted as SALTRACE-1. Two additional campaigns were carried out in February/March 2014 (SALTRACE-2) and June/July 2014 (SALTRACE-3) solely by TROPOS to extend the data base and enable comparisons with the winter data set, where the aerosol composition and also the meteorological situation is different.

Multiple aspects of dust aging, mixing of desert dust with marine and African smoke particles (during the winter half year), and downward transport of dust particles from the SAL to the ocean surface (removal of dust) can be investigated within the long-range transport regime over the tropical North Atlantic. It is also possible to study aerosol transformation processes in clear and cloudy air during an average stay of 10 days during the travel over the Atlantic under nearly undisturbed conditions. There are no significant anthropogenic aerosol sources between the west coast of Africa and Barbados for more than 4,000 km making it an ideal site to investigate advected dust layers. Moreover, the west-to-east research vessel "Meteor" cruise can be considered as a unique SALTRACE contribution along the main Saharan dust transport route. In the end, the generated measurement data are connected with mesoscale model transport simulations and high-resolution large eddy simulations.

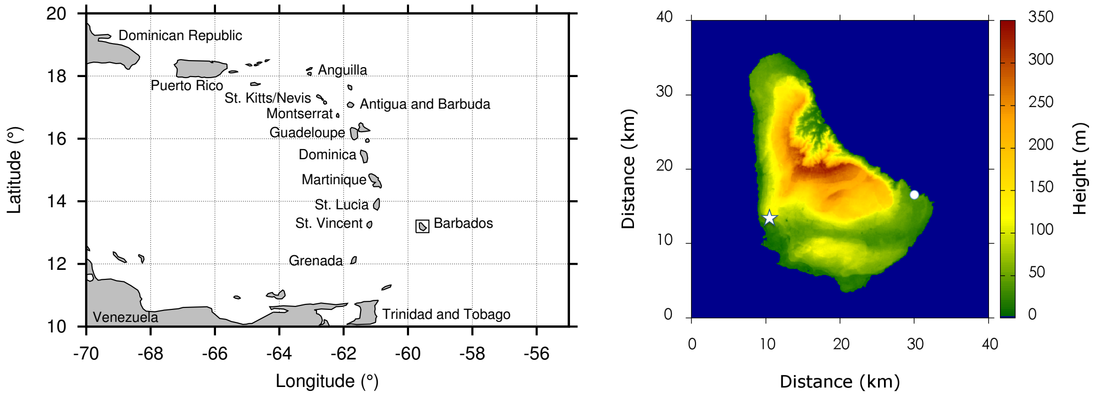

Figure 3.1: Left panel: part of the Caribbean including the Lesser Antilles. Right panel: topographical map of Barbados. The topographical data is obtained from the Consortium for Spatial Information (CGIAR-CSI) Shuttle Radar Topography Mission (SRTM) dataset at 200 m resolution. The white star denotes the location of the CIMH, which is close to the measurement field site. The white circle denotes the location of Ragged Point Station.

3.2 Measurements at and around Barbados during SALTRACE

3.2.1 Terrain characteristics and field site

Barbados is affected by steady trade-wind conditions for about half the year since it lies on the edge of the Atlantic Intertropical Convergence Zone (ITCZ). Unlike the other "Windward Islands", which are located approximately 100 km west of Barbados and are volcanic in origin with peaks up to 1500 m, Barbados is relatively flat. The elevations in the islands interior have an L-shaped pattern and range from 180 to 240 m height (Fig. 3.1). The highest elevation, Mt. Hillaby, is at 340 m asl. Most parts of the land surface are of limestone together with accumulated sediment. A major part of the limestone surfaces is used for sugarcane plantings. The Ragged Point station (13° 09' 54" N; 59° 26' 31" W) is located at the rough and steeper east coast, whereas the TROPOS field site at the CIMH (13° 08' 57" N; 59° 37' 28" W) lies at the most densely populated part of the island in the southwest.

3.2.2 Instrument specifications

During SALTRACE-1, altogether 14 research flights were performed in the Caribbean region with the Falcon aircraft from the DLR. The measurement systems installed on board the research aircraft are able to detect aerosols with particle sizes D_p between 4 nm and 50 µm in diameter directly within the dust layer. Besides other instruments, which measure chemical composition, shape, volatility, absorption properties and CCN number concentrations, a 2-µm doppler wind lidar resolves the horizontal and vertical wind velocity structure and provides an insight of the vertical extent of dust layers. A complete overview of the instrumentation on board the Falcon aircraft is shown in Table 3.1.

Several dust outbreaks of different intensity have been observed during the campaign. Figure 3.2 shows the time series of aerosol optical depth (AOD) τ_{AOD} at Ragged Point. The AOD is a measure of radiation extinction due to the interaction of radiation with aerosol particles and is defined as the integrated extinction coefficient over a vertical column. AOD values of $\tau_{\mathrm{AOD}} < 0.1$ most likely indicate that no or only a small portion of dust is present. These values are often observed during winter months and partly during summer. Most of the time, a dust load can be seen in the data where $0.2 < \tau_{\mathrm{AOD}} < 0.5$. Peak values of $\tau_{\mathrm{AOD}} > 0.5$ with a corresponding high dust load were reached at least 10 times during June and July 2013. The periodical pattern in Fig. 3.2 was caused by changes in the synoptic situation, where westward traveling easterly waves influenced the local weather every 3 to 4 days. Furthermore, the vertical profile of the extinction coefficient itself is another indication for dust aerosol.

The atmospheric research station at Ragged Point consists of aerosol inlets and in-situ instruments placed on a 50 m high tower and in a cabinet, respectively. With this system, the size-resolved composition and especially the dust concentration of the aerosol mixture can be obtained. Moreover, CCN number concentrations were measured continuously with a CCN counter at ground level for different supersaturations throughout the campaign. Further specifications of the instruments can be found in Tab. 3.2.

The focus of vertical profiling of the atmosphere with respect to meteorological values and aerosol distribution was realized by instruments at the CIMH campus near the west coast (cf. Fig. 3.3). The BERTHA (TROPOS Leipzig) and Polis (LMU Munich) lidars operated at three and two wavelengths, respectively.

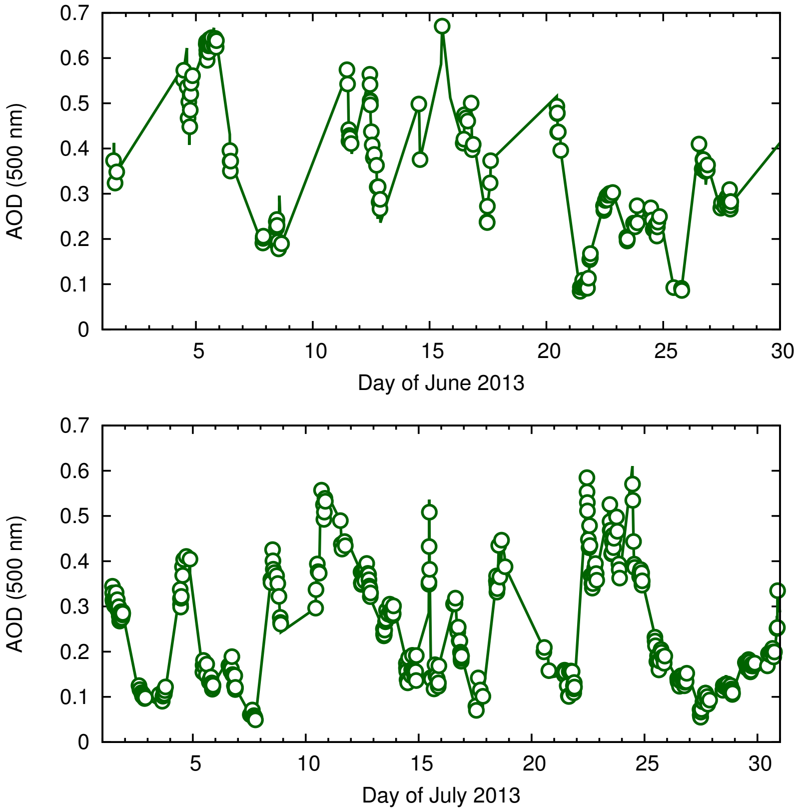

Figure 3.2: Time series of aerosol optical depth (AOD) measured with the AERONET sun photometer (level 2.0 data) at Ragged Point for June (top) and July (bottom) 2013. Data courtesy of Joe Prospero, University of Miami.

Figure 3.3: TROPOS lidar and photometer station at the CIMH, 21 km west of Ragged Point. Left image: daytime photograph with typical trade-wind cumuli, view in south direction. Right image: nighttime photograph with running BERTHA-Lidar, view in west direction.

Furthermore, sun photometers enabled additional AOD measurements, which can be compared with the ones from the AERONET station at Ragged Point. At least two radiosonde launches per day were released during the campaign time, which are used later on to initialize the model simulations. Table 3.3 summarizes the devices used at this field site.

Table 3.1: Instrumentation on board the Falcon research aircraft (SALTRACE-1)

Instrument	**Output**
Aerosol in-situ instruments inside the cabin behind an isokinetic inlet ($D_p <$ 2.5 μm)	
Multi-channel CPC (3 unheated, 1 heated channels, 1 reference CPC for CCNC)	Integral number concentration of ultrafine particles (0.004 μm $< D_p <$ 2.5 μm) and non-volatile particle fraction
2-channel OPC (Grimm SKY-OPC 1.129)	Total and non-volatile size distribution (0.25 μm $< D_p <$ 2.5 μm)
Thermo-denuder (250 °C) + CPC	Size distribution non-volatile/total Aitken mode (0.01 μm $< D_p <$ 2.5 μm)
3-λ-PSAP	Absorption coefficient at $\lambda = 467\,\text{nm}$, $\lambda = 530\,\text{nm}$ and $\lambda = 660\,\text{nm}$
SP2	Black carbon mass, single-particle coating thickness, mixing state
CCNC	Number concentration of cloud condensation nuclei as a function of supersaturation
Impactor sampler	Chemical composition and shape of fine mode particles
Aerosol in-situ instruments sampling at wing stations	
UHSAS-A	Aerosol size distributions (nominal size range 60 nm $< D_p <$ μm)
PCASP-100X	Dry state accumulation mode (nominal size range: 0.12 μm $< D_p <$ 3.5 μm)
FSSP-100	Ambient state accumulation + coarse mode (nominal size range: 0.1 μm $< D_p <$ 30 μm)
CAS-DPOL	Aerosol particle and cloud hydrometeor size distributions (nominal size range: 0.51 μm $< D_p <$ 50 μm), particle optical properties, particle shapes

Table 3.1: Instrumentation on board the Falcon research aircraft (SALTRACE-1) (continued)

Instrument	**Output**
Remote sensing instruments	
2-micrometer pulsed Doppler wind lidar	Horizontal wind vector (conical scan), vertical wind speed (nadir pointing), attenuated backscatter (conical scan and nadir pointing)
Meteorological data	
Standard instrumentation	Position, temperature, pressure, humidity, 3D wind
Dropsondes	Temperature, pressure, humidity, horizontal wind

Table 3.2: Instrumentation at Ragged Point Station, Barbados

Instrument	**Output**
Ground-based measurements by TROPOS Leipzig (SALTRACE-1)	
CPC	Total aerosol number concentration
APS, SMPS	Aerosol size distribution
CCNC	Number concentration of cloud condensation nuclei as a function of supersaturation
MAAP	Multi angle absorption photometer
SOAP	Spectral optical absorption photometer
Berner impactor	5-stage PM10 sampler
Aurora4000	Polar nephelometer
Digitel	High volume sampler
Ground-based measurements TU Darmstadt (SALTRACE-1)	
INC, Single-Particle Analysis	Ice nuclei sampling, hygroscopy, mineralogical analysis and chemistry from ground based samples (tower)
Ground-based measurements by the University of Miami (continuously)	
CIMEL sun photometer (AERONET)	Aerosol optical depth, aerosol optical properties

Table 3.3: Instrumentation at the CIMH campus, Bridgetown, Barbados

Instrument	**Output**
Ground-based measurements by TROPOS Leipzig (SALTRACE-1–3)	
BERTHA-Lidar	$\alpha(3\lambda)$, $\beta(3\lambda)$, $\Delta(3\lambda)$, HSRL at 532 nm
Dual-Polar sun photometer	AOD(8λ), DOLP
Radiosondes	Temperature, pressure, humidity, horizontal wind
Ground-based measurements by LMU Munich (SALTRACE-1)	
Polis-Lidar	$\alpha(2\lambda)$, $\beta(2\lambda)$, $\Delta(2\lambda)$
SSARA-P sun photometer	$\mathrm{AOD}_p(12\lambda)$, $\delta(\lambda)$

Chapter 4

Simulations of shallow cumulus convection

4.1 Overview

Before the results of the more complex large eddy simulations for the island–ocean setup will be shown, this chapter deals with the simulation of a cumulus-topped marine boundary layer. It will be demonstrated that ASAM (run in LES mode) is able to reproduce the main features of this boundary layer type, which primarily means the development of a well mixed layer and evolution and disintegration of shallow cumulus clouds under steady-state conditions over a couple of hours. If the model formulation and the case design are set up correctly, the ASAM results should be similar to those of other models.

In particular, the following case is constructed to be simple and yet close to reality. The latter can be achieved if the simulation setup is based on measurement data. In this case, the Barbados Oceanographic and Meteorological Experiment (BOMEX) from the late 1960s serves as data base (Holland and Rasmusson, 1973). First LES studies with these data have been conducted by Siebesma and Cuijpers (1995). The model setup designed in that work was the basis for an LES model inter-comparison study of shallow cumulus convection and turbulent dynamics for this type of boundary layer (Siebesma et al., 2003). A series of such inter-comparisons have been organized by the Global Water and Energy Experiment (GEWEX) Cloud System Studies (GCSS) Working Group 1 (WG1). They focus on statiform boundary layer clouds, especially the shallow cumulus regime. Other noteworthy GCSS cases are Dynamics and Chemistry of Marine Stratocumulus

(DYCOMS-II) (Stevens et al., 2005; Ackerman et al., 2009) and Rain in Cumulus over the Ocean (RICO) (Stevens and Seifert, 2008; vanZanten et al., 2011).

4.2 Model setup

The setup for the ASAM simulation of the BOMEX LES case is similar to the one described in Siebesma et al. (2003). The simulation domain is $6.4 \times 6.4 \times 3.2\,\mathrm{km}^3$. The horizontal grid spacing is varied with $\Delta x = \Delta y = 200\,\mathrm{m}$ (this case is called DX200 hereafter), $\Delta x = \Delta y = 100\,\mathrm{m}$ (DX100) and $\Delta x = \Delta y = 50\,\mathrm{m}$ (DX050). The vertical grid increment is $\Delta z = 50\,\mathrm{m}$ in all three cases. The DX200 simulation is chosen because the same grid spacing is used for the SALTRACE simulation setup (Section 5.1). The DX100 case has the same horizontal resolution as in the model inter-comparison study in Siebesma et al. (2003) so that these data sets can be well compared with each other. A further halving of the grid spacing should reveal effects of finer resolutions. It should be noted that $\Delta x = \Delta y \leq 50\,\mathrm{m}$ are standard for contemporary LES studies with the steady increase of computational power and also increased memory capacities.

The initial profiles of density potential temperature θ_ρ and the total water specific humidity $q_t = q_v + q_c + q_r$ basically consist of four layers: a mixing layer ($z < 500\,\mathrm{m}$), a conditionally unstable (cloud) layer ($500 < z < 1500\,\mathrm{m}$), an inversion layer ($1500 < z < 2000\,\mathrm{m}$) and the free troposphere ($z > 2000\,\mathrm{m}$). The initial state is cloudless, which leads to $q_t = q_v$. Time-invariant surface energy fluxes are applied with $Q_{\mathrm{sens}} = 8.8\,\mathrm{W\,m^{-2}}$ and $Q_{\mathrm{lat}} = 143\,\mathrm{W\,m^{-2}}$. The momentum flux is specified by $\langle \vec{v}' w' \rangle_s = -u_*^2 \frac{\vec{v}}{|\vec{v}|}$ with the friction velocity $u_* = 0.28\,\mathrm{m\,s^{-1}}$. Three large-scale forcing terms are applied to the model equations. They include a piecewise linear subsidence velocity profile with an absolute peak value of $-560\,\mathrm{m\,day^{-1}}$, radiative cooling of $-2\,\mathrm{K\,day^{-1}}$ and large-scale advection of dry air into the lower boundary layer of $-1\,\mathrm{g\,kg^{-1}\,day^{-1}}$:

$$w_{\mathrm{sub}} = \begin{cases} -4.33 \cdot 10^{-6}\,\mathrm{s^{-1}} z\,, & z \leq 1500\,\mathrm{m} \\ -0.0065 + 1.08 \cdot 10^{-5}\,\mathrm{s^{-1}} \cdot (z - 1500\,\mathrm{m})\,, & 1500\,\mathrm{m} < z \leq 2100\,\mathrm{m} \\ 0.0\,, & z > 2100\,\mathrm{m} \end{cases} \tag{4.1}$$

$$\frac{\mathrm{d}\theta}{\mathrm{d}t} = \begin{cases} -2.315 \cdot 10^{-5}\,\mathrm{K\,s^{-1}}\,, & z \leq 1500\,\mathrm{m} \\ -2.315 \cdot 10^{-5}\,\mathrm{K\,s^{-1}} & \\ \quad +2.315 \cdot 10^{-8}\,\mathrm{K\,s^{-1}\,m^{-1}} \cdot (z - 1500\,\mathrm{m})\,, & 1500\,\mathrm{m} < z \leq 2500\,\mathrm{m} \\ 0.0\,, & z > 2500\,\mathrm{m} \end{cases} \tag{4.2}$$

$$\frac{\mathrm{d}q_v}{\mathrm{d}t} = \begin{cases} -1.2 \cdot 10^{-8}\,\mathrm{s^{-1}}\,, & z \leq 300\,\mathrm{m} \\ -1.2 \cdot 10^{-8}\,\mathrm{s^{-1}} & \\ \quad +6 \cdot 10^{-11}\,\mathrm{s^{-1}\,m^{-1}} \cdot (z - 300\,\mathrm{m})\,, & 300\,\mathrm{m} < z \leq 500\,\mathrm{m} \\ 0.0\,, & z > 500\,\mathrm{m} \end{cases} \tag{4.3}$$

To break the symmetry of the initial conditions, random perturbations in the temperature and specific humidity field are applied, with amplitudes of 0.1 K and $0.025\,\mathrm{g\,kg^{-1}}$, respectively. A damping layer above $z = 2900\,\mathrm{m}$ is used to suppress gravity wave reflection at the model top boundary. More details on the used damping layer will be found in the SALTRACE simulation setup, Section 5.1. The latitude for this simulation is set to $\varphi = 15°$. Due to the sensitivity of the used advection and turbulence scheme on the simulation results (e.g., Heinze, 2013; Matheou et al., 2011; Stevens et al., 2005), it should be mentioned here that a third-order advection scheme and the standard Smagorinsky SGS model (with the Smagorinsky constant $C_s = 0.18$) are used for the BOMEX simulations.

4.3 Simulation results

To obtain information about the mean boundary layer structure and cloud properties, domain and time averages are calculated for different quantities. While the spatial average covers the whole horizontal extent of the simulation domain, a temporal average of 1 h is used for low-order statistics (i.e., scalars and velocity components) and 3 h appears to be necessary for reliable higher-order statistics (i.e., turbulent fluxes). The profiles that contribute to these time-averages are calculated every 30 s. Time-averaged values are not denoted separately (it is always pointed out if a temporal average is applied), a horizontally averaged value is marked by angle brackets and calculated as follows:

$$\langle \phi \rangle = \frac{1}{N_x N_y} \sum_{i=1}^{N_x} \sum_{j=1}^{N_y} \phi(i\Delta x, j\Delta y, z, t)\,, \tag{4.4}$$

where N_x and N_y are the number of grid points in $x-$ and y-direction, respectively. The deviation of this mean is denoted by $\phi' = \phi - \langle\phi\rangle$.

Figure 4.1 shows some mean vertical profiles for the three considered BOMEX simulations for different grid spacings. In all of these simulations, the initial atmospheric boundary layer structure (seen in the profiles of density potential temperature θ_ρ and specific humidity q_v) maintains throughout the model integration time. Above $z > 1300\,\mathrm{m}$ the air is moister than in the reference solutions, which can be explained by the different condensation/evaporation approach used in ASAM (cf. Eq. (2.50) in Section 2.7.2). The horizontal wind evolves with time due to surface roughness effects, especially in the subcloud layer. Clouds are present between $500\,\mathrm{m} < z < 2000\,\mathrm{m}$ altitude with a maximum cloud water content near the boundary layer top around $z \approx 700\,\mathrm{m}$. The release of latent heat leads to a moist-adiabatic increase of potential temperature, a stronger decrease of the mean specific humidity and slightly positive upward motions in this height range. A second maximum in the cloud water can be seen around $z \approx 1700\,\mathrm{m}$ with a strong decrease above due to the inversion layer, which inhibits further vertical cloud growth. This effect is also partly reproduced by other models and strongly depends on the microphysics and advection scheme.

The liquid water content seems to be to most variable quantity with respect to the grid spacing. However, since this quantity is averaged only over the last hour of the simulation time, the statistical significance is too low as it can be seen in the time series of the liquid water path (LWP) in Fig. 4.3. The LWP is defined as the vertically integrated liquid water content (i.e., the sum of cloud and rain water):

$$LWP = \int_{z_0}^{z_T} \rho(q_c + q_r)\,\mathrm{d}z. \tag{4.5}$$

with units in $\mathrm{kg\,m^{-2}}$. Furthermore, the relatively low cloud cover leads to a pronounced dependency of the LWP on only a few grid points with cloud water. Here and also in the remainder of this work, cloud cover is defined as the fraction of columns within the considered domain that contain at least one cell at any level with a specific cloud water content larger than $1 \times 10^{-5}\,\mathrm{kg\,kg^{-1}}$. Averaging the LWP and the cloud cover the last 3 hours of the simulation gives a more reliable image of the grid spacing sensitivity on the cloud properties. For the three considered cases, the mean LWP decreases slightly from $\langle\mathrm{LWP}\rangle \approx 6.5\,\mathrm{g\,m^{-2}}$ for the DX200 case to $\langle\mathrm{LWP}\rangle \approx 3.9\,\mathrm{g\,m^{-2}}$ for DX050. Clouds also organize differently with changing grid spacings, which is displayed in Fig. 4.2. In this figure, the LWP for the whole domain is shown at the end of the simulation time. It becomes

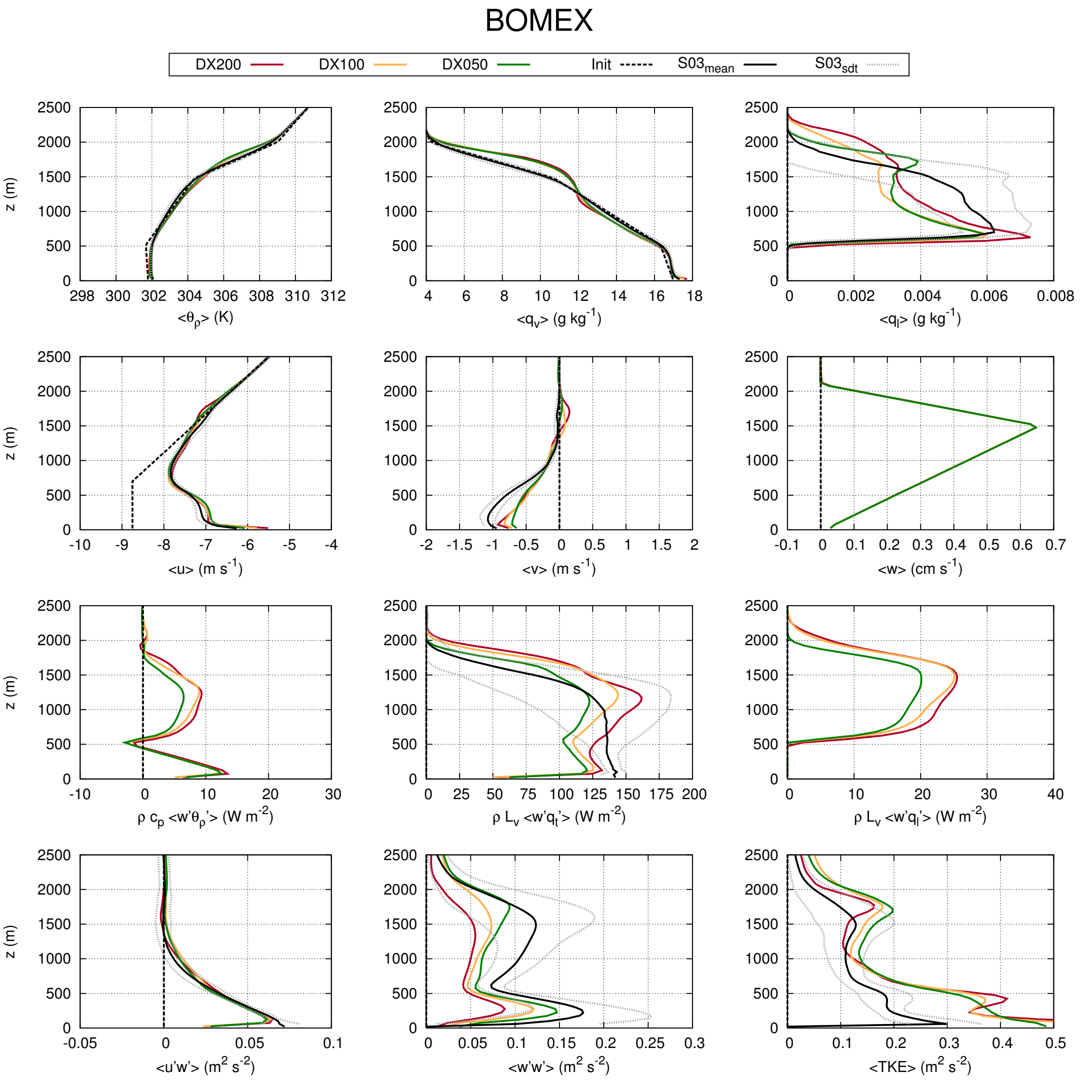

Figure 4.1: Mean vertical profiles for the BOMEX shallow cumulus case averaged over the last hour (first and second row) of density potential temperature $\langle \theta_\rho \rangle$, specific humidity $\langle q_v \rangle$, liquid water $\langle q_l \rangle$, zonal and meridional wind component $\langle u \rangle$ and $\langle v \rangle$ and vertical wind $\langle w \rangle$. Turbulent flux profiles averaged over the last 3 hours (third and forth row) of density potential temperature $\rho c_p \langle w' \theta'_\rho \rangle$, total water $\rho c_p \langle w' q'_t \rangle$, liquid water $\rho c_p \langle w' q'_l \rangle$, zonal wind $\langle u' w' \rangle$, vertical wind $\langle w' w' \rangle$ and turbulent kinetic energy $\langle \mathrm{TKE} \rangle$. Colored lines denote different grid spacings and the black dashed lines indicate the initial profiles. The solid black lines correspond to the mean profiles from the model inter-comparison study of Siebesma et al. (2003) (S03). Dotted gray lines denote the corresponding mean ± standard deviation (only visible if full datasets from all participating models were available).

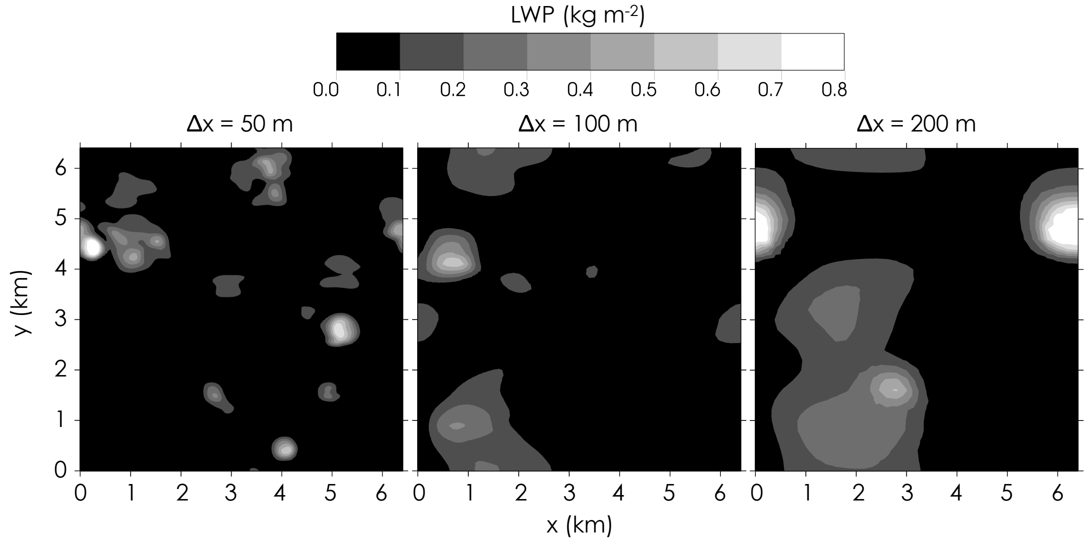

Figure 4.2: Instantaneous contours of LWP for the BOMEX shallow cumulus case at $t = 6\,\mathrm{h}$ simulation time for different horizontal grid spacings.

apparent that clouds are larger for coarser grid spacings but also that more small clouds are developing at finer grid spacings. The total cloud cover has similar values at the coarse grid spacings but increases at the highest spatial resolution with 9.7 % in the DX200 case to 9.4 % in DX100 and 11.1 % in DX050. This behavior is in agreement with studies of Matheou et al. (2011). They also found that grid convergence is achieved for grid spacings of 20 m for nonprecipitating cases. Higher cloud cover connected with finer resolutions are also reproduced in other studies, e.g., Riechelmann et al. (2012).

Higher-order moments in Fig. 4.1 show typical profiles for the marine boundary layer. The turbulent flux of θ_ρ decreases linearly in the subcloud layer. When condensation occurs, it increases again up to a maximum value of about $10\,\mathrm{W\,m^{-2}}$ around $z = 1200\,\mathrm{m}$. The total water flux $\langle w'q_t' \rangle$ shows a nearly similar behavior but at different magnitudes, where the maxima are dominated by the liquid water flux $\langle w'q_l' \rangle$. The resolved zonal component of the momentum flux $\langle u'w' \rangle$ does not show any dependence on the grid spacing. Values near the surface can be extrapolated to the parameterized surface stress. With increasing heights the momentum flux decreases monotonically down to zero in the middle of the cloud layer. Stronger variability with different grid spacings can be observed in the turbulent fluxes of vertical velocity component $\langle w'w' \rangle$ and the $\langle \mathrm{TKE} \rangle$ profiles. For the case of $\langle w'w' \rangle$, higher resolutions result in a better agreement with the reference profiles. The TKE profile shows a slight overestimation in the subcloud

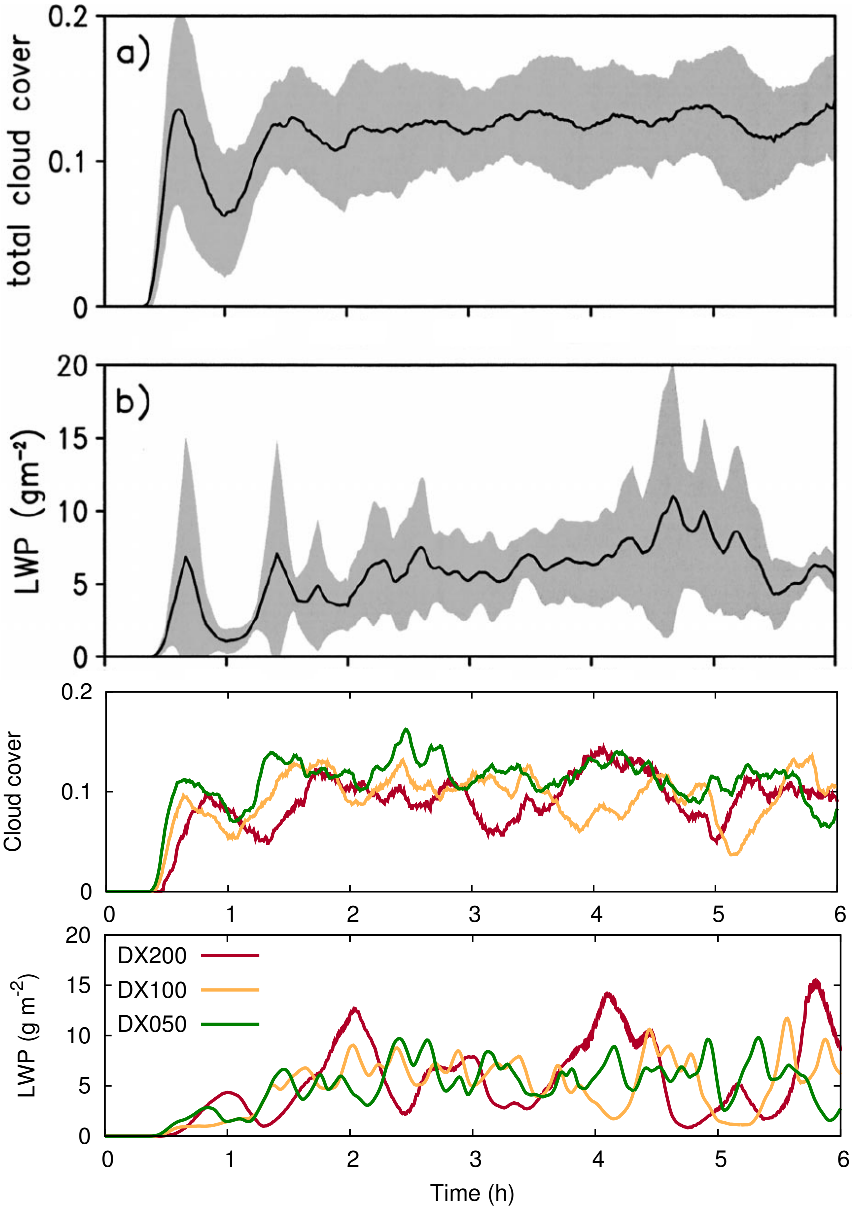

Figure 4.3: Time series of total cloud cover and liquid water path for the BOMEX shallow cumulus case. First and second panel: results from the intercomparison study of Siebesma et al. (2003) with mean values (solid line) and standard deviation (gray area). Third and fourth panel: results of ASAM simulations with different grid spacings.

.

layer, but the distinct double-peak profiles for both quantities can be reproduced by the ASAM simulations with the first one in the middle of the subcloud layer and the second one in the middle of the inversion layer. It should also be noted here that some aspects of numerics and physical parameterizations in ASAM differ more or less significantly from the participating models of the intercomparison study in Siebesma et al. (2003). All these factors have to be kept in mind when comparing and interpreting the results, as it is also mentioned in Dipankar et al. (2015), where the new new nonhydrostatic modeling system ICON (ICOsahedral Nonhydrostatic) is performed as LES model and compared against two other well-established standard LES codes. Overall, for the ASAM simulations, the higher-order moments and the temporal development of relevant parameters are in a good agreement with the inter-comparison study of Siebesma et al. (2003), which confirms that ASAM is suitable for performing LES of marine boundary layers as a prerequisite for the SALTRACE simulations following in the next section.

Chapter 5

Large eddy simulations of Barbados island effects

This chapter deals with results and discussion of the ASAM large eddy simulations. Simulation results are first and foremost presented for a shallow cumulus topped marine boundary layer. They are compared with results from a model intercomparison study to evidence that ASAM is capable to simulate reasonable boundary layer and cloud characteristics that are also reproduced by other models. After that, the setup for the SALTRACE simulations is presented, followed by the LES results and a comparison with measurement data. Parts of this analysis are already published in Jähn et al. (2015b).

5.1 The SALTRACE simulation setup

5.1.1 Domain and boundary conditions

To simulate atmospheric flow for the island–ocean system, the size of the model domain has to be appropriate dependent on the island size. The main criterion in this case is that a marine boundary layer has to develop at least several kilometers before it interferes with the island area. Also, the downwind area should approximately be twice of the island width so that resulting structures induced by the island can be properly represented. Since Barbados is a 24 km wide (west-east) and 34 km long (south-north) island, a model domain with a spatial extent of $102.4 \times 102.4\,\mathrm{km}^2$ is chosen. The island is located at the domain center. The model top is set to 5 km altitude.

Due to the presence of the island area, non-cyclic lateral boundary conditions have to be used. Within the finite volumes/differences discretization strategy adopted herein, a "zero-gradient" boundary condition is applied to all scalars and velocity components at each lateral boundary (north, east, south, west). This means that the boundary-perpendicular flux for these quantities is set to zero, which leads to a simple radiation condition near the outlets with minimal wave reflection. A pressure correction for sound waves is applied to each actual normal velocity component and not to the initial wind profile, which also suppresses artificial wave reflection near the inflow boundary. This setup ensures stability for the whole simulation time and works appropriately with the turbulence generation method, as shown at the end of this section.

For the top boundary, a free-slip condition is applied, i.e., the gradient of the tangential velocity component is zero. In order to prevent gravity wave reflection, an additional relaxation term is applied on the right-hand-side of the momentum equations:

$$\Phi^{n+1} = ... - \Delta t \cdot \rho K(d) \left(\Phi^n(d) - \Phi^0\right) , \tag{5.1}$$

with a damping function depending on the distance to the top boundary d:

$$K(d) = \begin{cases} d_f \sin^2\left(\frac{\pi}{2}\frac{d_w - d}{d_w}\right) & d < d_w \, , \\ 0 & d \geq d_w \, . \end{cases} \tag{5.2}$$

This damping layer is applied above $d_w = 4\,\text{km}$ model height (20 vertical layers) with a damping parameter $d_f = 1 \times 10^{-3}$.

Surface boundary conditions are represented by a momentum flux parameterization based on the Monin-Obhukov similarity theory (Monin and Obukhov, 1954):

$$\tau_{zx} = -\rho C_\mathrm{m} |\vec{v_h}| u \, , \tag{5.3}$$

$$\tau_{zy} = -\rho C_\mathrm{m} |\vec{v_h}| v \, . \tag{5.4}$$

C_m is the drag coefficient for momentum, which is defined as follows:

$$C_\mathrm{m} = \frac{k_K^2}{\Psi_\mathrm{M}^2} \, , \tag{5.5}$$

with

$$\Psi_\mathrm{M} = \ln\left(\frac{z + z_0}{z_0}\right) - \phi_\mathrm{m}\left(\frac{z}{L}\right) \, , \tag{5.6}$$

and ϕ_m representing the integrated similarity function. L stands for the Obukhov length and k_K is the von-Kármán-constant.

The topographic data is obtained from the Consortium for Spatial Information (CGIAR-CSI) Shuttle Radar Topography Mission (SRTM) dataset (`http://srtm.csi.cgiar.org`) at 200 m resolution. A simple smoothing algorithm is applied to guarantee a proper grid pre-processing. In the smoothed data set, the maximum elevation is lowered by about 15 m compared to the raw topography data, which is an acceptable level. It is important to note that if high-resolution simulations are performed, the topographical data set also has to be adequately resolved, e.g., as shown in Nunalee et al. (2015). If the resolution of these data is too coarse, the uncertainties in resolved dynamics might affect the simulation results in a negative manner.

Table 5.1 summarizes the model configuration for the Barbados large eddy simulations performed in Section 5.2.

Table 5.1: LES model configuration for the simulations performed in Section 5.2.

Model parameter	Value / description
Domain	$102.4 \times 102.4 \times 5\,\mathrm{km}^3$
Grid cells	512 x 512 x 100
Time step	4 s
Horizontal grid spacing	200 m
Vertical grid spacing	50 m
Start time (LT)	02:00
End time (LT)	22:00
Topography data	SRTM, 200 m resolution
Turbulence scheme	Standard Smagorinsky SGS model
Cloud microphysics	2-moment scheme (no ice phase) by Seifert and Beheng (2006)
Wind direction	East (90°)
Lateral BC	Zero gradient
Surface BC	Monin-Obhukov
Top BC	Free-slip
Damping layer	For $z \geq 4.0\,\mathrm{km}$

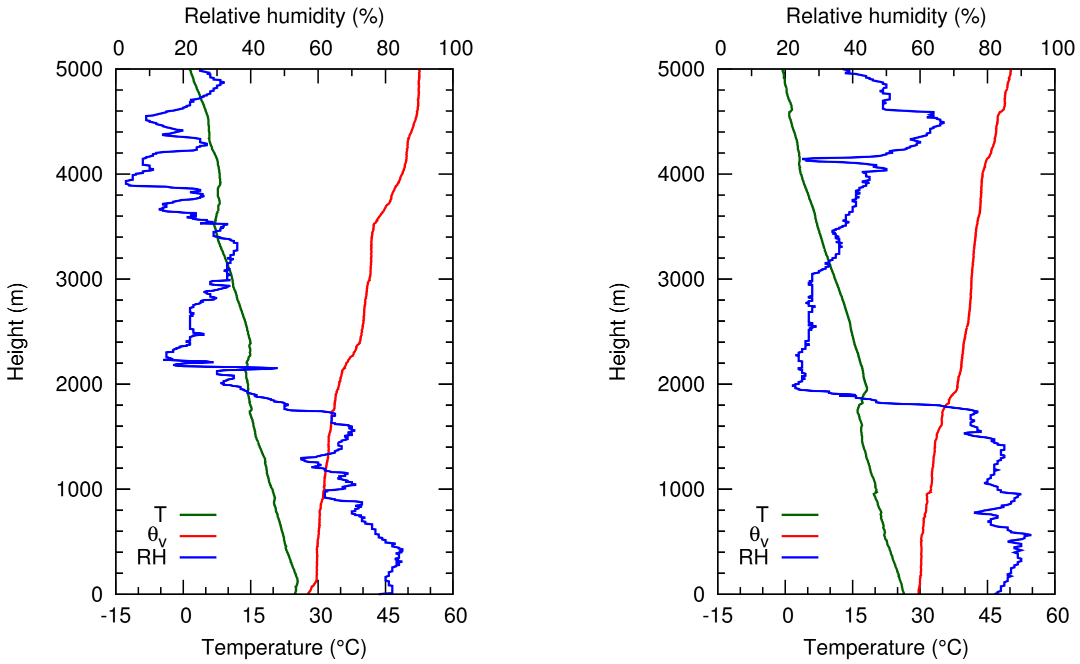

Figure 5.1: Nighttime radiosonde soundings on 22 June 2013 (left) and 27 June 2013 (right).

5.1.2 Initial data

The two cases examined (22 June and 27 June 2013) mainly differ in their atmospheric state and geostrophic forcing. Measured nighttime radiosonde profiles of temperature and humidity are directly used for model initialization (Fig. 5.1), which reduces the complexity of the simulations due to the absence of horizontal inhomogeneities and a time-varying background state. There are two reasons behind the choice of using single profiles instead of averaging multiple profiles. Firstly, a single initial profile is better for comparing the LES results with Doppler wind lidar data (cf. Section 5.4), which are obtained for a few selected cases during SALTRACE. Secondly, trade-wind inversions are only poorly represented when the soundings are averaged over many cases. This becomes apparent when considering the sharply defined inversion at the 27 June case, which is shown later on. Air density and pressure profiles are obtained by vertical integration with respect to hydrostatic equilibrium. Some simplifications are assumed for the geostrophic forcing. The wind direction is exclusively east (i.e., $d = 90°$ and $v_g = 0$), which is also for simplicity and to make it easier to define upwind and downwind regimes later on.

The vertical wind profiles are expressed as piecewise linear functions for both cases, respectively. For the 22 June case, the geostrophic wind at first linearly decreases above $z = 1600\,\mathrm{m}$ altitude and then increases again above $z = 3000\,\mathrm{m}$:

$$u_{g,1} = \begin{cases} -10.0\,\mathrm{m\,s^{-1}}\,\frac{\log(z/z_0)}{\log(700\,\mathrm{m}/z_0)}\,, & z \leq 0.7\,\mathrm{km} \\ -10.0\,\mathrm{m\,s^{-1}}\,, & z \leq 1.6\,\mathrm{km} \\ -10.0\,\mathrm{m\,s^{-1}} + 4.29\cdot10^{-3}\,\mathrm{s^{-1}}\cdot(z-3000\,\mathrm{m})\,, & 1.6\,\mathrm{km} < z \leq 3.0\,\mathrm{km} \\ -4.0\,\mathrm{m\,s^{-1}} - 2.0\cdot10^{-3}\,\mathrm{s^{-1}}\cdot(z-5000\,\mathrm{m})\,, & 3.0\,\mathrm{km} < z \leq 5.0\,\mathrm{km} \end{cases} \tag{5.7}$$

with a roughness length $z_0 = 0.01\,\mathrm{m}$. A turn in wind direction to southwest is observed within the layer where the wind speed decreases. However, this is not captured by the LES due to the simplifications and assumptions mentioned above. Therefore, the effect of wind directional shear might be underestimated in the model for this case. The change in wind direction (±15°) is rather small at other altitudes so that the LES input profile can be considered as a good approximation. For the 27 June case, the geostrophic wind linearly decreases above $z = 3000\,\mathrm{m}$ altitude:

$$u_{g,2} = \begin{cases} -11.5\,\mathrm{m\,s^{-1}}\,\frac{\log(z/z_0)}{\log(700\,\mathrm{m}/z_0)}\,, & z \leq 0.7\,\mathrm{km} \\ -11.5\,\mathrm{m\,s^{-1}}\,, & z \leq 3\,\mathrm{km} \\ -11.5\,\mathrm{m\,s^{-1}} + 5.25\cdot10^{-3}\,\mathrm{s^{-1}}\cdot(z-3000\,\mathrm{m})\,, & z > 3\,\mathrm{km} \end{cases} \tag{5.8}$$

In this profile there is no distinct change in wind direction. Figure 5.2 visualizes the measured (green lines) and parameterized (red lines) velocity profiles for both cases. The LES background wind profiles are parameterized to closely match the soundings. Within the boundary layer, the LES profile should be near the nighttime measurements (dark green line) because this is mainly a representation of the marine boundary layer. For the free troposphere ($\approx$ above 1000 m altitude), the LES profile should roughly be a mean of all three soundings, since no large-scale advection term is applied on the wind components during the simulation time.

Table 5.2 shows a comparison of the two simulated cases with respect to mean flow properties, trade inversion strength, moisture load (all derived from radiosonde profiles), CCN concentrations (obtained by ground-based measurements at Ragged Point station) and the location of the Saharan dust layer (estimated from BERTHA lidar measurements at CIMH). The differences in the geostrophic forcing are already discussed. Regarding the atmospheric stability, there is a much stronger trade inversion for the 27 June case with a local virtual potential temperature gradient

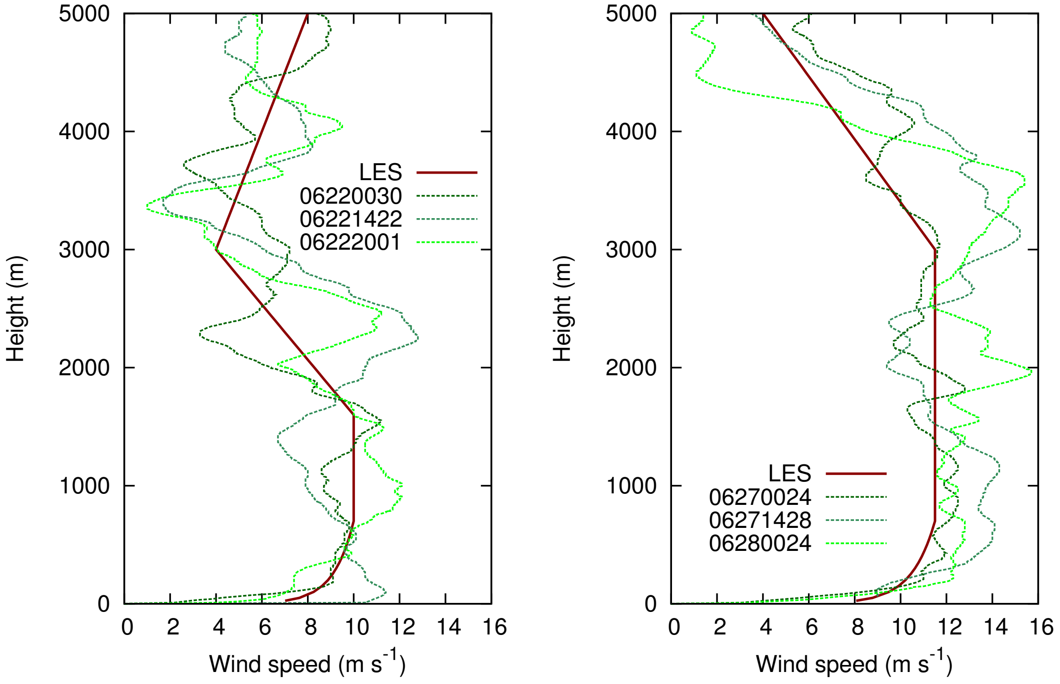

Figure 5.2: Parameterized (LES) and measured wind profiles from radiosondes on 22 June 2013 (left) and 27 June 2013 (right). Names indicate date and time in UTC.

Table 5.2: Parameter values of the cases to be examined: 22 June and 27 June 2013.

Parameter	Unit	22 June 2013	27 June 2013
Maximum geostrophic wind $\|u_g\|$	$\mathrm{m\,s^{-1}}$	10.0	11.5
Top altitude of trade-wind inversion $z_{\mathrm{inv,t}}$	m	2200	2000
Bottom altitude of trade-wind inversion $z_{\mathrm{inv,b}}$	m	1600	1800
Inversion strength $\mathrm{d}\theta_v/\mathrm{d}z$	$\mathrm{K\,km^{-1}}$	5.67	13.89
Surface pressure p_0	hPa	1014.2	1013.9
Integrated water vapor content up to up to $z = 2\,\mathrm{km}$	$\mathrm{kg\,m\,kg^{-1}}$	22.14	26.16
CCN concentration at 1% supersaturation $N_{\mathrm{CCN,1\%}}$	$\mathrm{cm^{-3}}$	300	300
Top altitude of Saharan dust layer	m	2800	2900
Bottom altitude of Saharan dust layer	m	1800	1700

of 14 $\mathrm{K\,km^{-1}}$. As mentioned in the introduction, the trade inversion controls the amount of precipitation and the lifetime of cloud streets. Furthermore, there is a 18 % stronger moisture load for the 27 June case, where a faster cloud development is expected. Due to the vertical and temporal variability of the CCN number concentrations, a mean value of 300 $\mathrm{cm^{-3}}$ has been chosen for both cases, which is a typical magnitude for days with a moderate dust load, where aerosol optical depths between 0.2 and 0.4 are observed.

5.1.3 Forcings

Surface sensible and latent heat fluxes over the island and the ocean are obtained by separate 1D simulations with full model physics. The parameterizations there include the radiation scheme (Fu and Liou, 1993) as well as land-use and soil models. The soil class 'loam' was chosen to represent the average island soil type. Hydraulic and thermal parameters of this soil type can be found in Doms et al. (2011) and Jähn et al. (2015a). For land surface parameterization, 'shrubland' appears to be a good compromise between coastal beach areas and forest in the

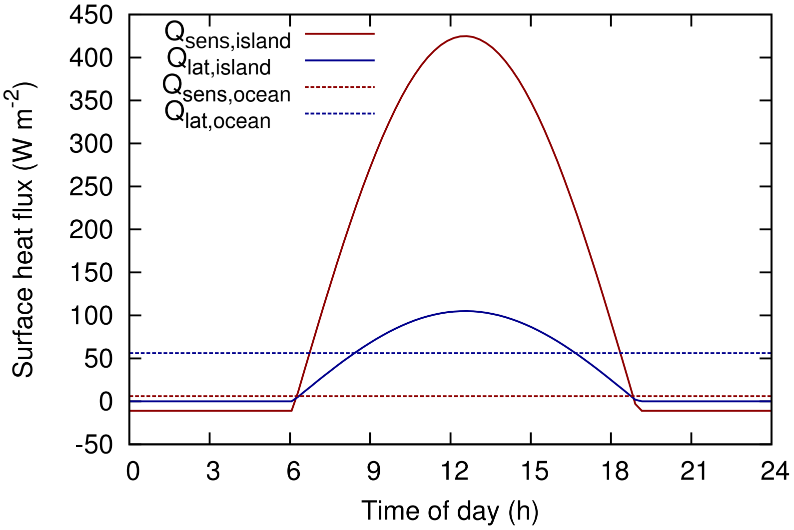

Figure 5.3: Parameterized diurnal variation of sensible and latent heat fluxes dover island and ocean areas.

island interior. The roughness length of this land type is $z_{\mathrm{R,island}} = 0.2\,\mathrm{m}$, whereas the ocean roughness length is set to $z_{\mathrm{R,ocean}} = 0.01\,\mathrm{m}$. The usage of direct (compared to interactive) fluxes reduces computational costs for the LES runs and makes it easier to potentially reproduce these simulations by other models, especially due to a large number of existing radiation and land-use models. Figure 5.3 shows the diurnal variation of sensible and latent heat fluxes over the island area. The maximum sensible heat flux over the island is $Q_{\mathrm{sens_{max},island}} = 425\ \mathrm{W\,m^{-2}}$ and the corresponding maximum latent heat flux is $Q_{\mathrm{lat_{max},island}} = 105\ \mathrm{W\,m^{-2}}$. Surface heat fluxes over the ocean are constant during the whole simulation time with $Q_{\mathrm{sens,ocean}} = 6\ \mathrm{W\,m^{-2}}$ and $Q_{\mathrm{lat,ocean}} = 56\ \mathrm{W\,m^{-2}}$. The latent heat flux over the ocean is comparably lower than in other studies (e.g., Siebesma et al., 2003; vanZanten et al., 2011), however it was directly obtained from simulations using the bulk aerodynamic formula in the form of Eq. (2.64c) and the measured humidity profile. Sunrise is at 05:36 LT and sunset is at 18:29 LT, whereby the fluxes are shifted by 30 minutes to represent the delay due the fact that the soil has to be heated first before energy exchange with the lower atmosphere can take place.

5.1.4 Turbulence generation – the cell perturbation method

LES modeling technique has the advantage of allowing explicit resolution of turbulent production and part of the inertial range scales, being today the most accurate and computationally feasible modeling approach in the context of high Reynolds number flows. LES results are strongly dependent on boundary conditions, therefore requiring specification of realistic inflow turbulence characteristics that propagate through the domain into the area of interest. In order to ensure that the incoming boundary layer characteristics at Barbados correspond to fully-developed turbulence consistent with the imposed marine boundary layer forcing, the cell perturbation method recently proposed by Muñoz-Esparza et al. (2014) is used. The cell perturbation method uses a novel stochastic approach based upon finite amplitude perturbations of the potential temperature field applied within a region near the inflow boundaries of the LES domain. This method has demonstrated superior performance when compared to a state-of-the-art synthetic turbulence generators and is computationally inexpensive (Muñoz-Esparza et al., 2015).

Previous studies where the cell perturbation method was developed and validated dealt with transitions from smooth mesoscale flow to nested LES (Muñoz-Esparza et al., 2014, 2015). In these idealized cases, boundary conditions at the LES domain boundaries were imposed from the mesoscale model instantaneous solution (Dirichlet boundary conditions), in which moisture effects were not considered. Herein, the application of the cell perturbation method is further extended to turbulence inflow generation for cloud modeling including terrain effects. As explained in earlier sections, zero-gradient open radiative lateral boundary conditions need to be used in order to minimize wave reflections at the boundaries that do develop in fully-compressible codes like ASAM-LES model when the domain includes terrain features. In order to test the best configuration for the cell perturbation method in this particular context, a series of calculations is performed where only the upstream region of the Barbados island is considered (i.e., incoming marine boundary layer). The reduced subset of the domain consists of a 51.2 km × 51.2 km area in the horizontal, with the same vertical extent (5 km) and large-scale forcings like in the BOMEX case described in Section 5.1.3 for the 22 June 2013 case study. To represent the marine boundary layer conditions that are going to be imposed through the entire simulation period, constant sensible and latent heat fluxes of $Q_{\mathrm{sens,ocean}} = 6\ \mathrm{W\,m^{-2}}$ and $Q_{\mathrm{lat,ocean}} = 56\,\mathrm{W\,m^{-2}}$ are used (see Fig. 5.3).

The sensitivity of the generated turbulence by the cell perturbation method to the

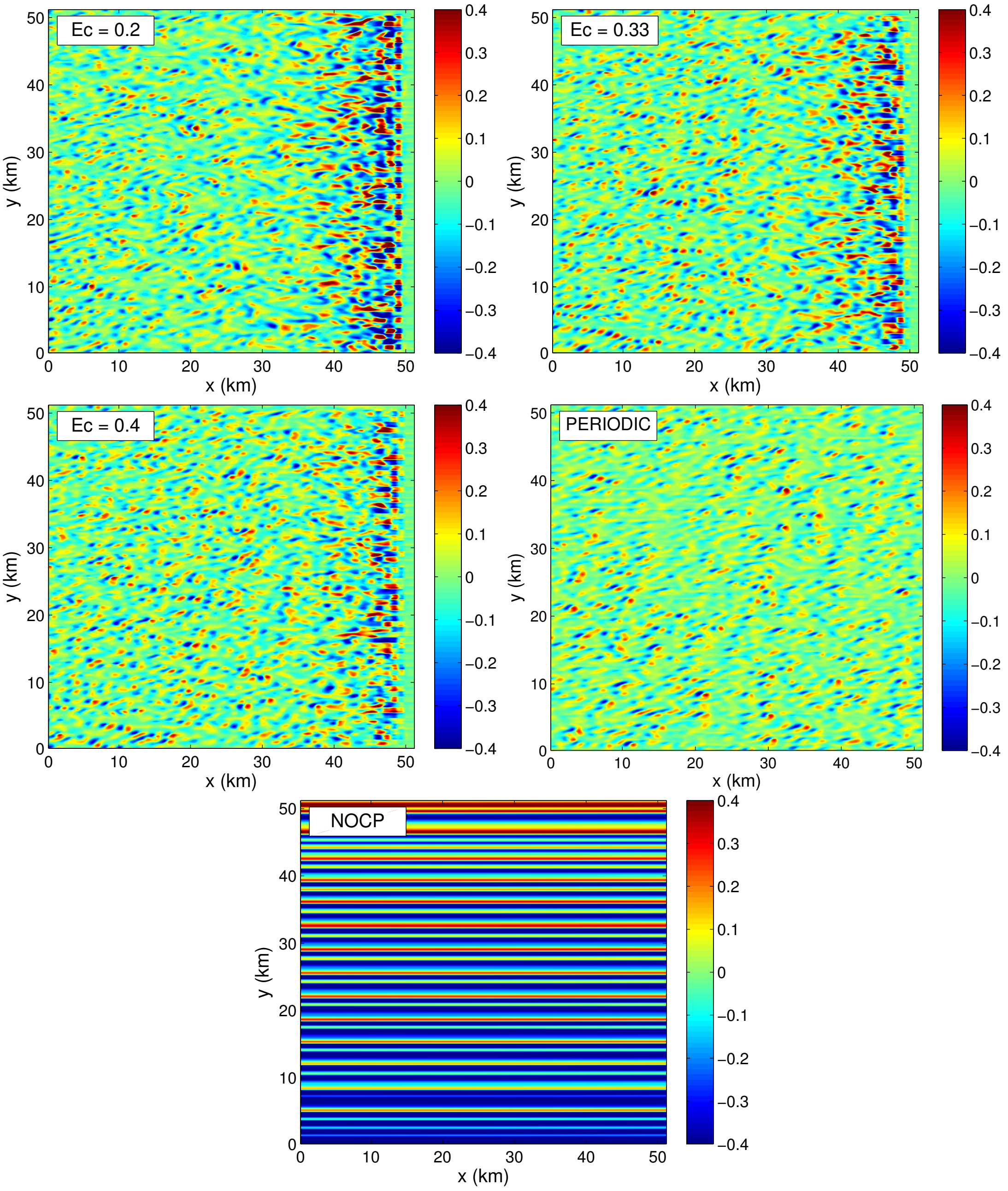

Figure 5.4: Instantaneous contours of vertical velocity at $z = z_i/2 = 375\,\mathrm{m}$ or different perturbation Eckert numbers, $Ec = 0.2, 0.33, 0.4$, the periodic reference solution and the no perturbation case (NOCP, $Ec = \infty$).

optimum perturbation Eckert number, $Ec = U_g^2/c_p\tilde{\theta}_{pm} = 0.2$ is explored, where U_g is the mean geostrophic wind and $\tilde{\theta}_{pm}$ is the maximum potential temperature perturbation. The perturbations are random and uniformly distributed in the interval $\left[-\tilde{\theta}_{pm}, +\tilde{\theta}_{pm}\right]$. Three square cells adjacent to the east boundary are used, which were found to provide the fastest transition to a fully-developed turbulent state (Muñoz-Esparza et al., 2015). The cell size is set to 4×4 grid points, to ensure the cell wavelength falls within the inertial range of three-dimensional turbulence. The perturbation time scale, t_p, was obtained from $\Gamma = t_p U_1 (4\Delta x)^{-1} = 1$ (Muñoz-Esparza et al., 2015) with U_1 being the horizontal wind speed in the first vertical layer, resulting in a frequency to seed instantaneous perturbations of $t_p = 145\,\mathrm{s}$. Figure 5.4 shows instantaneous contours of vertical velocity at $z = z_i/2 = 375\,\mathrm{m}$ for different perturbation Eckert numbers, $Ec = 0.2$, 0.33, 0.4, the periodic reference simulation and for the non-perturbation case (NOCP, $Ec = \infty$). The cell perturbation method for the three Ec numbers considerably accelerates the formation of three-dimensional turbulent structures that agree with the ones obtained in the reference simulation using periodic lateral boundary conditions. As the perturbation Eckert number increases (maximum perturbation amplitude decreases), the strength of the vertical velocities induced by the temperature perturbations is progressively reduced, and the onset of forcing-consistent turbulence seems to qualitatively occur at earlier distances from the inflow boundary. In contrast, the NOCP case exhibits the formation of coherent streamwise bands, with homogeneous amplitude and spacing across the entire streamwise extension of the domain. This pattern differs from the observed features in the convective boundary layer case analyzed by Muñoz-Esparza et al. (2014), where buoyancy-induced turbulence developed progressively as the flow was advected away from the inflow boundary. This effect can be attributed to the use of zero gradient lateral boundary conditions, where there is no "clean" flow imposed at the boundaries and the convection from the imposed heat flux at the surface does not have a predominant location to initiate and rather develops everywhere in the domain and at the same rate.

In order to have a better understanding of the turbulence initiation and development processes, the energy spectrum evolution in the streamwise direction for the three velocity components is presented in Fig. 5.5. The cell perturbation method instigates a rapid development of the upper-wavenumber portion of the energy spectrum for the u and v components. The larger scales (lower wavenumbers) require longer distances to be established due to large buoyant plumes having to emerge from the surface and populate across the entire extent of the boundary layer.

This flow development pattern is consistent with the findings from Muñoz-Esparza et al. (2014) for convective conditions. In contrast, the energy spectrum for the vertical velocity reveals a rapid growth of turbulent energy that reaches levels 10 times greater than the periodic quasi-equilibrium solution (dashed black line), and that progressively dissipate as the flow transitions through the domain. This behavior is attributed to the cell size, $4\Delta x$, which for the resolution employed in this study may fall in the vicinity of the limit of the inertial range. Smaller cell sizes were not considered due to the energy dissipation at high wavenumbers present in finite differences/volumes discretizations. There, an interaction with fully-resolved scales and an instigation of an accelerated transition to a developed turbulence state would not have taken place. In addition, the use of zero-gradient lateral boundary conditions helps to maintain the signature of the perturbations more than in the case of Dirichlet boundary conditions, hence contributing to strengthen the periodically seeded perturbations. It is worth noting that the effective model resolution can be estimated by the wavelength in the inertial range where the the code starts to deviate from the theoretical –5/3 decay. From this spectral analysis, it appears that the model starts to tail off at about $6\Delta x$, which is in the same order as in the WRF code (Muñoz-Esparza et al., 2014).

By increasing the perturbation Eckert number from 0.2 to 0.4 (first row vs. third row in Fig. 5.5), the energy overestimation is damped, and results after a fetch of 40 km for $Ec = 0.4$ are in close agreement with the periodic simulation used as reference and have reached quasi-equilibrium converged statistics. The $Ec = 0.2$ case results in energy deficit at wavenumbers close to the integral length scale, and also at the highest wavenumbers for the w component. When the cell perturbation method is not used (NOCP panels, bottom row in Fig. 5.5), dramatic energy deficits are found, together with an unrealistic spiky energy distribution in which the expected energy production and cascade processes are not present.

Finally, the vertical distribution of relevant boundary layer quantities at a downstream distance of 40 km from the east boundary (i.e., $x = 11.2$ km) is examined. Vertical profiles (Fig. 5.6) show the best agreement with the periodic simulation for the $Ec = 0.4$ and 0.33 cases, in particular for the turbulent kinetic energy levels and boundary layer structure. Momentum flux profiles exhibit slightly larger values in the first 250 m, due to the differences in the horizontal wind speed distribution near the surface. However, the boundary layer structure is similar, with the differences being related to distinct quasi-equilibrium solutions for the periodic and the open boundary condition simulations. Similar conclusions are found for

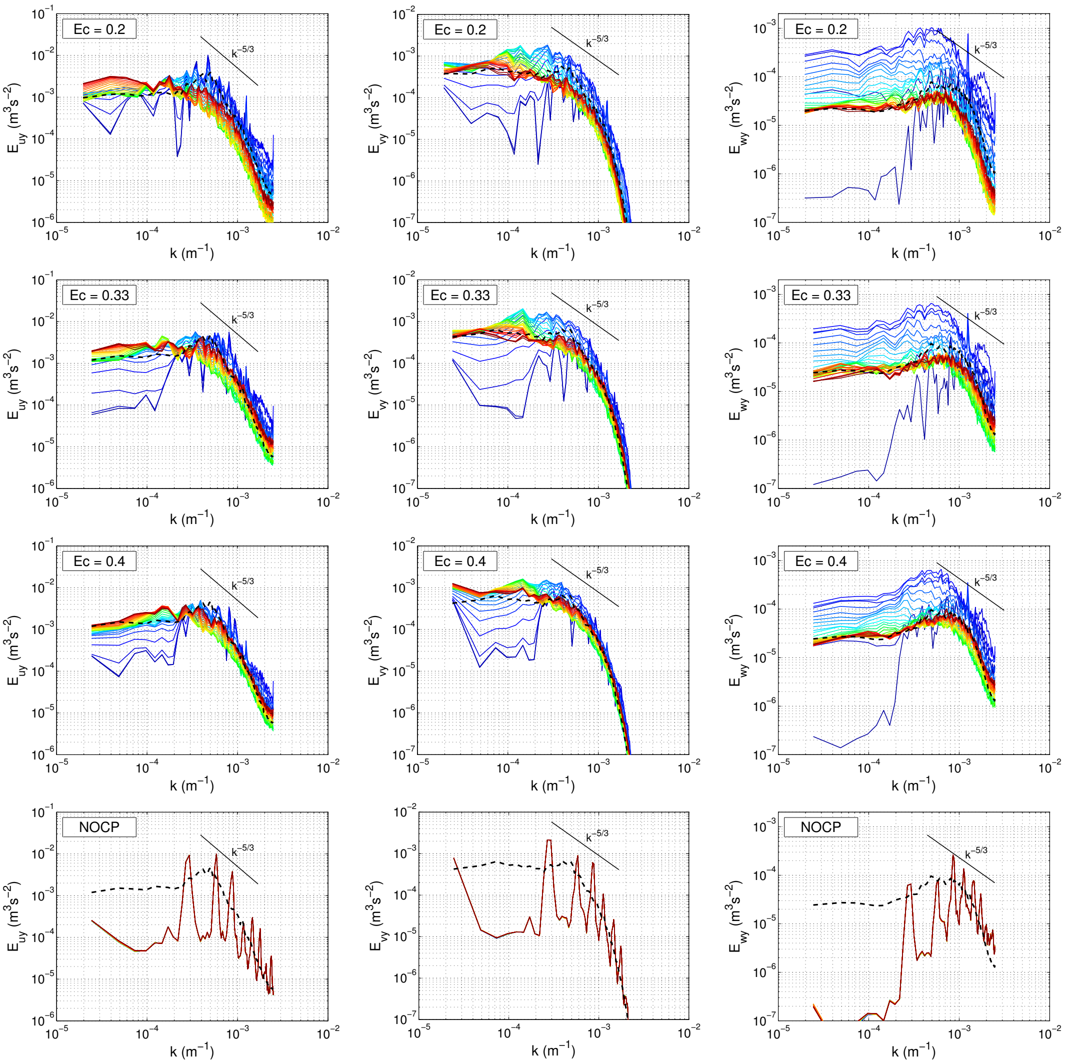

Figure 5.5: Spatial evolution of time-averaged energy spectra of *u*- (left), *v*- (middle) and *w*-component (right) in the *y*-direction at $z/z_i = 0.5$ for three perturbation Eckert numbers and the NOCP case. Color lines indicate distance from the east lateral boundary in steps of 0.8 km, 51.2:-0.8:1.6 km, from blue to red. The dashed black line corresponds to the reference spectrum from the periodic computation, additionally averaged in the streamwise direction.

the sensible and latent heat fluxes. The cell perturbation method was originally developed and tested in the context of dry boundary layers (Muñoz-Esparza et al., 2014, 2015). It is worth emphasizing that it is demonstrated for the first time, as it can be seen from the latent heat flux profile, that the cell perturbation method has the ability to develop turbulent moisture features that are in agreement with the imposed forcing. The $Ec = 0.2$ case fails to produce a boundary layer structure that is similar to the reference periodic case, with excessive mixing attributed to an enhanced effect of the perturbations for the reasons before mentioned. Also, the NOCP case does not provide realistic turbulent boundary layer features corresponding to a strongly under-developed turbulent state. Therefore, the $Ec = 0.4$ setup is selected as the inflow to be used for the island simulations presented in the remaining of the manuscript since it produces the most rapid development and stabilization of forcing-consistent turbulence. This is further evidenced by taking the downwind evolution of the TKE into account (Fig. 5.7), where the non-dimensional integrated TKE is defined by

$$\mathrm{TKE}_{\mathrm{int}} = \frac{1}{L_x L_y L_z u_*^2} \int_0^{L_x} \int_0^{L_y} \int_0^{z_i} \mathrm{TKE}(x, y, z)\, \mathrm{d}x\, \mathrm{d}y\, \mathrm{d}z \qquad (5.9)$$

It can be observed how the $Ec = 0.2$ results in an overshoot of TKE that requires longer fetches to stabilize and has a rate of growth slower than the other two perturbation Ec numbers. This reinforces the choice of a different Ec number than 0.2. For the island cases discussed in the next section, a domain with horizontal extent of $102.4 \times 102.4\,\mathrm{km}^2$ is used, which leaves sufficient fetch for the marine boundary layer to develop prior to start interacting with the topography of Barbados and its local stability effects.

5.2 Results of the SALTRACE simulations

To investigate the effects of the Barbados island area on boundary layer properties, cloud generation and vertical mixing of aerosols, two subdomains that are defined to be representative for the upwind and downwind area, respectively. Figure 5.8 shows the position of these two subdomains. They both cover a base area of $10 \times 20\,\mathrm{km}^2$ and are used for averaging of vertical profiles and time series of the relevant quantities. The upwind domain east of Barbados (representing the marine boundary layer) is approximately 15 km away from the eastern boundary to avoid contamination from the inflow boundaries where turbulence has to be generated

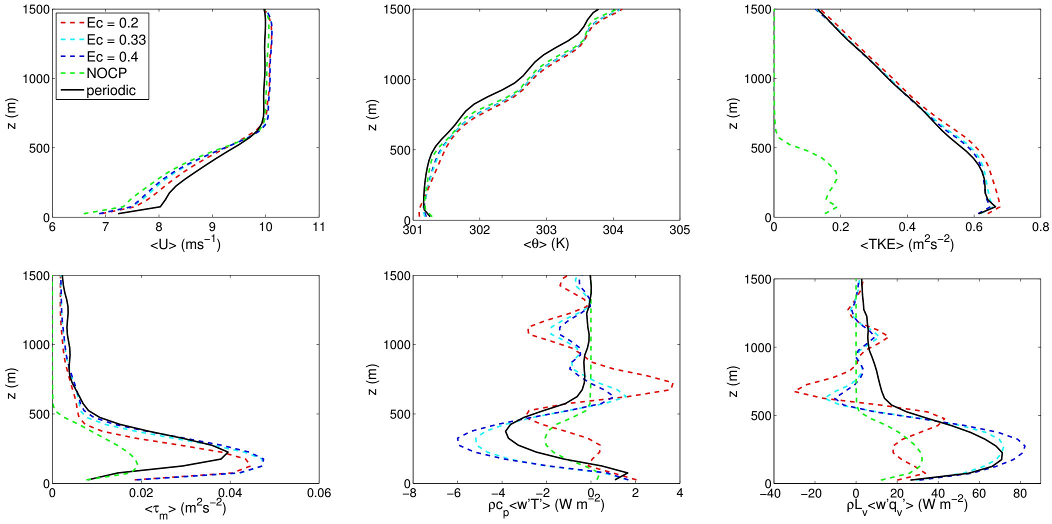

Figure 5.6: Vertical profiles of horizontal wind speed $\langle U \rangle$ (top left panel), potential temperature $\langle \theta \rangle$ (top middle), turbulent kinetic energy $\langle \mathrm{TKE} \rangle$ (top right), momentum flux $\langle \tau_m \rangle$ (bottom left), sensible heat flux $\rho_0 c_{pd} \langle w'T' \rangle$ (bottom middle) and latent heat flux $\rho_0 L_0 \langle w' q'_v \rangle$ (bottom right) at a downstream distance of 40 km from the east boundary for different Ec numbers and the NOCP case (averaged along the y-direction and in time). The solid black line corresponds to the reference profile from the periodic computation, additionally averaged in the streamwise direction. The profiles are valid for the 22 June 2013 case.

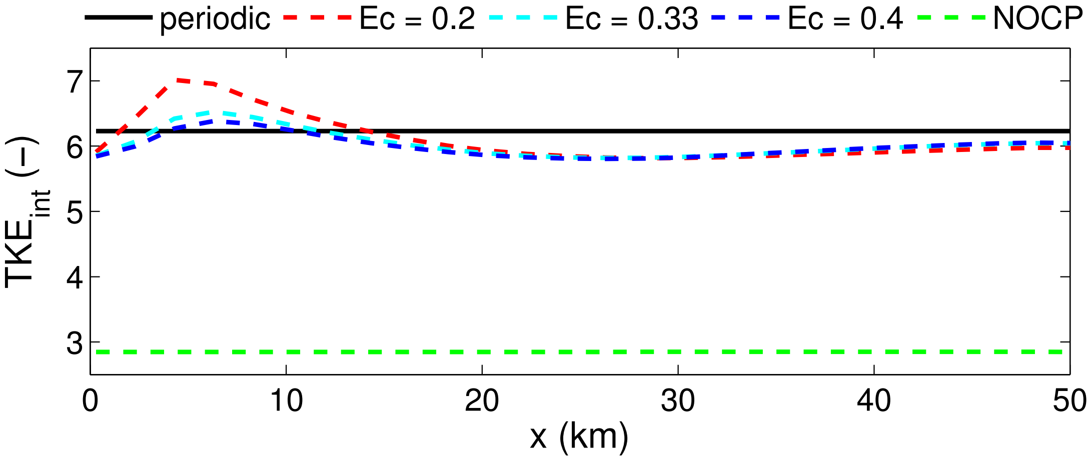

Figure 5.7: Non-dimensional integrated turbulent kinetic energy $\mathrm{TKE}_{\mathrm{int}}$ as a function of the distance from the inflow boundary.

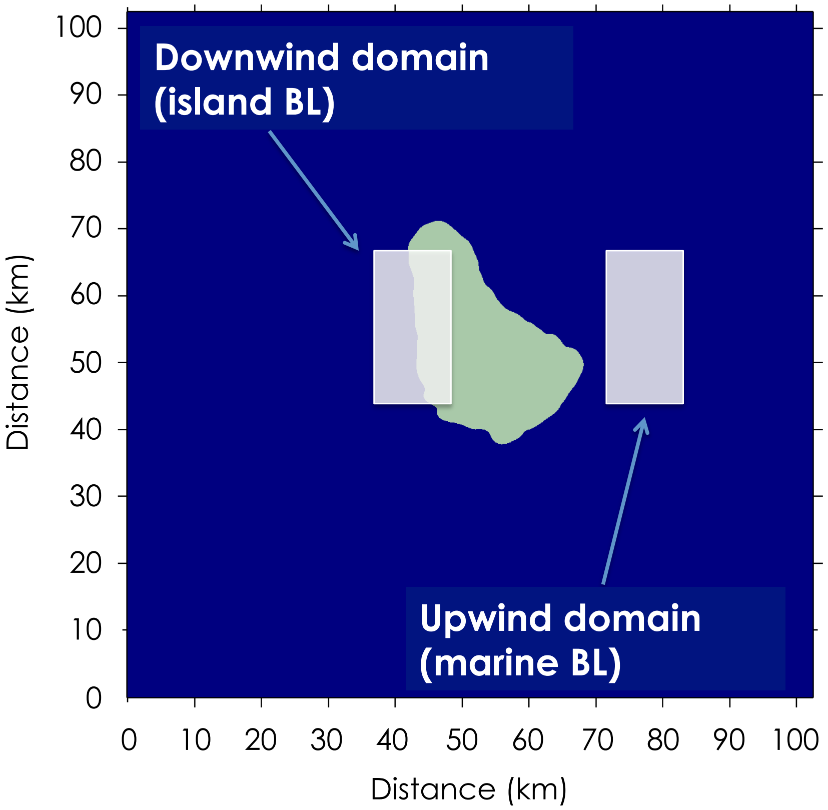

Figure 5.8: Definitions of subdomains for spatial averaging to cover different boundary layer characteristics: upwind marine regime east of Barbados (right) and downwind island regime over the west coast area (left).

Table 5.3: Parameter choices for the performed sensitivity simulations.

Simulation name	Date	Δx, Δy (m)	Δz (m)	$\tilde{Q}_{\mathrm{sens}}$ ($\mathrm{W\,m^{-2}}$)	Turbulent inflow	Orography
REF	2013-06-22	200	50	436	yes	yes
INV	2013-06-27	200	50	436	yes	yes
NOCP	2013-06-22	200	50	436	no	yes
DX400	2013-06-22	400	100	436	no	yes
FLAT	2013-06-22	200	50	436	yes	no
FLUX	2013-06-22	200	50	218	yes	yes

first. Looking into the model data, it becomes apparent that at least half of the island area has to be overflown until a well-mixed convective layer can fully develop. For that reason, the downwind subdomain is located between $35\,\mathrm{km} < x < 45\,\mathrm{km}$ and thus covers the west coast island area and the marine offshore area in equal parts. The following analysis mainly consists of comparisons between these two regimes to investigate island effects on various parameters.

5.2.1 Overview of the performed simulations

The simulation ensemble that is going to be analyzed consists of altogether six cases. The first two cases differ in their initial atmospheric state and dynamical forcing. They were already introduced in Section 5.1.2 and are further denoted as REF case (22 June 2013) and INV case (27 June 2013) because the first one is taken as basis for several sensitivity tests and the latter one is mainly characterized by its strong trade inversion between $1800\,\mathrm{m} < z < 2000\,\mathrm{m}$ asl. For the first sensitivity case (NOCP), the cell perturbation method described in Section 5.1.4 is disabled so that the upwind flow is strongly underdeveloped. With this setup, the effect of having a realistic turbulent boundary layer around the island rather than idealized constant winds is investigated. In the next sensitivity case (DX400), the grid resolution is halved from 200 m to 400 m horizontally and from 50 m to 100 m vertically to point out the deficiencies in the use of coarser resolution without appropriate resolved turbulence and gray zone modeling (Wyngaard, 2004) for particular aspects of interest in boundary layers and cloud modeling. In this simulation, the cell perturbation method is also put off since the usage of a turbulent inflow in coarse resolution studies has not been utilized before and, moreover, appears to be questionable because the inertial subrange of the turbulence spectrum is not resolved anymore. Two additional simulation cases deal with modified surface characteristics. In the FLAT case the orography of the island is completely removed to study topographical effects on boundary layer and cloud characteristics. Surface heating is decreased by 50 % in the last sensitivity case (FLUX) to investigate to what extend turbulent structures and cloud generation are weakened due to reduced convective activity. Table 5.3 summarizes the settings for all aforementioned simulations.

5.2.2 Boundary layer and cloud characteristics

To get a qualitative impression of the local situation simulated by the LES model, Fig. 5.9 shows a three-dimensional snapshot of the temperature and humidity field as well as cumulus clouds with up- and downdrafts visualized by isosurface fields at 12:00 LT for the reference case. The daytime convection is clearly visible by multiple updraft cells distributed over the whole island area, which subsequently leads to the development of non-precipitating shallow cumulus clouds. Advection of heated air from the central and southern part of the island towards the west can be seen in the surface temperature field (which is meant as temperature of the lowest model layer in this context), whereas the cooler marine flow narrows the thermal wake toward the meridional center of the domain up to 40 km downwind. This effect is connected with an island-induced change of wind speed and direction. The change of the humidity profile can be observed in the vertical cut plane at the western model boundary. A large amount of moisture is transported vertically upwards in the central region where also occasional cumulus clouds are present. A few ten kilometers away in the y-direction, dryer air from heights of 500–1000 m is mixed downward.

Figure 5.10 shows a height-distance profile through $y = 50\,\mathrm{km}$. This cut plane intersects the grid point of the CIMH location and gives and idea of the daytime convective moisture transport. Regions at $x > 65\,\mathrm{km}$ are not or only very marginally affected by the island area. Turbulent mixing within the marine boundary layer up to 700–800 m altitude is visible in this area. Convective enhancement takes place at about one third of the island area connected with cloud generation, an increase of cloud base height and even cloud overshoots up to the top of the inversion layer around $z \approx 2\,\mathrm{km}$. Toward late afternoon, island effects become weaker and converge toward the marine background state. Especially around noon

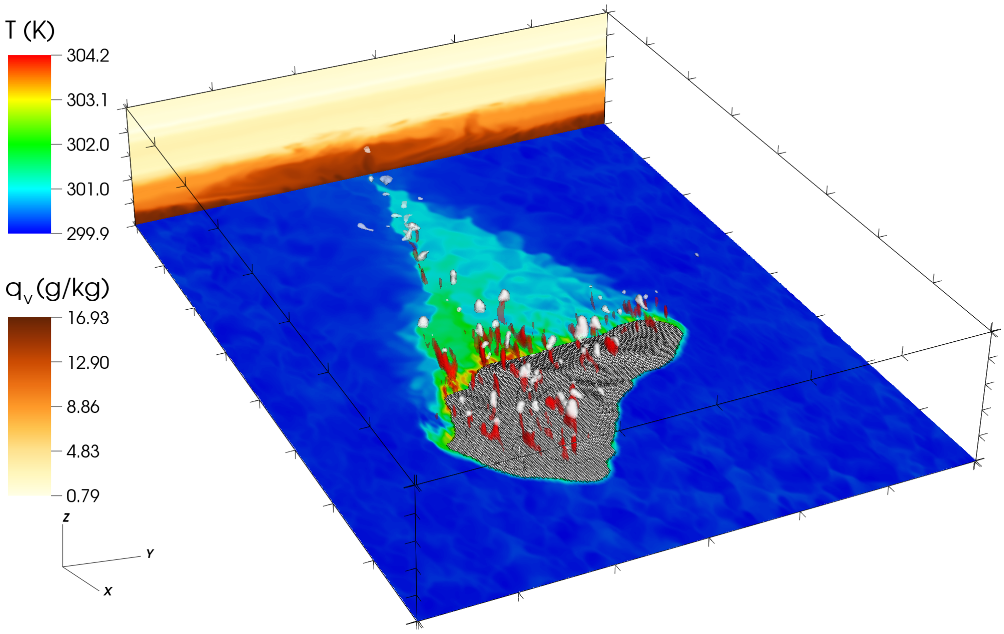

Figure 5.9: Perspective view of surface temperature and specific humidity field at the western boundary for the REF case. Clouds are visualized by $0.1\,\mathrm{g\,kg^{-1}}$ isosurface in white coloring. Red color depicts an isosurface of $2\,\mathrm{m\,s^{-1}}$ updrafts. Snapshot taken at 12:00 LT. A model volume of $80 \times 60 \times 5\,\mathrm{km^3}$ is shown.

(middle panel in Fig. 5.10) the upward mixing of moist air becomes apparent with maximum RH values between 1.2 and 1.5 km altitude – a prior dry layer with only RH $\approx 60\,\%$. A dry region with the same values can also be observed in the near-surface downwind region (approx. 20 km long) due to offshore heat advection.

A more quantitative analysis of the island effect as a whole can be done by comparing the island simulations with the periodic solution without the island. Due to the fact that the periodic reference solution is computed on a domain with half the domain length in x- and y-direction compared to the island simulations, each field from the periodic run is quadruplicated to fill out the full domain. Results of this procedure are shown in Fig. 5.11 for the virtual potential temperature θ_v and specific humidity q_v. The analysis reveals the spatial extent of island-induced heat and moisture changes at different heights. For a middle marine boundary layer altitude ($z = 375\,\mathrm{m}$), warmer ($\Delta\theta_v \approx 2\,\mathrm{K}$ max.) and dryer ($\Delta q_v \approx -6\,\mathrm{g\,kg^{-1}}$ min.) air is advected westwards, which matches well with the RH fields from the previous figure. Already at the top of the marine boundary layer at $z = 775\,\mathrm{m}$ there is still warmer air transported downwind but the sign in moisture difference changes toward more humid air. In addition to that, the transport direction is not strictly westwards but rather takes a conical form. A similar pattern is observed when analyzing the internal gravity propagation near the inversion layer, which will be discussed at the end of this chapter. In higher levels, the virtual potential temperature does not significantly change anymore in the downwind region, however, upward moisture transport is still present up to 2 km height asl.

For further insight into flow dynamics, especially for the downwind region, Fig. 5.12 provides the vertical wind field at $z \approx z_i/2$ in the afternoon for all six considered cases from Table 5.3. Looking at the REF and INV case, several turbulent updraft bands with lengths of about 10 km in zonal direction and vertical velocities up to $2.5\,\mathrm{m\,s^{-1}}$ develop all over the island area. However, one main band at $y \approx 52\,\mathrm{km}$ remains persistent, even at higher altitudes. Such updraft bands can be a result of the dynamic and/or thermal instability over the island. In the case of Barbados, the low heat capacity of the island surface relative to water leads to a thermally forced island convection, which is the predominating effect. It should be noted here that mechanical forcing may still influence the updraft band location as well as its intensity and organization (cf. Kirshbaum and Wang, 2014; Kirshbaum and Fairman, 2015). Eventually, quasi two-dimensional horizontal vortex rolls with their axes aligned in the downwind direction (e.g., Etling and Brown, 1993) are

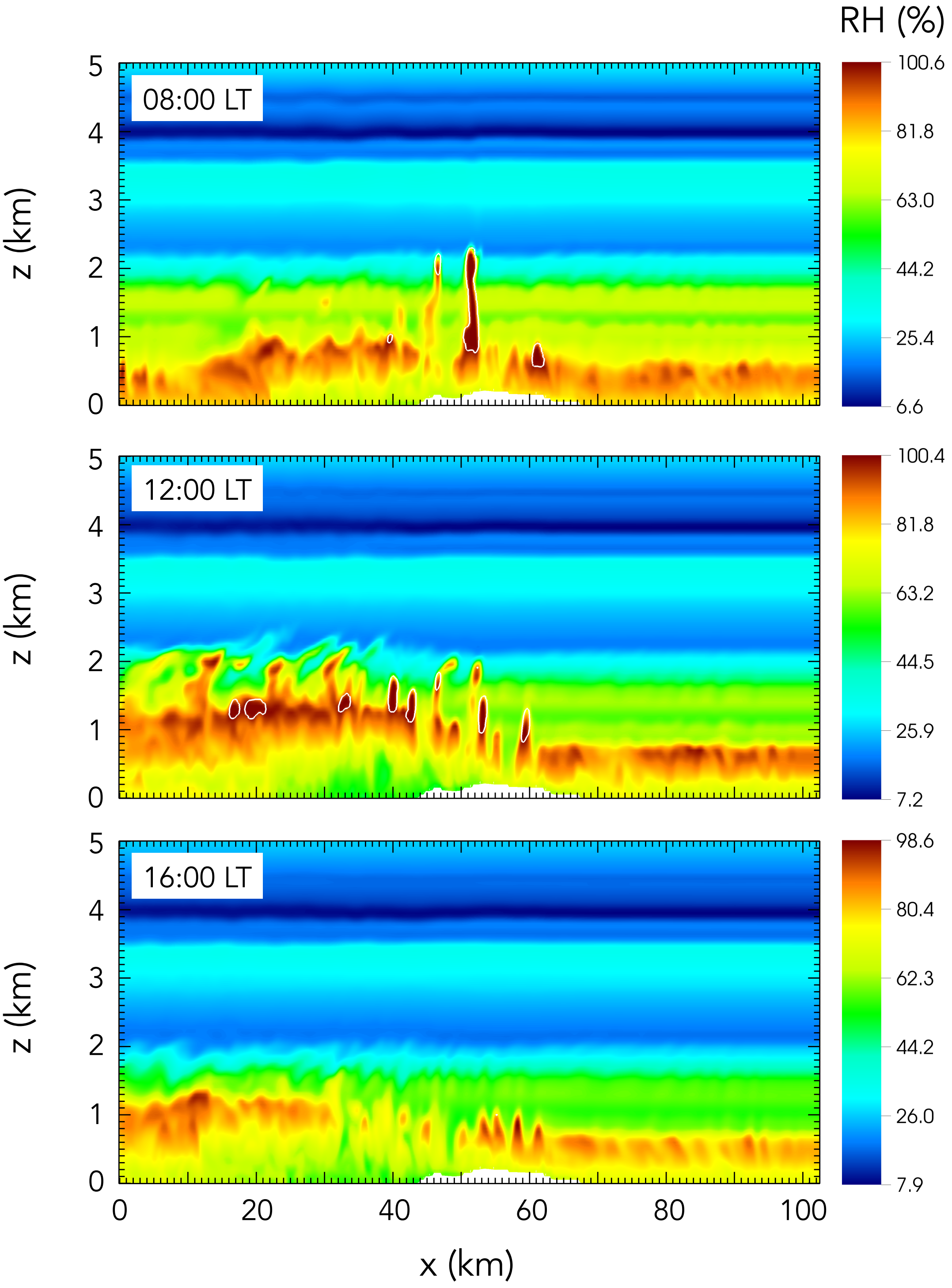

Figure 5.10: LES model output (REF case): zonal height-distance profile of relative humidity at $y = 50\,\mathrm{km}$ (13° 08' 53" N latitude) for different times on 22 June 2013. White contours correspond to $q_c = 0.01\,\mathrm{g\,kg^{-1}}$.

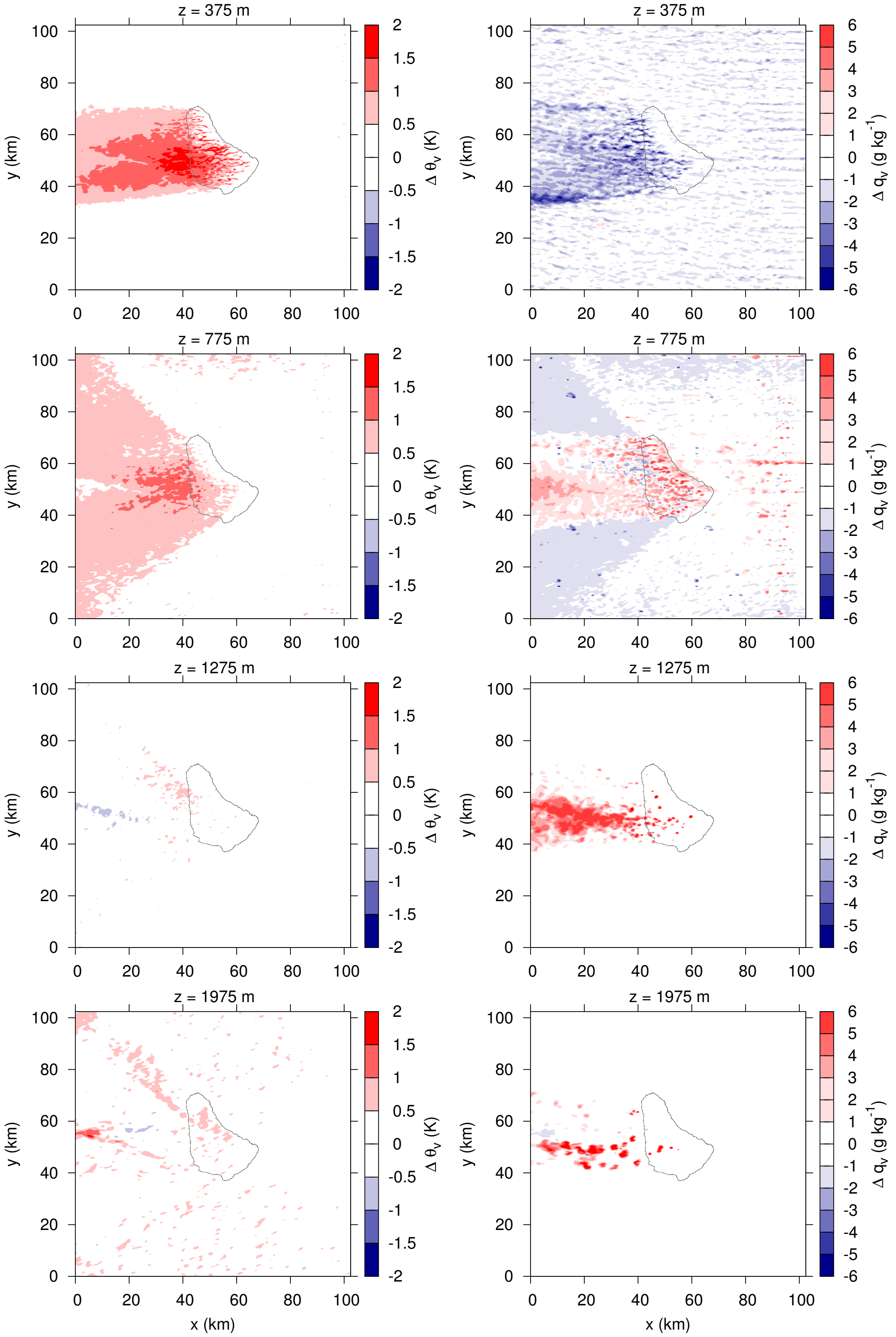

Figure 5.11: Difference θ_v and q_v fields at several height levels. The difference is calculated between the REF case at 12:00 LT and the steady-state periodic solution without the island.

generated. Figure 5.13 shows a meridional cut plane at $x = 30\,\mathrm{km}$ (which is around 12 km off the west coast) where the specific humidity field and vertical velocity contours are displayed. The main updraft band is located at $y \approx 48\,\mathrm{km}$ where positive updrafts of $w > 0.25\,\mathrm{m\,s^{-1}}$ are simulated up to an altitude of $z = 1300\,\mathrm{m}$. Toward the evening, as the surface sensible heat flux is not positive anymore and convection fades away, the band decouples from the island and vanishes (not shown). Turbulent updraft cells within the marine boundary layer with vertical velocities between $0.5\,\mathrm{m\,s^{-1}}$ and $1\,\mathrm{m\,s^{-1}}$ are also visible since a turbulent inflow is generated with the cell perturbation method described in Section 2.5. In the INV case, these updrafts are a bit weaker, which is most likely due to the stronger mean horizontal wind speed.

Wave-like structures in the upwind vertical velocity field are observed in the NOCP case. There, the flow remains laminar in this region and since no perturbation is applied but surface fluxes are present, artificial convergence lines are forming. Note that this effect is not seen in the REF and INV case. This underscores the importance of having an explicit inflow turbulence generation when working on LES scales. Just by visibly comparing the "coarse" simulation DX400 with the other cases, it becomes apparent that there is a lot of structure loss in the vertical wind field. All up- and downdraft bands – even the main updraft band downwind – are almost perfectly aligned in x-direction. This shows the importance of using a grid spacing that resolves the inertial subrange of the velocity spectrum (cf. Bryan et al., 2003). Note that with coarser grid spacings the orographical structures of the island are also less represented. In the FLAT case the mean updraft structure is conserved with the same main updraft band intensity and position. There are slight differences at the first few kilometers over the eastern island area where in the REF case vertical winds are already present, which are missing in FLAT. If the island surface sensible heat flux is halved (FLUX), there is an expected lower strength in the vertical wind field. An updraft band with weaker updrafts is still visible. However, it does not appear to be continuous anymore.

Figure 5.14 shows the surface wind fields and liquid water path for all simulated cases at 14:00 LT. In all these cases, the island convection affects both the strength (up to $4\,\mathrm{m\,s^{-1}}$ stronger wind speeds compared to marine surface winds) and direction ($\pm 30°$) of the wind in the downwind area of Barbados, thus leading to strong surface convergence and subsequently forming the updraft band as seen in Fig. 5.12 at $y = 52\,\mathrm{km}$. Despite having this elongated band, very little cloud formation is observed in this area for all cases except DX400, which is also the

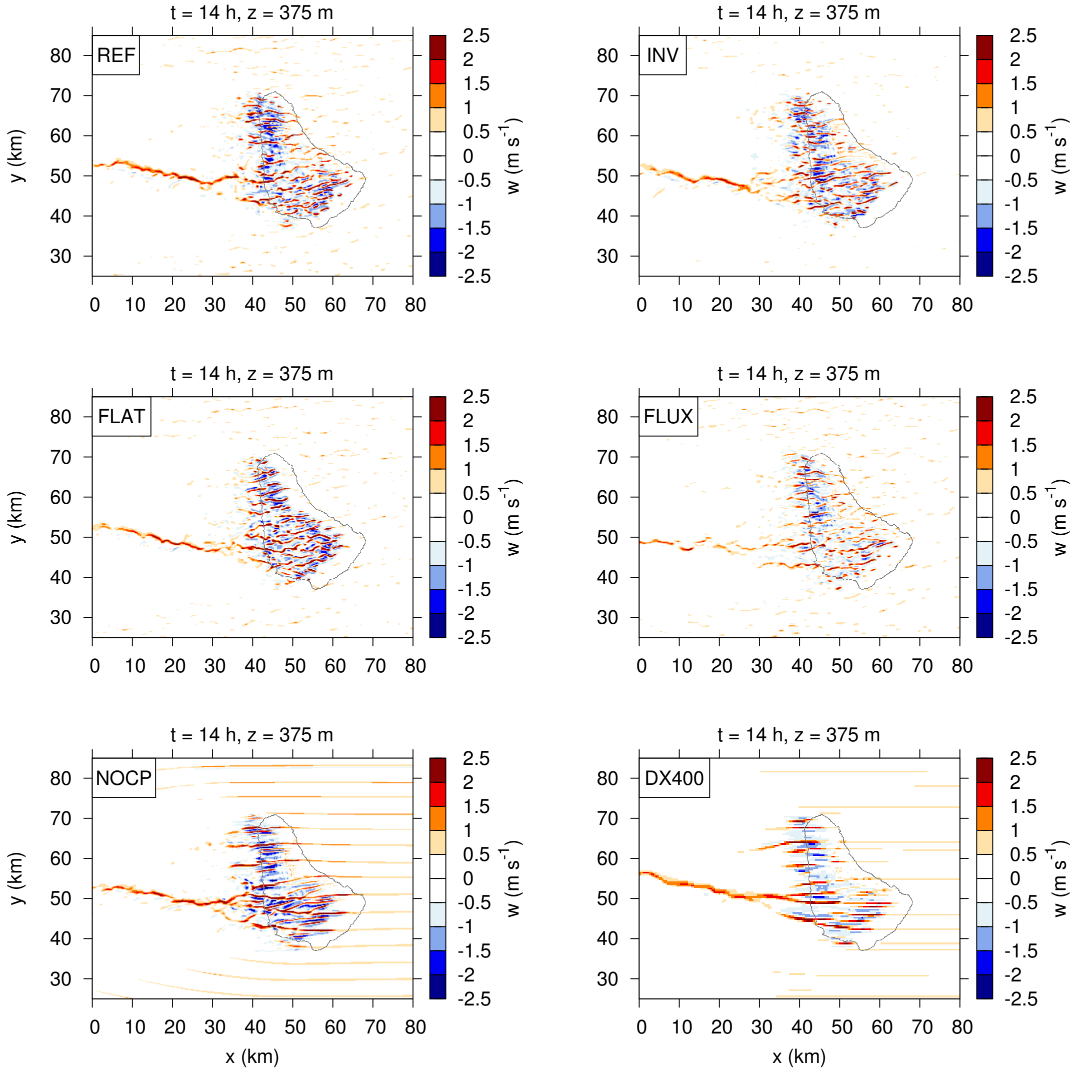

Figure 5.12: Vertical wind at $z = 375\,\text{m}$ height asl at 14:00 LT for the six simulation cases (see Table 5.3).

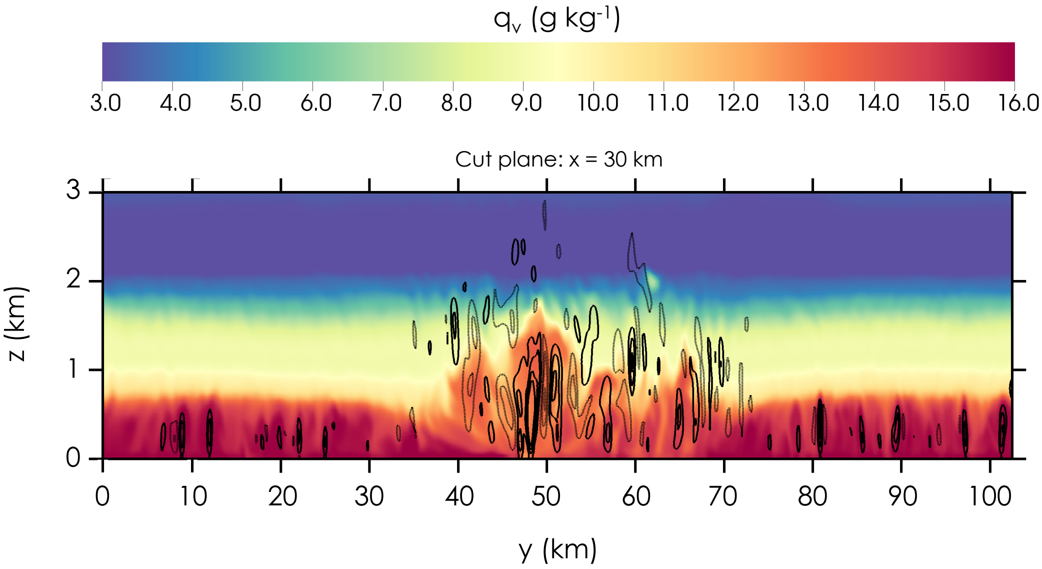

Figure 5.13: Meridional cut plane at $x = 30\,\mathrm{km}$ (cf. Fig. 5.12) at 14:00 LT for the REF simulation. The specific humidity field and contours of vertical velocity (solid lines = updrafts, dashed lines = downdrafts, contour interval is $0.25\,\mathrm{m\,s^{-1}}$) are shown.

case for other times of the day (not shown). This means that no continuous cloud street is modeled on the 22 June 2013 and the 27 June 2013, respectively. While cloud streets occur on around 60 % of undisturbed days, there are several effects that suppress cloud street generation (Kirshbaum and Fairman, 2015). In the cases initialized by the 22 June 2013 data (all cases except INV), the relatively low moisture load (RH = 80 % near the surface, decreasing below 60 % at $z \approx 1300\,\mathrm{m}$) and a weak trade wind inversion leads to a non-formation of a cloud trail. The only exception is the DX400 case, which is discussed later on. Both moisture and stratification are increased in the INV case but the stronger mean trade winds (almost $12\,\mathrm{m\,s^{-1}}$) are the suppressing factor here (Kirshbaum and Fairman, 2015). Due to the absence of a turbulent inflow velocity field, the cumulus clouds over the island are horizontally aligned to the mean wind direction in the NOCP case. In the REF and INV cases, more realistic scattered cumulus cloud fields over the island area and downwind are modeled. Besides the distinct cloud bands, the DX400 case shows further very notable differences in the cloud field. First of all, clouds are broader because of the coarser grid spacing. In addition to that, a continuous cloud street is modeled, which can be considered as an artifact since such a cloud band is neither seen in other simulations nor in satellite observations. Furthermore, the

Table 5.4: Diagnostics the six sensitivity simulations (see Table 5.3), including cloud cover, cloud base height z_{cb}, cloud top height z_{ct}, boundary layer height z_i, water vapor path (WVP), liquid water path (LWP), and maximum updraft values $w_{\max}$. All quantities are spatially averaged for the downwind area and temporally averaged between 06:00 and 18:00 LT.

Case	Cloud cover (%)	z_{cb} (m)	z_{ct} (m)	z_i (m)	WVP ($\mathrm{kg\,m\,kg^{-1}}$)	LWP ($\mathrm{g\,m^{-2}}$)	$w_{\max}$ ($\mathrm{m\,s^{-1}}$)
REF	7.8	967	1167	1240	27.6	8.5	5.0
INV	8.6	846	1024	1174	33.2	5.9	4.5
NOCP	11.0	1066	1269	1222	27.7	18.8	5.2
DX400	9.7	1029	1237	1262	29.3	19.0	3.7
FLAT	5.5	898	1083	1191	28.5	6.6	4.9
FLUX	4.9	811	966	1100	27.6	4.8	3.9

downwind horizontal velocity field is slightly stronger compared to the other cases. This behavior can be attributed to the lack of resolved small scales that cannot extract energy from the large eddies and therefore grow and become more coherent. This effect is also observed to a lesser extent for the NOCP case. Considering the FLAT case, a similar flow convergence pattern downwind can be observed. In REF however, there is a stronger flow acceleration due to orographic turbulence. Furthermore, the distribution of island-induced cumulus cloud is different in the FLAT case compared to REF. If orography is present, scattered cumulus clouds are present all over the island area, whereas without orography their are more concentrated along a zonal lane between $45\,\mathrm{km} < y < 50\,\mathrm{km}$. In the FLUX case the downwind wake is overall weaker together with less and smaller cumulus clouds.

In the following, the diurnal development of the convective island boundary layer is investigated. Figure 5.15 shows time series of boundary layer and cloud properties for the downwind region around the west coast of Barbados. Further mean quantities of boundary layer and cloud characteristics are diagnosed and summarized in Table 5.4.

The REF and the INV case have some properties in common. They both show a strong increase of cloud cover in the downwind region between 07:00 and 08:00 LT up to a maximum value of about 16 %. The boundary layer height z_i displays

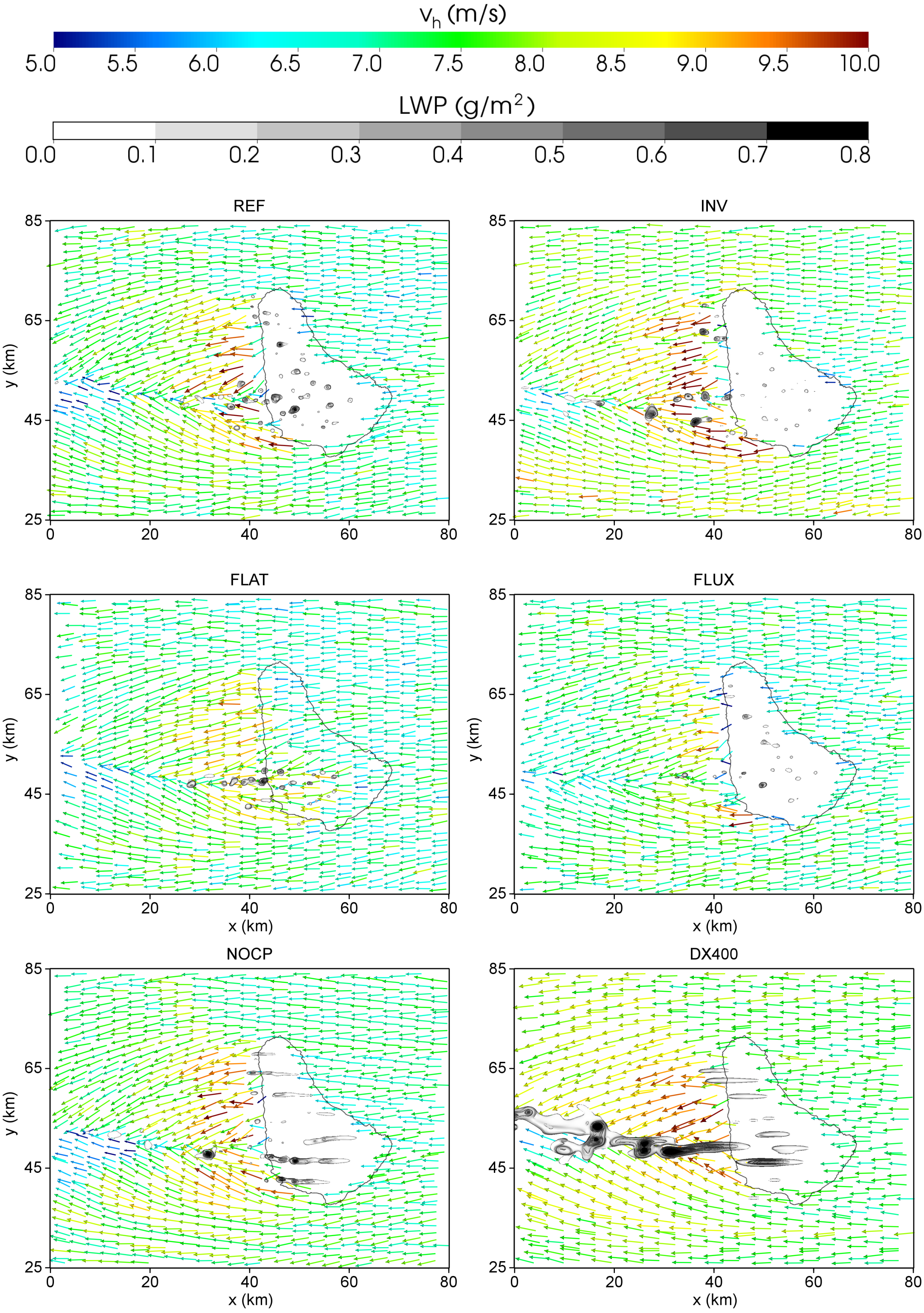

Figure 5.14: Horizontal cut planes (xy) of surface wind vectors and contours of liquid water path for all six simulation cases (see Table 5.3).

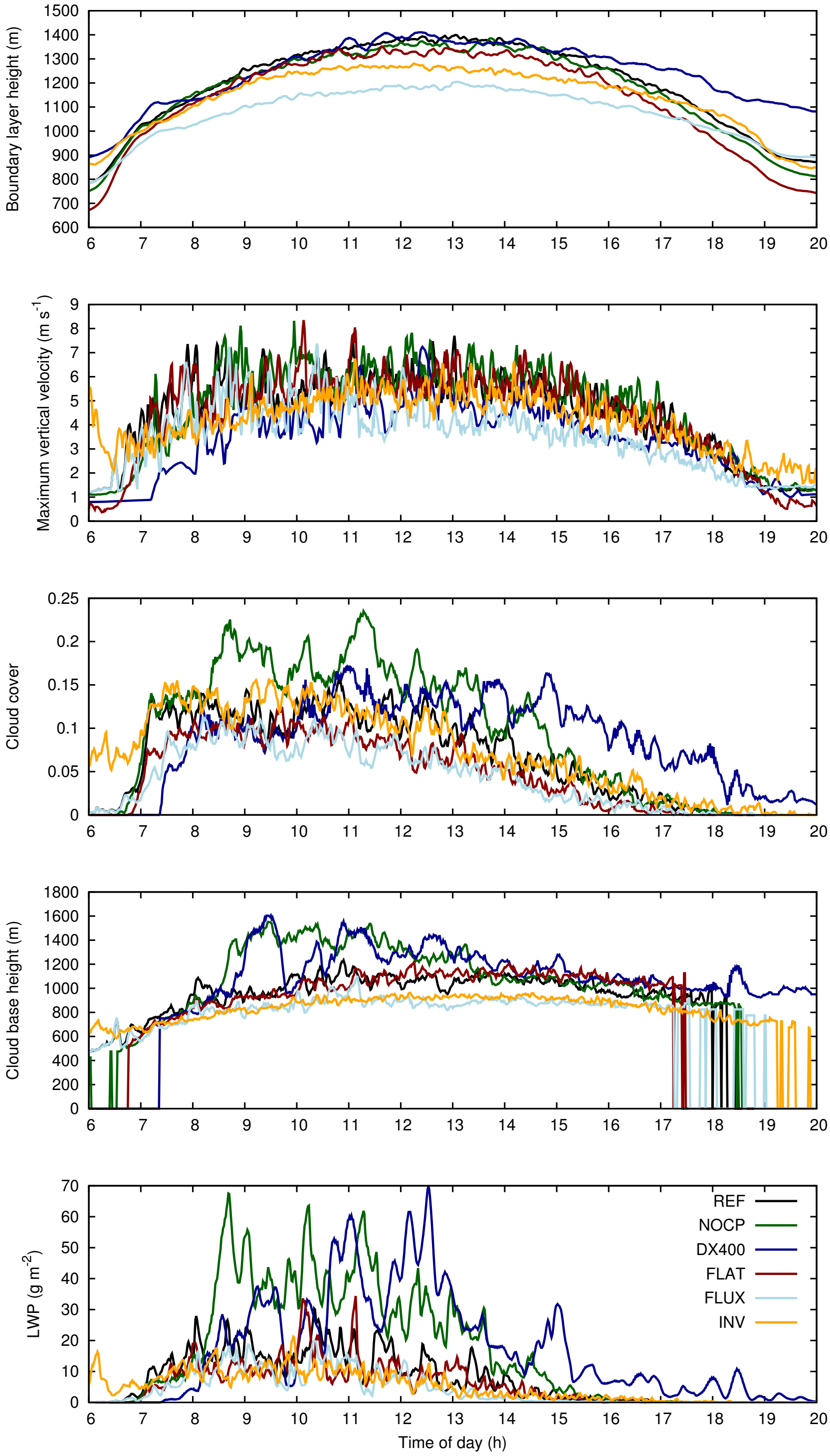

Figure 5.15: Time series of boundary layer height, maximum vertical velocity, cloud cover, cloud base height and liquid water path for the downwind domain. Spatial averaging as indicated in Fig. 5.8.

a diurnal variation, growing up to $z = 1350$ m around 13:00 LT in the REF case. For the INV simulation, z_i is approximately 100–150 m shallower. This parameter is calculated via the Bulk Richardson criterion, where the boundary layer height is defined as the height where the Bulk Richardson number Ri_b exceeds a value of 0.25, with

$$\mathrm{Ri}_b = \frac{g}{\theta_{v0}} \frac{\theta_v - \theta_{v0}}{u^2 + v^2} z \,, \tag{5.10}$$

where θ_{v0} is the virtual potential temperature at the surface. Being relatively similar in boundary layer characteristics and cloud cover, there is a clear distinction between REF and INV with regard to cloud microphysical properties. Due to higher cloud base height in the REF case, the cumulus clouds tend to grow deeper, which is seen in the mean LWP values as well as in the cloud base and top heights (cf. Table 5.4). The cloud cover, however, is fairly comparable for these two cases. Peak updraft values also show a diurnal variation, starting from approximately $w_{\mathrm{max}} = 1\,\mathrm{m\,s^{-1}}$ (which is equivalent to the upwind area value) up to $w_{\mathrm{max}} = 7\,\mathrm{m\,s^{-1}}$ around noon. The DX400 case has overall weaker peak updrafts, however this does not mean that there is less vertical transport of energy, moisture, momentum etc. Due to the coarser grid spacing in every spatial direction there is a higher net upward transport. In the FLUX case almost all quantities of interest have lower values, which is expected due to the weaker forcing. Boundary layer and cloud base heights are reduced by about 150 m, the average LWP is almost halved and the mean maximum updrafts are decreased by $1\,\mathrm{m\,s^{-1}}$. A flat island surface also leads to weaker convective activity over the island with its subsequent effects. However, the weakening is not that pronounced as in the FLUX case, e.g., the reduction of cloud base and BL height are only 50 m.

To further investigate daytime-dependent vertical mixing and layering, Fig. 5.16 shows hourly averaged vertical profiles boundary layer and cloud parameters for the downwind domain compared to the daily upwind average. Due to the large differences between the convective island boundary layer quantities and those of the marine boundary layer, Fig. 5.17 shows the upwind profiles exemplarily for the REF case with a suitable scale. Comparing the REF and INV cases, daytime dependent differences in the density potential temperature and specific humidity profiles can be noticed (these profiles are shown in Appendix B). Lower levels at $z < 700$ m are warmer and dryer compared to the marine background. The vertical turbulent transport is evidenced by the profiles of sensible and latent heat fluxes. The sensible heat flux is linearly decreasing within the mixing layer up to heights between $700\,\mathrm{m} < z < 900\,\mathrm{m}$, depending on the time of day. The maximum latent

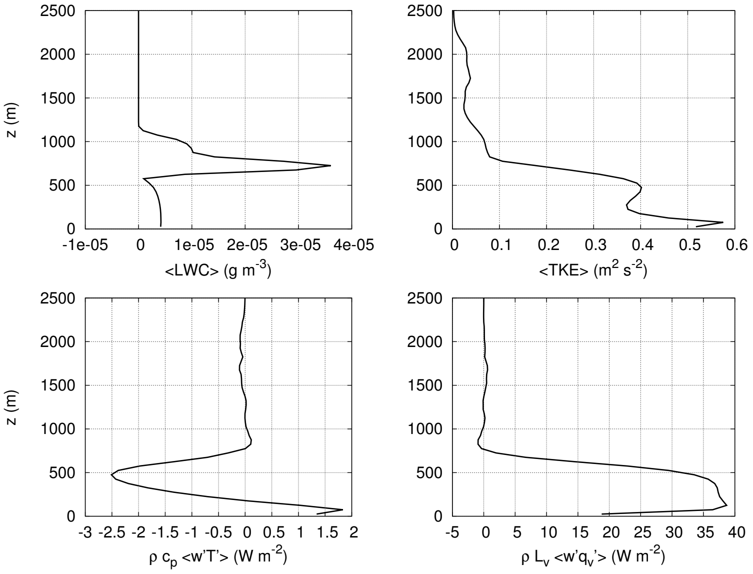

Figure 5.16: Vertical profiles of liquid water content $\langle \mathrm{LWC} \rangle$, resolved turbulent kinetic energy $\langle \mathrm{TKE} \rangle$, sensible and latent heat flux $\rho_0 c_{pd} \langle w'T' \rangle$ and $\rho_0 L_0 \langle w'q_v' \rangle$ for the marine upwind domain in the REF case. Spatial averaging as indicated in Fig. 5.8. The profiles are temporally averaged between 08:00 and 20:00 LT.

heat fluxes occur between $600\,\mathrm{m} < z < 800\,\mathrm{m}$. Above that layer, the cloud water content reaches its maximum, which is connected to latent heat release and thus to an increase of the sensible heat flux and a decrease of the latent heat flux. In the INV case, the trade inversion around $z \approx 2000\,\mathrm{m}$ inhibits further cloud development above this height, whereas in the REF simulation there is also a notable amount of cloud water above 2000 m. The presence of wind shear above 1500 m height leads to a secondary maximum of TKE around $z = 2000\,\mathrm{m}$, which is not the case in the shearless INV simulation.

In the NOCP case, i.e., without a turbulent inflow, persistent updraft bands form over the island area, which is consistent with the modeled cloud field from Fig. 5.14. The inflow characteristics have little effect on boundary layer properties like TKE, vertical velocity variance (not shown), sensible and latent heat flux (cf. Fig. 5.16). However, the values for the NOCP case tend to be a bit higher than in REF, especially between 500 and 700 m. One reason for this could be that the upwind marine boundary layer already vertically transported some amount of energy, which is missing in the NOCP case. More remarkable differences are noticeable with regard to cloud development. The LWC around $z \approx 1000\,\mathrm{m}$ during

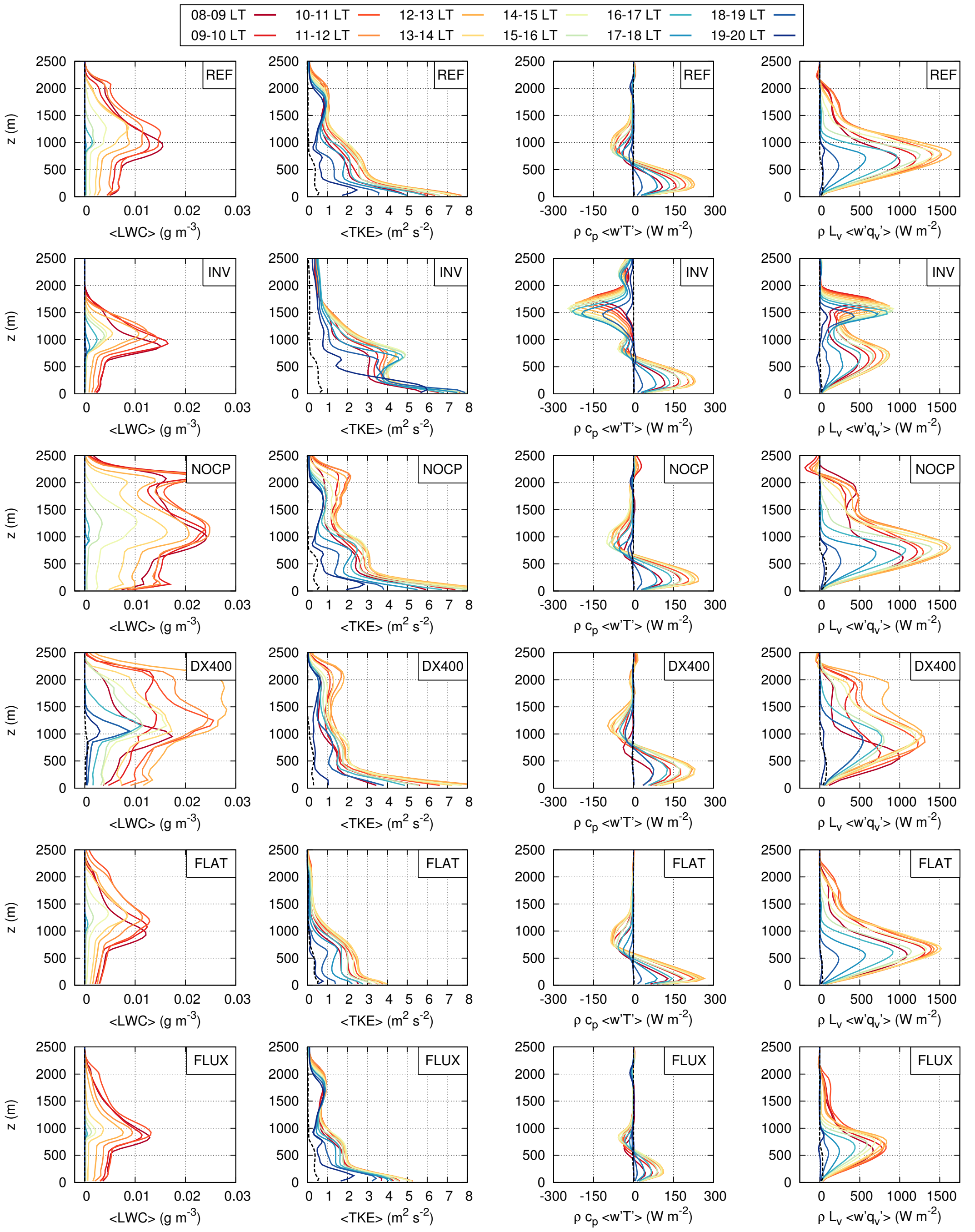

Figure 5.17: Vertical profiles of liquid water content ⟨LWC⟩, resolved turbulent kinetic energy ⟨TKE⟩, sensible and latent heat flux $\rho_0 c_{pd} \langle w'T' \rangle$ and $\rho_0 L_0 \langle w' q'_v \rangle$ for all six considered cases (REF, INV, NOCP, DX400, FLAT and FLUX from top to bottom). Spatial averaging as indicated in Fig. 5.8. Black dashed lines represent the marine upwind area and are temporally averaged between 08:00 and 20:00 LT. Colored solid lines stand for hourly averages during different times of the day for the downwind area.

noon is nearly doubled for the NOCP case. There is also a particularly pronounced secondary maximum of LWC around $z \approx 2100\,\mathrm{m}$ in the same order of magnitude. Taking the average over the whole daytime period, the mean LWP is more than doubled in the NOCP case compared to the REF case, which is in agreement with higher LWC values and also higher cloud cover ($\approx +3\,\%$). More undesired effects become apparent when using a coarser spatial resolution as in the DX400 case, which is most noticeable in the averaged vertical profiles. First of all, there is less variability in the potential temperature and specific humidity fields for altitudes $z > 1000\,\mathrm{m}$, which can be explained by the lack of turbulent vertical transport within the boundary layer (this effect can be seen in the vertical profile of TKE in Fig. 5.16 and in the profile of the vertical velocity variance). The LWC however has maximum values of $0.028\,\mathrm{g\,m^{-3}}$ around $z \approx 2000\,\mathrm{m}$, which is factor 2 higher compared to the REF case. This is accompanied by strong latent heat fluxes in these layers. Cloud growth is also more inhibited at finer resolutions due to explicit entrainment of dryer environmental air (e.g., Bryan et al., 2003). Having a distinct and quite symmetric diurnal variation of boundary layer and cloud properties in the other cases, the evening transition in the DX400 case is poorly represented, where still a notable amount of clouds exist and a deeper boundary layer is modeled around 20:00 LT.

Orographic effects are revealed in the LWC and the turbulent flux profiles. The maximum of sensible heat flux is shifted slightly downwards, which explains lower cloud base heights in the FLAT case. There is also the lowest amount of TKE in the near-surface levels among all sensitivity simulations due to the absence of orographic turbulence. There is also no second peak in the TKE profile in the trade inversion layer between $1700\,\mathrm{m} < z < 2200\,\mathrm{m}$. Turbulent flux profiles in the FLUX case are less pronounced as it could be anticipated. However, the TKE around the trade inversion is of the same magnitude as in other cases because the gravity wave activity there is driven by the mean geostrophic forcing. The maximum LWC in the FLUX case is comparable to the REF and FLAT cases, respectively, despite the fact that the clouds form at lower altitude.

5.2.3 Vertical mixing of aerosols

After the long-range transport of Saharan dust into the Caribbean region, these dust layers arrive at Barbados having mean base heights of about 1.5–2 km asl. Due to a possible interaction with the convective island boundary layer, vertical mixing of aerosols and layer movement are investigated in this subsection. As already shown in Section 5.1, these aerosol layers are represented by passive tracers in the model. They are initialized with a relative concentration of 1 within the layer where the aerosol is detected and 0 else. This approach has already been used for heat island effect studies in Engelmann et al. (2011). These relative concentrations can be related to mass concentrations of Saharan dust, e.g., $180\,\mu g\,m^{-3}$. This mass concentration and the Saharan dust layer heights are estimated from ground-based multi-wavelength aerosol lidar measurements (Moritz Haarig, personal communication, 20 July 2015) and provide a rough idea of the magnitude of these quantities.

Figure 5.18 displays height-distance profiles of the boundary layer tracer ϕ_{BLT} and the Saharan dust tracer ϕ_{SDT} near the west coast of Barbados. In both cases, the turbulent character over the island section is visible as a vertical distribution of the passive tracer within the higher boundary layer and the corresponding decrease in tracer concentration. It is more pronounced for the southern part of the island, which is due to the broader land area width (20 km in the south compared to 10 km in the north). It also indicates the wind shear at the island boundaries (e.g., at $y = 43\,\mathrm{km}$), which causes the advection of air masses from $z > 700\,\mathrm{m}$ into the boundary layer. This effect is more pronounced further west (not shown). In the REF case, the mean boundary layer height around noon was calculated to be $z_i \approx 1400\,\mathrm{m}$. The passive tracer analysis additionally shows some local overshoots up to over 2 km height asl. These convective instabilities are also seen in the isentropic field (black lines in Fig. 5.18). The Saharan dust tracers do have a different vertical structure. For the REF simulation, the tracer is thinned out, with maximum concentrations between $1.9\,\mathrm{km} < z < 2.4\,\mathrm{km}$, whereas in the INV case it is between $1.7\,\mathrm{km} < z < 2.5\,\mathrm{km}$. There are also no overshoots visible beyond $z = 1.7\,\mathrm{km}$. The stronger turbulent mixing in the REF case can be explained by the presence of wind shear around $z \approx 1.5\,\mathrm{km}$ height, whereas in the INV case the strong trade wind inversion suppresses further development of turbulence in higher altitudes.

Although there are already some indications of downward aerosol transport, a better quantification of these effects is still needed to achieve an improved understanding of the processes behind it. For that reason, mean vertical profiles are calculated in the same manner as in the boundary layer and cloud analysis. Figure 5.19 shows vertical profiles of tracer-related quantities for the REF and the INV case, respectively. The tracer profile is getting deformed by vertical transport processes,

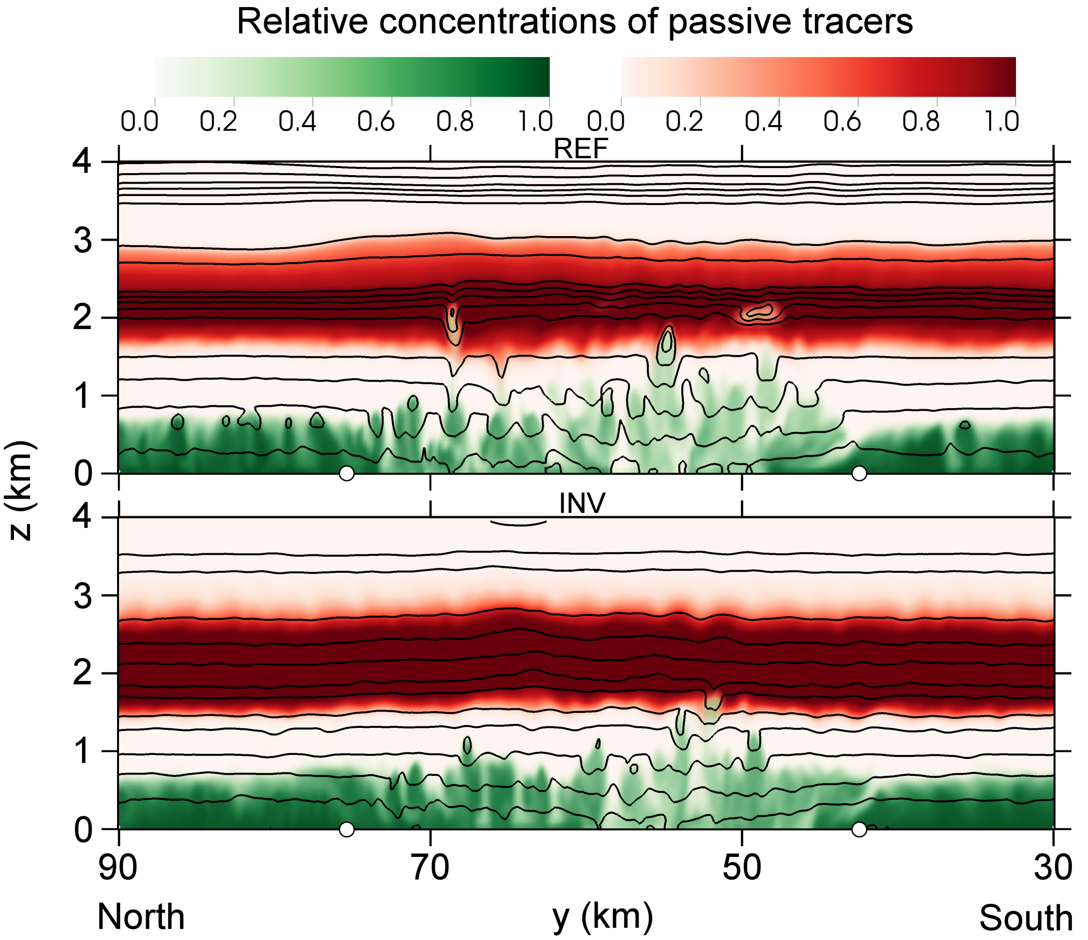

Figure 5.18: Meridional cut planes (y-z profiles, 3 km off the west coast of Barbados) of the relative passive tracer concentrations and isolines of equivalent potential temperature θ_e (solid black lines, contour interval 1 K) for the REF (top panel) and the INV case (bottom panel), respectively. Red coloring represents the Saharan dust tracer concentration ϕ_{SDT} and green coloring represents the boundary layer tracer concentration ϕ_{BLT}. White circles denote the location of the northern and southern island edges. The snapshots are taken at 12:00 LT.

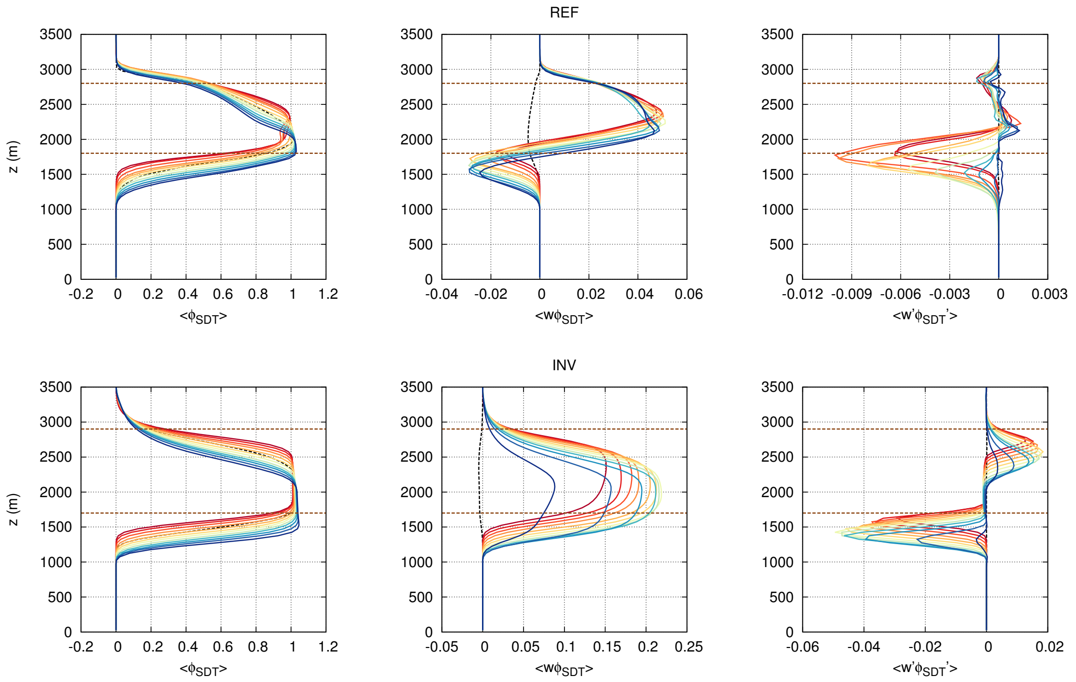

Figure 5.19: Vertical profiles of the passive Saharan dust tracer $\langle \phi_{\mathrm{SDT}} \rangle$ (left panel), the total vertical tracer flux $\langle w\phi_{\mathrm{SDT}} \rangle$ (middle panel) and the resolved turbulent tracer flux $\langle w'\phi'_{\mathrm{SDT}} \rangle$ (right panel) for the REF case (top row) and the INV case (bottom row). Solid line colors, spatial and temporal averaging as in Fig. 5.16. The horizontal brown dashed line represents the initial location of the Saharan dust tracer between $1800\,\mathrm{m} \leq z \leq 2800\,\mathrm{m}$ for REV and between $1700\,\mathrm{m} \leq z \leq 2900\,\mathrm{m}$ for INV.

which can be originated by larger-scale or turbulent processes. To distinguish between those two, the total vertical tracer flux $\langle w\phi_{\mathrm{SDT}}\rangle$ as well as the turbulent vertical tracer flux $\langle w'\phi'_{\mathrm{SDT}}\rangle$ are computed. According to the model data, there already is a persistent downward movement east of Barbados within a layer between $1.5\,\mathrm{km} < z < 3.0\,\mathrm{km}$, which corresponds to a subsidence velocity of $w = -407\,\mathrm{m\,day^{-1}}$ for the REF case and $w = -345\,\mathrm{m\,day^{-1}}$ for the INV case. There is a total relative downward flux for the downwind area in the REF case at 1.7 km height, with a maximum magnitude of $\langle w\phi_{\mathrm{SDT}}\rangle = -0.03\,\mathrm{m\,s^{-1}}$. The height of this local extremum depends on the time of day, with higher altitudes in the morning and around noon and lower altitudes toward the evening. A net positive upward flux is always present above $z = 2\,\mathrm{km}$, becoming zero at $z = 3\,\mathrm{km}$. About one third to one half of the total downward flux is caused by turbulent mixing, having their local maxima at $z = 1.8\,\mathrm{km}$, which is the lower bound of the Saharan dust layer. The daytime turbulent downward mixing is about five times stronger in the INV case but is shifted approximately 400 m toward the surface compared to REF. Due to the tracer subsidence, the layer also reaches these altitudes of maximum turbulent downward mixing, which would not be the case if the dust layer remained at its initial height of 1.7 km. The downwind total tracer flux, however, is positive (upwards) for all altitudes and is almost one order of magnitude stronger compared to REF. Since the mean wind speed only slightly differs between the two cases and surface fluxes are the same, it can be concluded that atmospheric stability (especially inversion strength), moisture load effects and the presence of wind shear in the sub-inversion layer have a major impact on altitude and strength of layers with preferably upward or downward mixing properties. The model data suggests that the net effect, i.e., effects from both mean transport and turbulent vertical mixing is a downward transport around the dust layer base for the downwind region in REF and a net upward transport in INV.

5.3 Comparison with Raman lidar data

In the framework of the SALTRACE campaign the polarizing Raman lidar BERTHA (Backscatter, Extinction, lidar Ratio, Temperature, Humidity profiling Apparatus, Tesche et al., 2009) was deployed at the Caribbean Institute of Meteorology and Hydrology at the west coast of Barbados. Radiosondes were launched by TROPOS twice a day and more frequently at intensive measurement periods. Continuous measurements were performed on 22 June 2013 from 9:49–17:23 LT and after sunset (around 18:30 LT) from 19:32–22:30 LT. The range-corrected signal for the 532 nm cross polarized channel is shown in the top panel of Fig. 5.20. The vertical resolution is 7.5 m and the time resolution varies from 3 to 15 seconds. The mean wind speed (< 3 km altitude) was approx. 10 m s^{-1}, which results in a horizontal resolution of 30 to 150 m. A first strong dust layer in a very dry environment (20-30 % RH) was detected between 1.8 and 2.8 km, topped by a second, weaker dust layer between 2.8 and 3.7 km, which was more humid (40-50 % RH). Temperature inversions set the limits of the total dust layer or Saharan Air Layer. The lidar signal shows clouds all over the day around 1 km height and close to 1800 m. On average, 20 clouds per hour cross the lidar beam with an increasing number in the afternoon, leading to a cloud cover (in this context defined on a temporal scale) of roughly 50 %. At nighttime only a single cloud was detected within three hours of measurement. That confirms the convective character of the daytime clouds at the investigated day over the west coast of Barbados. The bottom panel in Fig. 5.20 shows the LES model output of the corresponding height-time profile of relative humidity for this day and the same location. The diurnal variation of convective vertical moisture transport is clearly pronounced. Clouds (white/red colors) develop at the same altitudes as in the BERTHA lidar measurements. Even higher and deeper clouds up to the top of the trade inversion at $z = 2$ km are resolved. Higher cloud activity can be noticed in the measurements, whereas the LES model results show less clouds toward the late afternoon. This effect can be attributed to the relative low ocean latent heat flux from the marine boundary layer forcing, which tends to dry out the lower troposphere over a longer period of time (i.e., toward the afternoon and evening hours). Additionally, there is a notable increase of moisture during the afternoon (cf. the 16:01 LT radiosonde launch compared to the other ones) within the first 800 m of the lower troposphere. Because of the fact that no additional large-scale forcing (in this case, advection of moist air) is applied during the simulation time, this effect can expectedly not be captured by the LES.

Further comparisons regarding the cloud base height are conducted to achieve an even better relation between the BERTHA lidar measurements and the model results. Figure 5.21 shows the temporal evolution of the cloud base height derived from the REF case LES output and the cloud base height derived from BERTHA lidar measurements during the 22 June 2013. The cloud base was detected from the lidar signal with an accuracy of ±50 m. The algorithm sets the cloud base if the 52.5 m vertically smoothed 532 nm total signal increases by a factor of 2 within 50 m. To get an overview of the day, the temporal resolution was set to

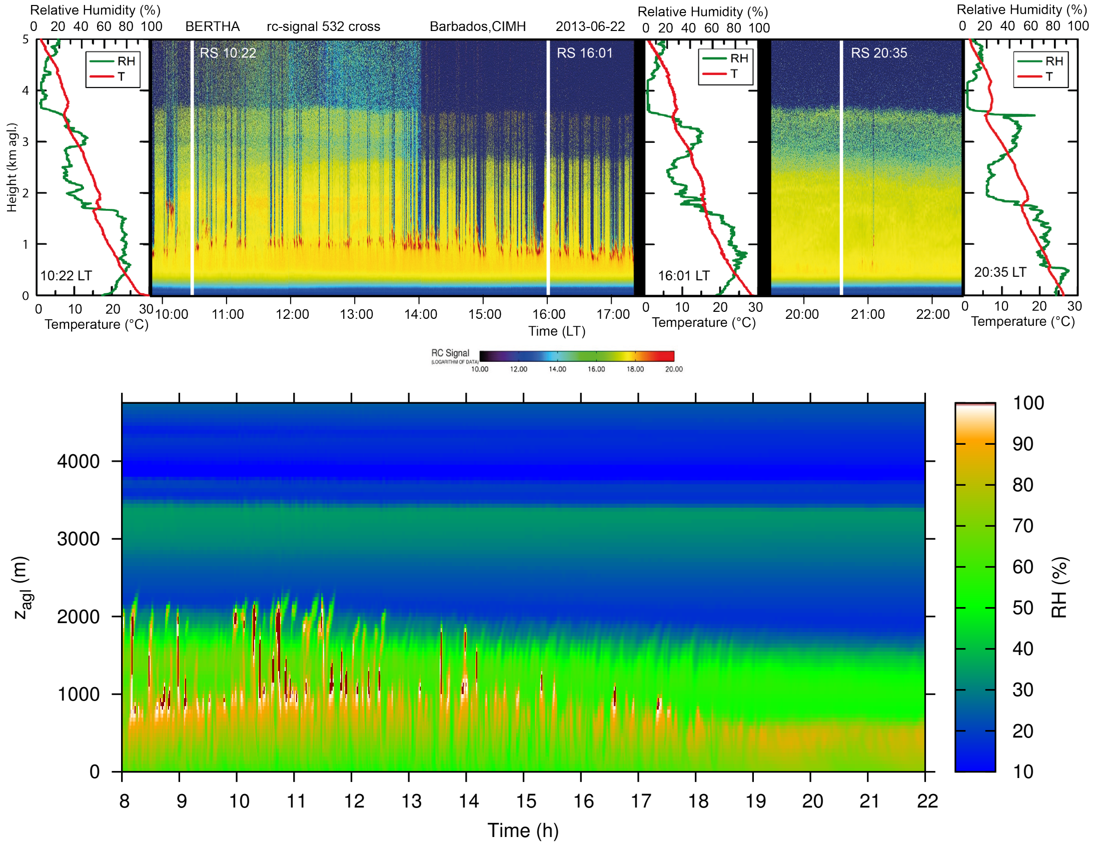

Figure 5.20: Top panel (image courtesy of Moritz Haarig): BERTHA lidar measurements at CIMH and 3 radiosonde profiles of 22 June 2013. The range corrected signal of the 532 nm cross polarized channel is shown. The aerosol layer (in yellow) reaches up to 3.7 km. The signal peaks (in red) are liquid clouds through which the lidar beam cannot penetrate, resulting in the lack of signal above the cloud. At 14:04 LT the temporal resolution was changed from 15 s to 3 s. Bottom panel: LES model results of relative humidity at the CIMH grid point for the REF case, corresponding to 22 June 2013.

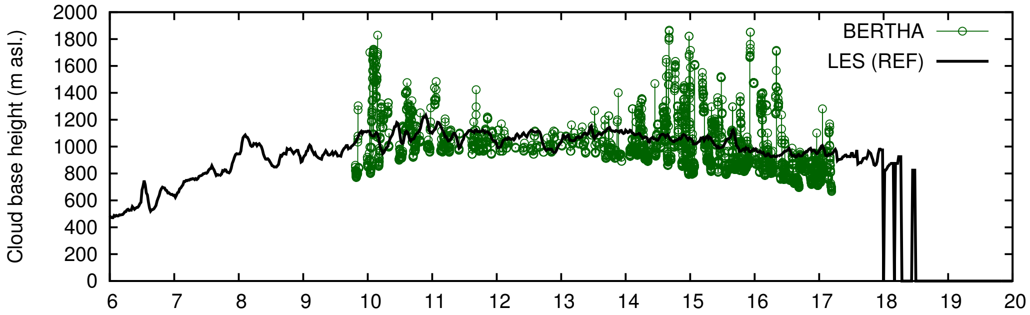

Figure 5.21: Temporal evolution of the spatially averaged cloud base height from the LES REF case (black line) and cloud base height derived from BERTHA lidar measurements (green circles) during the 22 June 2013 at the west coast near the CIMH.

30 s. This procedure reproduces the clouds visible in Figure 5.21. The spread gives an idea about the cloud thickness due to the fact that if a cloud overpasses the lidar beam, it is very likely that cloud water near the cloud top is detected at first and/or at the end of the overpass. However, in some cases, it indicates some single clouds that start at an altitude of 1600 m. At noon, the cloud base gets higher and the clouds are generally thinner, which can be seen in range of variation in the lidar data, which is very low at this period of time.

5.4 Comparison with Doppler wind lidar data

A further qualitative evaluation of the results obtained by the LES model is carried out by comparing the measurements performed by an airborne Doppler Wind Lidar (DWL), which is presented in this section. Vertical and horizontal wind speed measurements from a flight on 20 June 2013 are compared to the simulation results of the 27 June 2013 case. A simulation with initial data at 20 June 2013 could not have been performed because no nighttime radiosonde data were available at this particular day. Although the measurements and the simulation correspond to different days, the comparison of the radiosonde profiles used for the LES initialization launched on 27 June and the dropsonde measurements obtained during the measurement flight on 20 June show a good agreement in the altitude of the trade inversion, relative humidity levels and temperature profile (Fig. 5.22). Especially the measured horizontal wind speed profile from the dropsondes matches

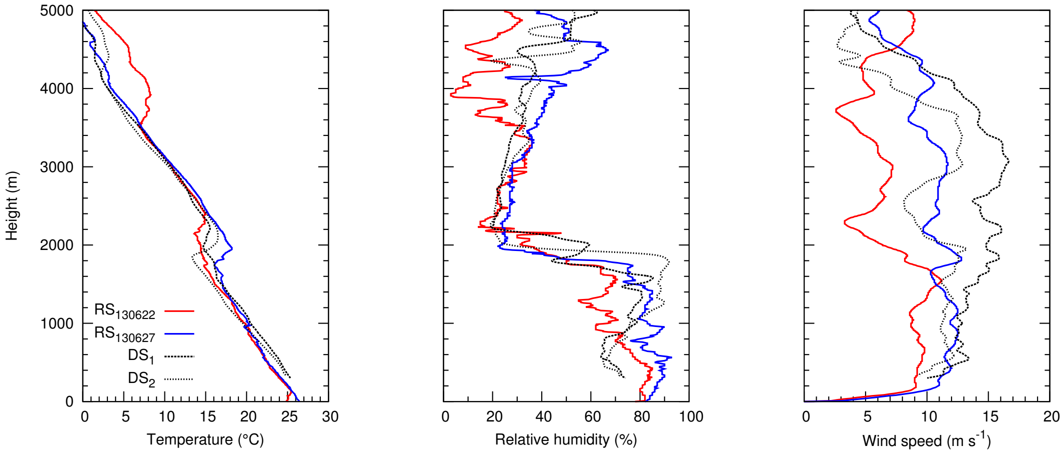

Figure 5.22: Comparison of measured temperature (left panel), relative humidity (middle panel) and wind speed (right panel) obtained from the night-time radiosonde launches (solid lines) on 22 June (red curve) and 27 June (blue curve) and two dropsonde profiles during the wind lidar measurements at 20 June on board the Falcon aircraft. DS$_1$ (dashed lines) was launched 100 km to the west of Barbados at 12:46:59 UTC and DS$_2$ (dotted lines) was launched 200 km to the east of Barbados at 13:22:51 UTC.

better to the 27 June than the 22 June simulation case.

5.4.1 Overview of the performed measurements

The airborne DWL used for this comparison was deployed onboard the DLR Falcon 20 research aircraft during the SALTRACE-1 campaign. The system, based on an instrument developed by Lockheed Martin Coherent Technologies and enhanced by DLR to provide airborne measurement capabilities, can be operated in either nadir pointing mode or scanning mode (Reitebuch, 2012; Chouza et al., 2015). The nadir pointing mode allows the retrieval of vertical wind speeds with a vertical resolution of 100 m and a horizontal resolution of approximately 200 m with a random error lower than 0.15 m s^{-1} and a systematic error lower than 0.05 m s^{-1}. Note that these resolutions are almost identical to the grid spacings used in the LES. On the other side, the scanning mode is used to retrieve horizontal wind speed and direction with a vertical resolution of 100 m and a horizontal resolution of approximately 6 km, depending on the aircraft ground speed. During

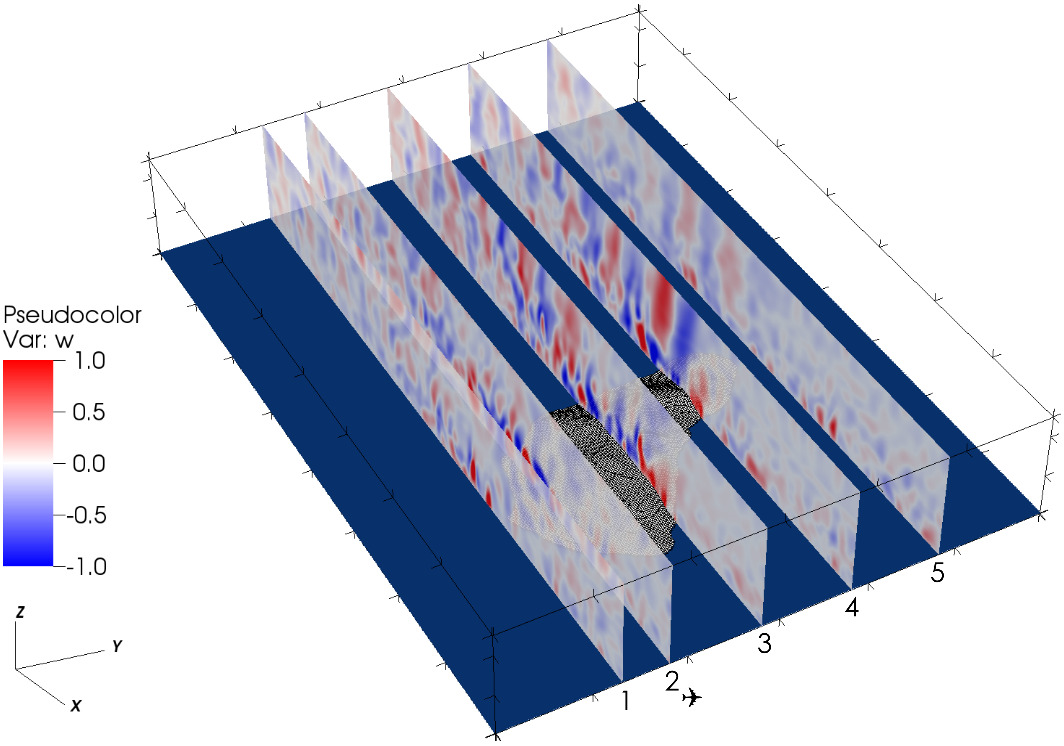

Figure 5.23: Locations of the five considered vertical planes for the comparison between the LES results and the DWL measurements within a domain of 60 km (y) and 80 km (x) up to an altitude of 2.5 km (z). The vertical wind (in m/s) along the planes is indicated in red (updrafts) and blue (downdrafts) colors. Plane 2 is similar to the Falcon flight track. Planes 1 and 5 have no intersection with the island area, which is visualized by surface cut cells of the computational grid. Ocean area is in blue color.

the measurement flight on 20 June 2013, two overflights over Barbados were performed on a very similar flight track, with the DWL operating in a different mode on each overpass. The first overflight was conducted with the lidar operating in scanning mode between 10:00-10:10 LT at a flight altitude of 4400 m, while the lidar was operated in nadir pointing mode during the second overflight between 10:36-10:44 LT at a flight altitude of 2900 m.

Figure 5.23 shows the flight track corresponding to the overflights (plane 2 in the figure) together with the LES results of the vertical wind speed for the 27 June case at 10:30 LT. For the first overflight, the horizontal wind measurements cover almost the whole simulation domain, while for the case of the second overflight, only vertical wind measurements on the lee side and over the island are available.

5.4.2 Horizontal winds

The horizontal wind measurements retrieved on the 20 June 2013 are displayed together with the LES results in Fig. 5.24. As expected, the main easterly flow is well reproduced by the LES. The measurements show a shift in the wind direction from east to southeast for altitudes between 1.5 km and 3 km. This being a large-scale and daytime-dependent effect (it does not show over the whole zonal extent of the plane), it cannot be captured by the LES model. For low level winds on the lee side of Barbados, the model shows an island disturbed flow with southeasterly winds, as it has already been shown in Fig. 5.14 in the previous section. A counter-flow with opposing turn of wind direction with north-easterly winds above 250 m altitude becomes visible both in the LES and the measurement data (Fig. 5.25). However, due to the presence of clouds during the measurement time, only a few measurement points are available from the DWL for altitudes lower than 400 m. Although this few points are compatible with the LES results, the statistical significance is too low to draw a meaningful conclusion from this feature.

5.4.3 Vertical winds

A comparison between the measured and the simulated vertical wind speed profiles is displayed in Fig. 5.26, where some main structures can be recognized in both profiles. Strong vertical winds associated with convective activity over Barbados can be observed on both the simulation and the measurements. It can be noticed that the lidar is able to resolve the vertical velocity structures over the island better than the LES model, which is due to the lower effective model resolution that was already discussed in Section 5.1.4. In the case of the measurements, the presence of convective clouds limits the lidar coverage over the island (between 47 km and 63 km on the x-axis). For the measurements performed on the lee side of Barbados and for altitudes above 1 km a series of waves with a wavelength of approximately 10 km and an amplitude of $2\,\mathrm{m\,s^{-1}}$ can be recognized. A similar feature can be seen in the LES data, but with a slightly weaker amplitude.

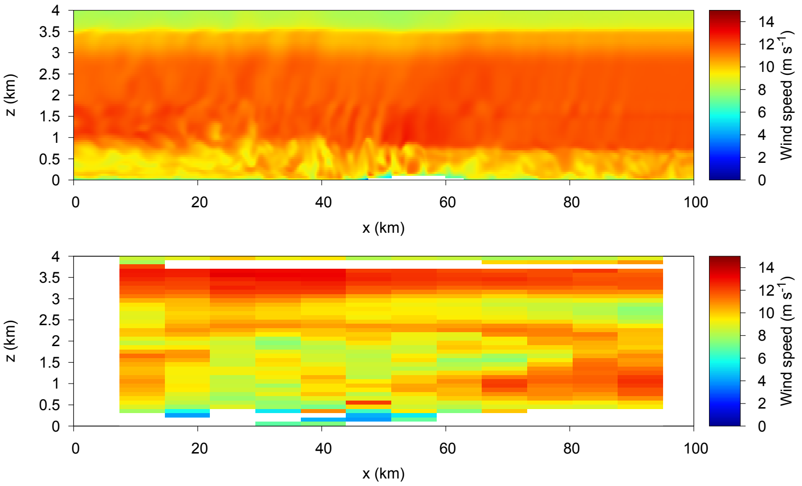

Figure 5.24: LES model output of zonal height-distance profiles of horizontal wind speed at 10:00 LT (upper panel). DWL horizontal wind speed between 10:00-10:10 LT (lower panel). Location is indicated in Fig. 5.23. Island area is between 47 km $< x <$ 63 km.

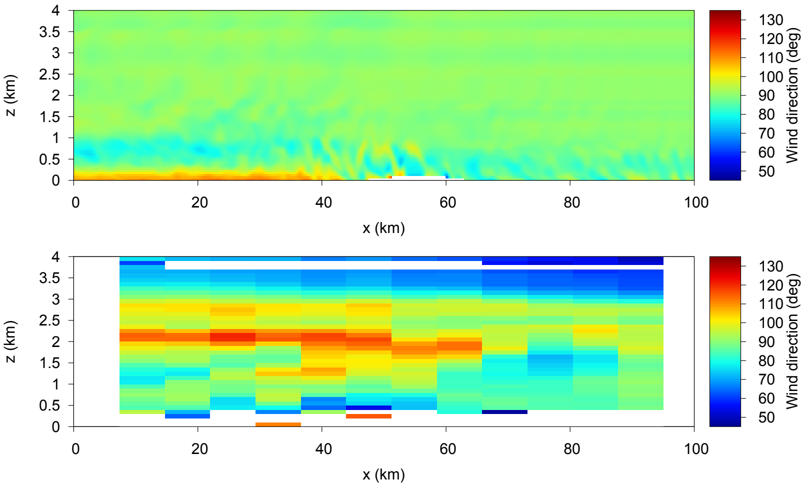

Figure 5.25: Same as Fig. 5.24, but for wind direction.

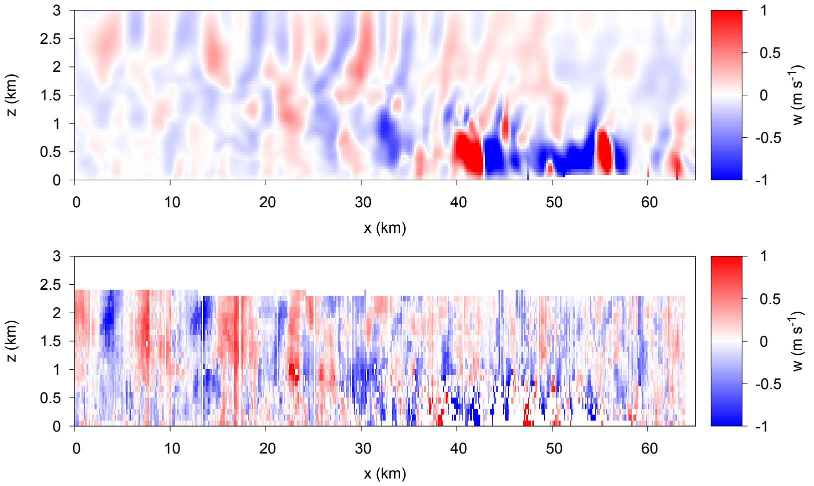

Figure 5.26: LES model output of zonal height-distance profiles of vertical wind speed component (upper panel) at 10:30 LT. DWL vertical wind speed component (lower panel) between 10:36-10:44 LT. Location indicated in Fig. 5.23. Island area is between 47 km $< x <$ 63 km.

To get a better idea of the horizontal distribution of these waves at a certain level, Figure 5.27 shows the vertical wind speed at the trade wind inversion height for different times during the day. It seems that the strength of daytime convective activity plays a minor role since the overall pattern looks very similar in all three snapshots, with the exception of minimally stronger fluctuations toward the afternoon hours. A marked wave structure in the lee of the island is visible, which is the result of trapped gravity waves due to the strong inversion. Again, a similar wavelength amplitude of about 10 km can be seen and also stronger amplitudes (comparable to the DWL measurements) originating from the northern part of Barbados are visible.

Figure 5.28 shows a comparison between the mean and the variance of the measured and simulated vertical wind speed on the lee side (between 0 km and 35 km on the x-axis) of Barbados. The mean vertical wind profiles of the measurements (black line) show a good agreement with the LES results (e.g., cut planes 1, 2 and 5, which are located at the southern and northern edge of Barbados, covering a similar spatial area as in the flight route). The mean vertical velocity below 1 km height indicates a downdraft region on the lee side of Barbados. This can be explained by the daytime circulation pattern in the lee of Barbados since the updraft band located between the center and southern part of the island causes downdrafts at its lateral flanks. Planes 3 and 4 reflect this behavior with positive

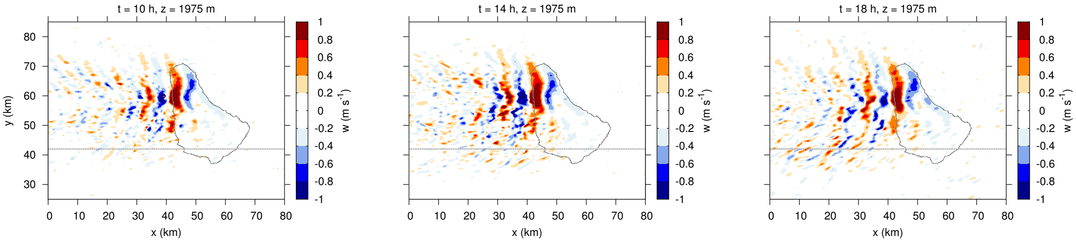

Figure 5.27: LES model output of vertical wind fields around the trade wind inversion height at $z = 1975\,\mathrm{m}$ at 10:00, 14:00 and 18:00 LT on 27 June 2013. The gray dashed line indicates the Falcon flight track (similar to cut plane 2 in Fig. 5.23).

vertical velocities below 1 km height. The variance of the vertical wind field shows an overall increase with altitude both for measurement and model results. However, the strength of these fluctuations is increased in the measurement data, which could result from differences in the forcing, e.g., increased background winds.

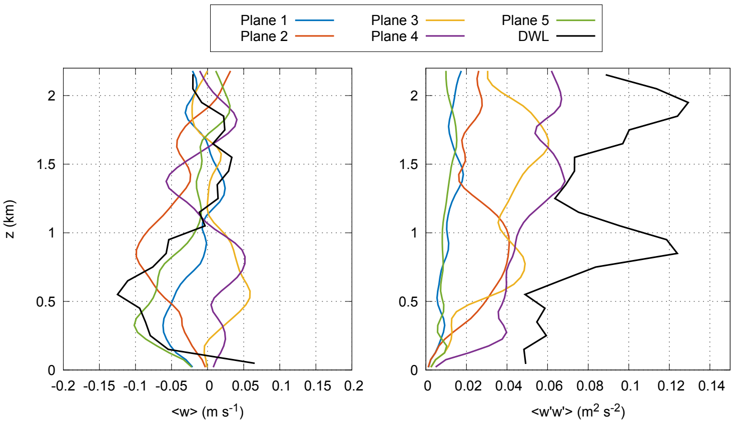

Figure 5.28: Comparison between the mean (left panel) and the variance (right panel) of the measured (black line) and simulated (colored lines) vertical wind fields at the lee side of Barbados at 10:30 LT. The wind profiles are horizontally averaged in *x*-direction along the five different cut planes indicated in Fig. 5.23.

Chapter 6

Summary and conclusions

The fully compressible, three-dimensional, nonhydrostatic atmospheric model ASAM has been enhanced to be utilized for large eddy simulations of island effect studies. The first main focus of this work was a thorough description of the technical aspects of ASAM with close attention being paid to the cut cell method together with the spatial discretization technique. With the cut cell method there is no accuracy loss near steep slopes, which can occur around mountains using a high spatial resolution or when obstacles or buildings are embedded. The concept of the spatial discretization of the advection operator and a non-linear term in the momentum equation were outlined. A technique to distribute surface fluxes around cut cells was described. An implicit Rosenbrock time integration scheme with two splitting approaches of the Jacobian were presented, which is particularly useful to bypass the small cell problem. With the described scheme, relatively large time steps are possible. Physical parameterizations (Smagorinsky subgrid scale model, two-moment warm microphysics scheme, multi-layer soil model), which are necessary for performing large eddy simulations for and island-ocean system, are implemented in ASAM. The model produces good results when comparing scalar and velocity fields for typical benchmark test cases from the literature. It was shown that energy conservation is not affected when it comes to interaction with the flow in the vicinity of cut cells. However, perfect energy conservation can not be expected by design. Accuracy tests show that the experimental order of convergence is almost second order for the annulus advection test. Simulations of atmospheric flow around and idealized, three-dimensional mountain under different ambient conditions showed that gravity-wave structure and precipitation patterns can be well reproduced. Thus, the model ASAM is demonstrably able to simulate atmospheric flow for a wide range of problems.

The second part of this thesis dealt with a LES study for investigating island-induced effects on boundary layer structure, cloud generation and vertical mixing of aerosol layers at the easternmost Caribbean island of Barbados. The simulations were performed with the model ASAM on large eddy scale, where the horizontal resolution of $\Delta x = \Delta y = 200\,\mathrm{m}$ is adequate to still resolve the lower wavenumber end of the inertial subrange of the turbulence spectrum. In order to generate inflow turbulence consistent with the upstream marine boundary layer forcing, the cell perturbation method based on finite amplitude perturbations was used. This method has been successfully adapted to moist boundary layer simulations with open lateral boundary conditions. Spectral analysis and examinations of vertical profiles of boundary layer quantities were used to determine the optimal Eckert number for the simulations. It was found that a value of $Ec = 0.4$ is most suitable for the island simulations, guaranteeing rapid development of turbulence that is very close to results from simulations with periodic boundary conditions. This perturbation Eckert number differs from the optimum $Ec = 0.2$ derived for neutral stability (Muñoz-Esparza et al., 2015). These weaker-amplitude temperature perturbations appear to be due to a combination of the use of open boundary conditions and near production range grid resolution.

After the model was set up, several simulations were performed to analyze island effects. The atmospheric state is described by a horizontally homogeneous profile obtained via nighttime radiosonde launches. On the one hand, the used profile can not be seen as a representative state, which could have been achieved by averaging multiple profiles. One the other hand, these quasi-idealized simulations enabled the possibility to compare the LES output data with Raman lidar and DWL measurements. Large-scale forcings are not applied during the simulation time, i.e., a time-invariant background state is used, which makes it easier to analyze daytime changes in boundary layer and cloud characteristics as a result of convective island activity. The radiosonde profile from 22 June 2013 served as reference case for a crucial sensitivity study, which revealed the following:

- Due to the daytime island heating, the moderate trade wind flow and undisturbed background conditions, the conceptual model of island effects is affirmed and visible in the LES model data. Island convection leads to downwind flow distortion, which results in a near-surface flow convergence together with a well-defined updraft band of at least 40 km length that is aligned along the mean wind direction in the downwind region of Barbados.

- Disadvantages of neglecting a turbulent inflow and modeling within the 'terra incognita' or 'gray zone' become apparent (Wyngaard, 2004). If the turbulent inflow generation is turned off, i.e., no marine boundary layer develops, cloud properties are drastically changed over and in the lee of the island. There, cloud cover, liquid water path and cloud base height have significantly higher values compared to the reference case. Also, the cloud morphology is different, having horizontally aligned cloud bands instead of scattered cumulus clouds.

- Using a general coarser horizontal grid spacing of $\Delta x = \Delta y = 400\,\mathrm{m}$ shows the same issues regarding cloud properties. Additionally, boundary layer turbulence is not well resolved but vertical energy transport is enhanced overall, which leads to the formation of a cloud street along the updraft band past Barbados. This has not been seen in the other cases and can thus be considered as an artificial effect.

- If island orography is not taken into account, the downwind flow convergence pattern is still present. However, there is a weaker flow acceleration and the flow field is less turbulent due to a flat island surface and the absence of orographic turbulence. This has also subsequent effects on the spatial distribution of island-induced shallow cumulus clouds, which are more concentrated in the southern part of Barbados.

- Effects of weaker surface sensible heat fluxes, which can occur due to radiation absorption or reflection at upper levels, are less fluctuations in the vertical wind, a lowering of the mean boundary layer height of about 150 m and a reduction in cloud cover and LWP by 40-50 %.

- Analyzing the daytime convective boundary layer for both considered cases (22 June and 27 June 2013), they both generally show similar vertical profiles, although slight differences were detected due to wind shear effects in particular. Also, for the case with the strong trade inversion, the boundary layer grew approximately 150 m deeper. Significant differences were again visible in cloud properties. In the latter case, the trade inversion inhibited cloud growth beyond 1800 m altitude, whereas local overshoots through the weaker inversion occurred in the 22 June case.

Vertical mixing of aerosols and layer transport has been qualitatively and quantitatively analyzed by including passive tracers in the LES model, which represent the incoming Saharan dust layers over Barbados. They are initialized at the same heights as they are seen in Raman lidar data during the considered days. The model data suggested that a continuous subsidence velocity within these layers was present, which lead to a mean descent of 400 m toward the surface. Layers of turbulent downward mixing have also been detected between 1200 m and 1700 m altitude. It can be concluded that if the dust layer reaches this height range, turbulent downward mixing of aerosol takes place, which is separated from large-scale subsidence effects. The exact position of these layers and strength of downward mixing and transport are mainly controlled by atmospheric stability and wind shear. It became apparent that for the INV case the net vertical transport is rather upwards for heights around the Saharan dust layer base. A larger number of simulation cases would provide further insight of this effect and the influence of trade inversion strength.

Qualitative comparisons with Raman lidar and DWL measurements were carried out to validate the LES model results. From the stationary Raman Lidar BERTHA, which was deployed near the west coast of Barbados, cloud base heights and thickness were estimated and compared with the LES data. Combining these two techniques, a consistent picture of the diurnal convective activity and cloud generation over the island was gained for the most part. Considering the comparison with DWL data, a lot of similarities were found despite comparing different days, which however were very similar in terms of atmospheric stability, mean wind and temperature profile. First of all, large-scale changes in dynamics occur, which expectedly can not directly be captured by the model. However, island-induced lee side flow distortion is well resolved by the model, whereas the presence of clouds made it difficult to resolve this effect with the DWL horizontal wind measurements in addition to the coarser resolution of 6 km. Furthermore, the vertical wind field shows a similar structure for both measurements and LES, highlighting the convective activity over the island and trapped gravity waves around the strong trade inversion. The amplitude of these waves was a bit higher in the measurements, which is also seen in the vertical wind variance profile. Taking these comparison results into account and connecting them to the boundary layer and tracer analysis, it is possible that turbulent (downward) mixing of aerosol layers could be even more enhanced than the LES model results suggest.

As a general conclusion of this work, the performed simulations provided a detailed image of downwind boundary layer structure, cloud and vertical mixing processes, which agree well with lidar measurements. The model data can also help to better interpret the ground-based observations gained during the SALTRACE campaign at the Barbados west coast (CIMH field site).

Possible future model development could focus on cloud-radiative feedback (closely linked with heating rates at different levels) and shadowing effects (leading to a reduction of surface fluxes). Furthermore, finer horizontal grid spacings than 200 m would be desirable to either confirm the robustness of the obtained results or reveal additional effects of finer resolved turbulent structures. However, this requires a high computational effort, especially when performing sensitivity tests with a high number of simulations. In this context, performance tests for highly parallel computing with a large number of processors could be conducted to find out how well the scaling with an increased amount of processor units is maintained. A high-frequency "on the fly"-output is desired for statistical data analysis for computationally expensive large eddy simulations. For this reason, efficient techniques like adaption of the output on modern parallel visualization software will be an important priority for upcoming applications. Another focus on future model development lies on the model physics, which includes further testing of current implementations as well as adding new parameterizations, e.g., an ice microphysics scheme. For the description of turbulence, other (dynamic) Smagorinsky models (e.g., Kleissl et al., 2006; Porté-Agel et al., 2000) might be better suited for particular simulations compared to the present model version.

ASAM continues to be utilized for large eddy simulations of different boundary layer types (urban, marine, convective, canopy or arctic BL etc.). It is possible to use ASAM as an application-oriented tool for several kinds of problems, e.g., urban heat islands on a building-resolved scale, effects of land-use and terrain heterogeneity or as a concurrent LES model during field campaigns.

Appendix A

Derivation of tendency equations

In this appendix chapter a straightforward derivation of the density potential temperature tendency equation is given to get the necessary source terms for microphysics, surface fluxes and precipitation. Therefore, phase changes are allowed and a water vapor source term S_v and sedimentation velocity W_f for rain drops are added to the system.

$$\frac{d\rho}{dt} = -\rho\nabla \cdot \vec{v} + S_v - S_{fall}\,, \tag{A.1}$$

$$\frac{d\rho_v}{dt} = -\rho_v\nabla \cdot \vec{v} + S_v + S_{ph}\,, \tag{A.2}$$

$$\frac{d\rho_l}{dt} = -\rho_c\nabla \cdot \vec{v} - S_{ph} - S_{fall}\,, \tag{A.3}$$

$$\frac{d\rho_d}{dt} = -\rho_d\nabla \cdot \vec{v}\,. \tag{A.4}$$

The precipitation term is $S_{fall} = \partial/\partial z(\rho_r W_f)$ with the sedimentation velocity W_f after Eq. (2.57). The source terms are in units of $\mathrm{kg\,m^{-3}\,s^{-1}}$. One can rewrite the equations (A.2) and (A.3) with the mixing ratios $r_v = \rho_v/\rho_d$ and $r_l = \rho_l/\rho_d$:

$$\frac{dr_v}{dt} = \frac{1}{\rho_d}(S_v + S_{ph})\,, \tag{A.5}$$

$$\frac{dr_l}{dt} = -\frac{1}{\rho_d}(S_{ph} + S_{fall})\,. \tag{A.6}$$

For the sake of simplicity (regarding the following derivations) the liquid water density and mixing ratio are used with $\rho_l = \rho_c + \rho_r$ or $r_l = r_c + r_r$. The model however solves the prognostic equations for the cloud water density ρ_c and rain water density ρ_r separately.

A.1 Internal energy and absolute temperature

A prognostic equation for the internal energy e is derived from the first law of thermodynamics, cf. Bott (2008, Eq. (31)) and Satoh et al. (2008, Eq. (B.13)):

$$\frac{\partial(\rho e)}{\partial t} + \nabla \cdot (\rho e \vec{v}) = -p \nabla \cdot \vec{v} + S_e - \frac{\partial}{\partial z}(\rho_r W_f e_l) - \rho_r W_f g \,, \tag{A.7}$$

and alternatively with the specific enthalpy h in the advection part:

$$\frac{\partial(\rho e)}{\partial t} + \nabla \cdot (\rho h \vec{v}) = \vec{v} \cdot \nabla p + S_e - \frac{\partial}{\partial z}(\rho_r W_f e_l) - \rho_r W_f g \,. \tag{A.8}$$

There, the total specific internal energy is

$$e = h - \frac{p}{\rho} = (q_d c_{vd} + q_v c_{vv} + q_l c_{pl}) T + q_v L_{00} \,, \tag{A.9}$$

and the specific internal energy for liquid water

$$e_l = h_l = c_{pl} T \,. \tag{A.10}$$

The term S_e is related to the water vapor source term S_v:

$$S_e = h_v S_v \,. \tag{A.11}$$

Transforming Eq. (A.7) into a tendency equation for the absolute temperature:

$$\begin{aligned} e\left(\frac{\partial \rho}{\partial t} + \nabla \cdot (\rho \vec{v})\right) + \rho\left(\frac{\partial e}{\partial t} + \vec{v} \cdot \nabla e\right) &= \mathrm{RHS(A.7)} \\ e(S_v - S_{fall}) + \rho \frac{de}{dt} &= \mathrm{RHS(A.7)} \\ e(S_v - S_{fall}) + \frac{d(\rho e)}{dt} - e\frac{d\rho}{dt} &= \mathrm{RHS(A.7)} \end{aligned} \tag{A.12}$$

With Eq. (A.9), this leads to

$$\begin{aligned}
\frac{d(\rho e)}{dt} =& \frac{d}{dt}\left([\rho_d c_{vd} + \rho_v c_{vv} + \rho_l c_{pl}]T + \rho_v L_{00}\right) \\
=& T\left(c_{vd}\frac{d\rho_d}{dt} + c_{vv}\frac{d\rho_v}{dt} + c_{pl}\frac{d\rho_l}{dt}\right) \\
&+ (\rho_d c_{vd} + \rho_v c_{vv} + \rho_l c_{pl})\frac{dT}{dt} + L_{00}\frac{d\rho_v}{dt} \\
&- (\rho_d c_{vd} + \rho_v c_{vv} + \rho_l c_{pl})T\nabla\cdot\vec{v} \\
&+ T c_{vv}(S_v + S_{ph}) - T c_{pl}(S_{ph} + S_{fall}) \\
&+ (\rho_d c_{vd} + \rho_v c_{vv} + \rho_l c_{pl})\frac{dT}{dt} \\
&- L_{00}(\rho_v\nabla\cdot\vec{v} - S_v - S_{ph}) \\
=& - e\rho\nabla\cdot\vec{v} + (\rho_d c_{vd} + \rho_v c_{vv} + \rho_l c_{pl})\frac{dT}{dt} \\
&+ T(c_{vv}[S_v + S_{ph}] - c_{pl}[S_{ph} + S_{fall}]) \\
&+ L_{00}(S_v + S_{ph})\,, \qquad \text{(A.13)} \\
e\frac{d\rho}{dt} =& e(S_v - S_{fall}) - e\rho\nabla\cdot\vec{v}\,. \qquad \text{(A.14)}
\end{aligned}$$

Inserting Eq. (A.13) and (A.14) in (A.12):

$$\begin{aligned}
\rho_d c_{vml}\frac{dT}{dt} =& - T(c_{vv}[S_v + S_{ph}] - c_{pl}[S_{ph} + S_{fall}]) \\
&- L_{00}(S_v + S_{ph}) - p\nabla\cdot\vec{v} + S_v h_v \\
&- \frac{\partial}{\partial z}(\rho_r W_f e_l) - \rho_r W_f g \\
=& - p\nabla\cdot\vec{v} + (h_v - c_{vv}T - L_{00})S_v \\
&+ (c_{pl}T - c_{vv}T - L_{00})S_{ph} \\
&- \frac{\partial}{\partial z}(\rho_r W_f e_l) - \rho_r W_f g\,. \qquad \text{(A.15)}
\end{aligned}$$

Here we define

$$c_{vml} \equiv c_{vd} + r_v c_{vv} + r_l c_{pl}\,. \qquad \text{(A.16)}$$

Rewriting the pressure and elimination of the velocity divergence:

$$\begin{aligned}
-p\nabla\cdot\vec{v} =& -(\rho_d R_d + \rho_v R_v)T\left(-\frac{1}{\rho_d}\frac{d\rho_d}{dt}\right)\\
=&(R_d + r_v R_v)T\frac{d\rho_d}{dt}\,, && \text{(A.17)}\\
\frac{d\rho_d}{dt} =& \frac{1}{R_d T\left(1+\frac{r_v}{\varepsilon}\right)}\frac{dp}{dt} - \frac{pR_dT}{\varepsilon\left(R_dT\left[1+\frac{r_v}{\varepsilon}\right]\right)^2}\frac{dr_v}{dt}\\
&-\frac{p}{R_dT^2\left(1+\frac{r_v}{\varepsilon}\right)}\frac{dT}{dt}\\
=&\frac{\rho_d}{p}\frac{dp}{dt} - \frac{\rho_d}{\varepsilon + r_v}\frac{dr_v}{dt} - \frac{\rho_d}{T}\frac{dT}{dt} && \text{(A.18)}\\
\Rightarrow -p\nabla\cdot\vec{v} =& \frac{dp}{dt} - \rho_d R_v T\frac{dr_v}{dt} - (\rho_d R_d + \rho_v R_v)\frac{dT}{dt}\\
=&\frac{dp}{dt} - R_v T(S_v + S_{ph}) - (\rho_d R_d + \rho_v R_v)\frac{dT}{dt}\,. && \text{(A.19)}
\end{aligned}$$

Now this leads to the temperature equation:

$$\begin{aligned}
\rho_d(c_{vml} + R_m)\frac{dT}{dt} =& \rho_d c_{pml}\frac{dT}{dt}\\
=&\frac{dp}{dt} - R_v T(S_v + S_{ph})\\
&+ (h_v - c_{vv}T - L_{00})S_v\\
&+ (c_{pl}T - c_{vv}T - L_{00})S_{ph}\\
&- \frac{\partial}{\partial z}(\rho_r W_f e_l) - \rho_r W_f g\,, && \text{(A.20)}
\end{aligned}$$

With $c_{pv} - c_{vv} = R_v$, the water vapor source term disappears:

$$\begin{aligned}
&(h_v - c_{vv}T - L_{00} - R_v T)S_v =\\
&= (c_{pv}T + L_{00} - c_{vv}T - L_{00} - R_v T)S_v = 0\,. && \text{(A.21)}
\end{aligned}$$

Further simplifying:

$$\begin{aligned}
&(c_{pl}T - c_{vv}T - R_vT - L_{00})S_{ph} =\\
&(c_{pl}T - c_{vv}T - R_vT - L_v + (c_{pv} - c_{pl})T)S_{ph} =\\
&= -L_v S_{ph}\,. && \text{(A.22)}
\end{aligned}$$

Rearranging finally leads to the temperature equation

$$\rho_d c_{pml}\frac{dT}{dt} = \frac{dp}{dt} - L_v S_{ph} - \frac{\partial}{\partial z}(\rho_r W_f e_l) - \rho_r W_f g\,. \qquad \text{(A.23)}$$

and its logarithmic derivative

$$\begin{aligned}\frac{d\ln T}{dt} =& \frac{R_m}{c_{pml}}\frac{d\ln p}{dt} - \frac{L_v}{\rho_d c_{pml} T} S_{ph} \\ & - \frac{1}{\rho_d c_{pml} T}\frac{\partial}{\partial z}(\rho_r W_f e_l) - \frac{\rho_r W_f g}{\rho_d c_{pml} T} \, . \end{aligned} \tag{A.24}$$

A.2 Potential temperature

A prognostic equation for the (moist) potential temperature is derived here. This is necessary because it appears in the density potential temperature equation later on. Quantities that contain water vapor and liquid water are marked with a tilde to distinguish them from their dry equivalents (e.g., dry potential temperature θ).

The moist potential temperature is

$$\tilde{\theta} = \frac{T}{\tilde{\pi}} \qquad \text{mit} \qquad \tilde{\pi} = \left(\frac{p}{p_0}\right)^{\frac{R_m}{c_{pml}}} \, . \tag{A.25}$$

Taking the logarithm of the Exner function $\tilde{\pi}$ leads to

$$\ln \tilde{\pi} = \frac{R_m}{c_{pml}} \ln\left(\frac{p}{p_0}\right) \, . \tag{A.26}$$

The time derivative of the Exner function is

$$\begin{aligned}\frac{d\ln\tilde{\pi}}{dt} =& \frac{R_v}{R_m}\ln\tilde{\pi}\frac{dr_v}{dt} \\ & - \frac{\ln\tilde{\pi}}{c_{pml}}\left(c_{pv}\frac{dr_v}{dt} + c_{pl}\frac{dr_l}{dt}\right) + \frac{R_m}{c_{pml}}\frac{d\ln p}{dt} \, . \end{aligned} \tag{A.27}$$

Replacing the mixing ratio tendencies leads to

$$
\begin{aligned}
\frac{d\ln\tilde{\pi}}{dt} =& \frac{R_v}{R_m}\ln\tilde{\pi}\frac{S_v+S_{ph}}{\rho_d} \\
& -\ln\tilde{\pi}\left(\frac{c_{pv}}{c_{pml}}\frac{S_v+S_{ph}}{\rho_d}-\frac{c_{pl}}{c_{pml}}\frac{S_{ph}+S_{fall}}{\rho_d}\right) \\
& +\frac{R_m}{c_{pml}}\frac{d\ln p}{dt} \\
=& \ln\tilde{\pi}\left(\left[\frac{R_v}{R_m}-\frac{c_{pv}}{c_{pml}}\right]\frac{S_v+S_{ph}}{\rho_d}+\frac{c_{pl}}{c_{pml}}\frac{S_{ph}+S_{fall}}{\rho_d}\right) \\
& +\frac{R_m}{c_{pml}}\frac{d\ln p}{dt} \\
=& \frac{\ln\tilde{\pi}}{\rho_d}\left(\frac{R_v}{R_m}-\frac{c_{pv}}{c_{pml}}\right)S_v \\
& +\frac{\ln\tilde{\pi}}{\rho_d}\left(\frac{R_v}{R_m}+\frac{c_{pl}-c_{pv}}{c_{pml}}\right)S_{ph} \\
& +\frac{\ln\tilde{\pi}}{\rho_d}\frac{c_{pl}}{c_{pml}}S_{fall}+\frac{R_m}{c_{pml}}\frac{d\ln p}{dt}\,,
\end{aligned}
\tag{A.28}
$$

which leads to the moist potential temperature equation:

$$
\begin{aligned}
\frac{d\ln\tilde{\theta}}{dt} =& \frac{d\ln T}{dt}-\frac{d\ln\tilde{\pi}}{dt} \\
=& \frac{R_m}{c_{pml}}\frac{d\ln p}{dt}-\frac{L_v}{\rho_d c_{pml}T}S_{ph}-\frac{1}{\rho_d c_{pml}T}\frac{\partial}{\partial z}(\rho_r W_f e_l) \\
& -\frac{\rho_r W_f g}{\rho_d c_{pml}T}-\frac{\ln\tilde{\pi}}{\rho_d}\left(\frac{R_v}{R_m}-\frac{c_{pv}}{c_{pml}}\right)S_v \\
& -\frac{\ln\tilde{\pi}}{\rho_d}\left(\frac{R_v}{R_m}+\frac{c_{pl}-c_{pv}}{c_{pml}}\right)S_{ph} \\
& -\frac{\ln\tilde{\pi}}{\rho_d}\frac{c_{pl}}{c_{pml}}S_{fall}-\frac{R_m}{c_{pml}}\frac{d\ln p}{dt} \\
=& -\frac{\ln\tilde{\pi}}{\rho_d}\left(\frac{R_v}{R_m}-\frac{c_{pv}}{c_{pml}}\right)S_v \\
& -\frac{1}{\rho_d}\left(\frac{L_v}{c_{pml}T}+\ln\tilde{\pi}\left[\frac{R_v}{R_m}+\frac{c_{pl}-c_{pv}}{c_{pml}}\right]\right)S_{ph} \\
& -\frac{\ln\tilde{\pi}}{\rho_d}\frac{c_{pl}}{c_{pml}}S_{fall} \\
& -\frac{1}{\rho_d c_{pml}T}\frac{\partial}{\partial z}(\rho_r W_f e_l)-\frac{\rho_r W_f g}{\rho_d c_{pml}T}\,.
\end{aligned}
\tag{A.29}
$$

A.3 Density potential temperature

With the definition of the density potential temperature

$$\theta_\rho = \tilde{\theta}\frac{1 + r_v/\epsilon}{1 + r_v + r_l} \tag{A.30}$$

and by using the product rule:

$$\begin{aligned}
\frac{d\theta_\rho}{dt} =& \frac{1 + r_v/\epsilon}{1 + r_v + r_l}\frac{d\tilde{\theta}}{dt} + \frac{\tilde{\theta}}{1 + r_v + r_l}\frac{1}{\epsilon}\frac{dr_v}{dt} \\
& - \tilde{\theta}\frac{1 + r_v/\epsilon}{(1 + r_v + r_l)^2}\left(\frac{dr_v}{dt} + \frac{dr_l}{dt}\right) \\
=& \frac{\theta_\rho}{\tilde{\theta}}\frac{d\tilde{\theta}}{dt} + \theta_\rho\left(\frac{1}{\varepsilon + r_v} - \frac{1}{1 + r_v + r_l}\right)\frac{dr_v}{dt} \\
& - \frac{\theta_\rho}{1 + r_v + r_l}\frac{dr_l}{dt}\,.
\end{aligned} \tag{A.31}$$

Inserting Eqs. (A.29), (A.5) and (A.6) in (A.31):

$$\begin{aligned}
\frac{d\ln\theta_\rho}{dt} =& \frac{d\ln\tilde{\theta}}{dt} + \left(\frac{1}{\varepsilon + r_v} - \frac{1}{1 + r_v + r_l}\right)\frac{dr_v}{dt} \\
& - \frac{1}{1 + r_v + r_l}\frac{dr_l}{dt} \\
=& - \frac{\ln\tilde{\pi}}{\rho_d}\left(\frac{R_v}{R_m} - \frac{c_{pv}}{c_{pml}}\right)S_v \\
& - \frac{1}{\rho_d}\left(\frac{L_v}{c_{pml}T} + \ln\tilde{\pi}\left[\frac{R_v}{R_m} + \frac{c_{pl} - c_{pv}}{c_{pml}}\right]\right)S_{ph} \\
& - \frac{\ln\tilde{\pi}}{\rho_d}\frac{c_{pl}}{c_{pml}}S_{fall} \\
& - \frac{1}{\rho_d c_{pml}T}\frac{\partial}{\partial z}(\rho_r W_f e_l) - \frac{\rho_r W_f g}{\rho_d c_{pml}T} \\
& + \left(\frac{1}{\varepsilon + r_v} - \frac{1}{1 + r_v + r_l}\right)\frac{S_v + S_{ph}}{\rho_d} \\
& + \frac{1}{1 + r_v + r_l}\frac{S_{ph} + S_{fall}}{\rho_d}\,.
\end{aligned} \tag{A.32}$$

With the relation

$$\frac{1}{\varepsilon + r_v} = \frac{1}{\frac{R_d}{R_v} + r_v} = \frac{R_v}{R_d + r_v R_v} = \frac{R_v}{R_m} \tag{A.33}$$

we get the density potential temperature equation sort by source terms:

$$
\begin{aligned}
\frac{d\theta_\rho}{dt} = &\frac{\theta_\rho}{\rho_d}\left(\frac{R_v}{R_m} - \frac{\rho_d}{\rho} - \ln\tilde{\pi}\left[\frac{R_v}{R_m} - \frac{c_{pv}}{c_{pml}}\right]\right) S_v \\
&+ \frac{\theta_\rho}{\rho_d}\left(\frac{R_v}{R_m} - \ln\tilde{\pi}\left[\frac{R_v}{R_m} + \frac{c_{pl} - c_{pv}}{c_{pml}}\right] - \frac{L_v}{c_{pml}T}\right) S_{ph} \\
&+ \frac{\theta_\rho}{\rho_d}\left(\frac{\rho_d}{\rho} - \frac{c_{pl}}{c_{pml}}\ln\tilde{\pi}\right) S_{fall} \\
&- \frac{\theta_\rho}{\rho_d c_{pml} T}\left(\frac{\partial}{\partial z}(\rho_r W_f e_l) + \rho_r W_f g\right) \, . \qquad \text{(A.34)}
\end{aligned}
$$

Appendix B

Vertical profiles of the SALTRACE simulations

Due to the large amount of evaluated data of the SALTRACE simulations, additional temporally and spatially averaged profiles for the six simulation cases (REF, INV, NOCP, DX400, FLAT, FLUX) are shown in this appendix chapter. Most important profiles that are important for the boundary layer and cloud analysis (namely LWC, resolved TKE as well as sensible and latent heat flux) are already shown in Fig. 5.16 in Section 5.2.2. The panels in Fig. B.1–B.2 show the averaged profiles of density potential temperature $\langle \theta_\rho \rangle$, specific cloud water content $\langle q_c \rangle$, specific humidity $\langle q_v \rangle$, zonal and meridional wind speed components $\langle u \rangle$ and $\langle v \rangle$, vertical wind $\langle u \rangle$, turbulent fluxes of zonal $\langle u'w' \rangle$, meridional $\langle v'w' \rangle$ and vertical wind component $\langle w'w' \rangle$. Some additional orographic effects like a negative meridional component of the momentum flux and a net mean downdraft vertical velocity $> 0.1\,\mathrm{m\,s^{-1}}$ become apparent for the FLAT case. The profiles of the velocity components are most dependent on island shape and the topographical situation because even in the FLUX case with less surface sensible heat flux the profiles are nearly identical to REF. The momentum flux, however, is reduced by approx. 20 % for the horizontal components and almost 50 % for the vertical component. The INV case mainly differs in the vertical structure of the wind components. While this is expected for the u and v components by design, the mean vertical wind is getting positive for $z > 1000\,\mathrm{m}$, where as in REF this is the case for $z > 1700\,\mathrm{m}$. Again, the dynamical forcing, especially wind shear, appears to be very important for controlling up- and downdraft regimes downwind Barbados.

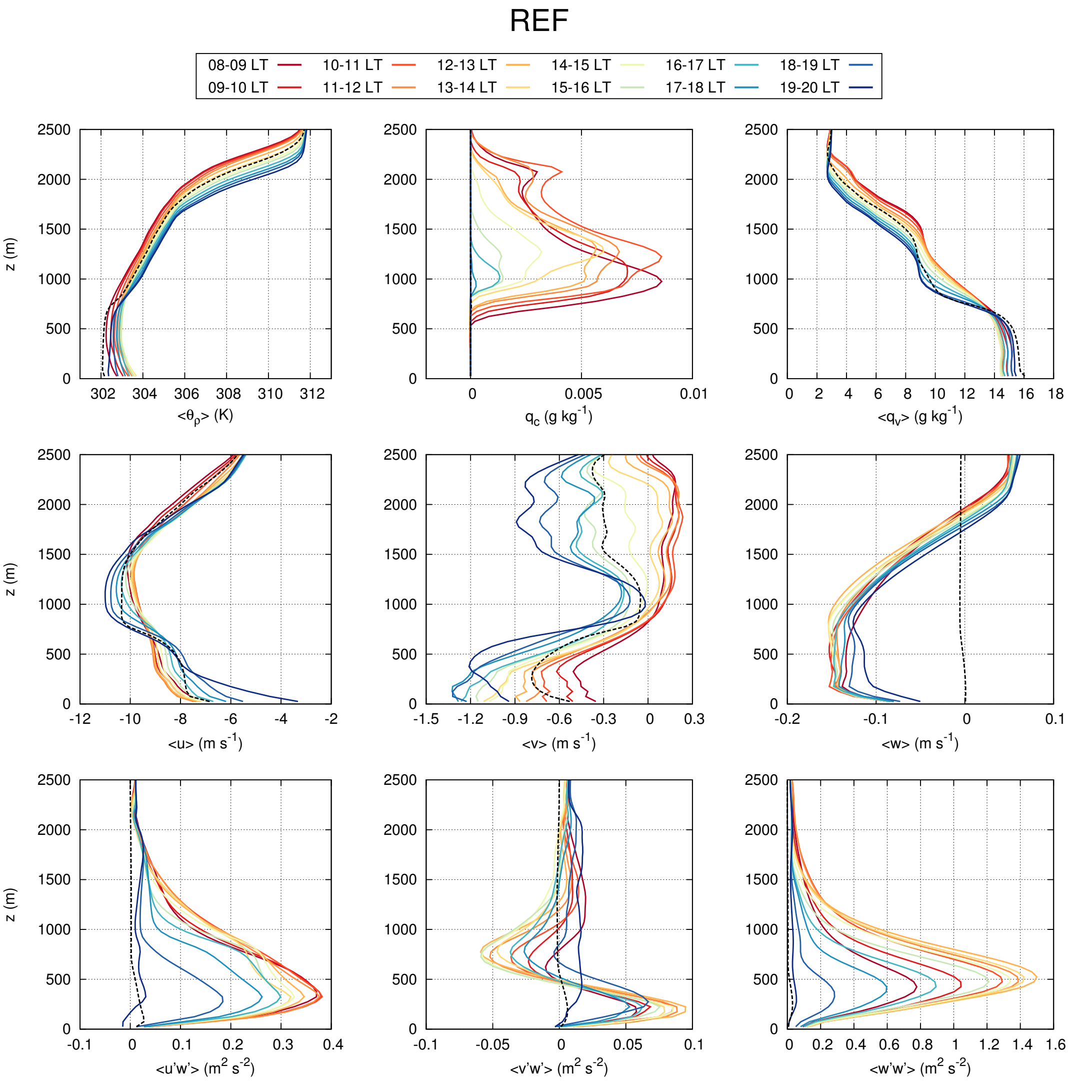

Figure B.1: Vertical profiles of density potential temperature $\langle \theta_\rho \rangle$, specific cloud water content $\langle q_c \rangle$, specific humidity $\langle q_v \rangle$, zonal and meridional wind speed components $\langle u \rangle$ and $\langle v \rangle$, vertical wind $\langle u \rangle$, turbulent fluxes of zonal $\langle u'w' \rangle$, meridional $\langle v'w' \rangle$ and vertical wind component $\langle w'w' \rangle$ for the REF case, from top to bottom. Spatial averaging as indicated in Fig. 5.8. Black dashed lines represent the marine upwind area and are temporally averaged between 08:00 and 20:00 LT. Colored solid lines stand for hourly averages during different times of the day for the downwind area.

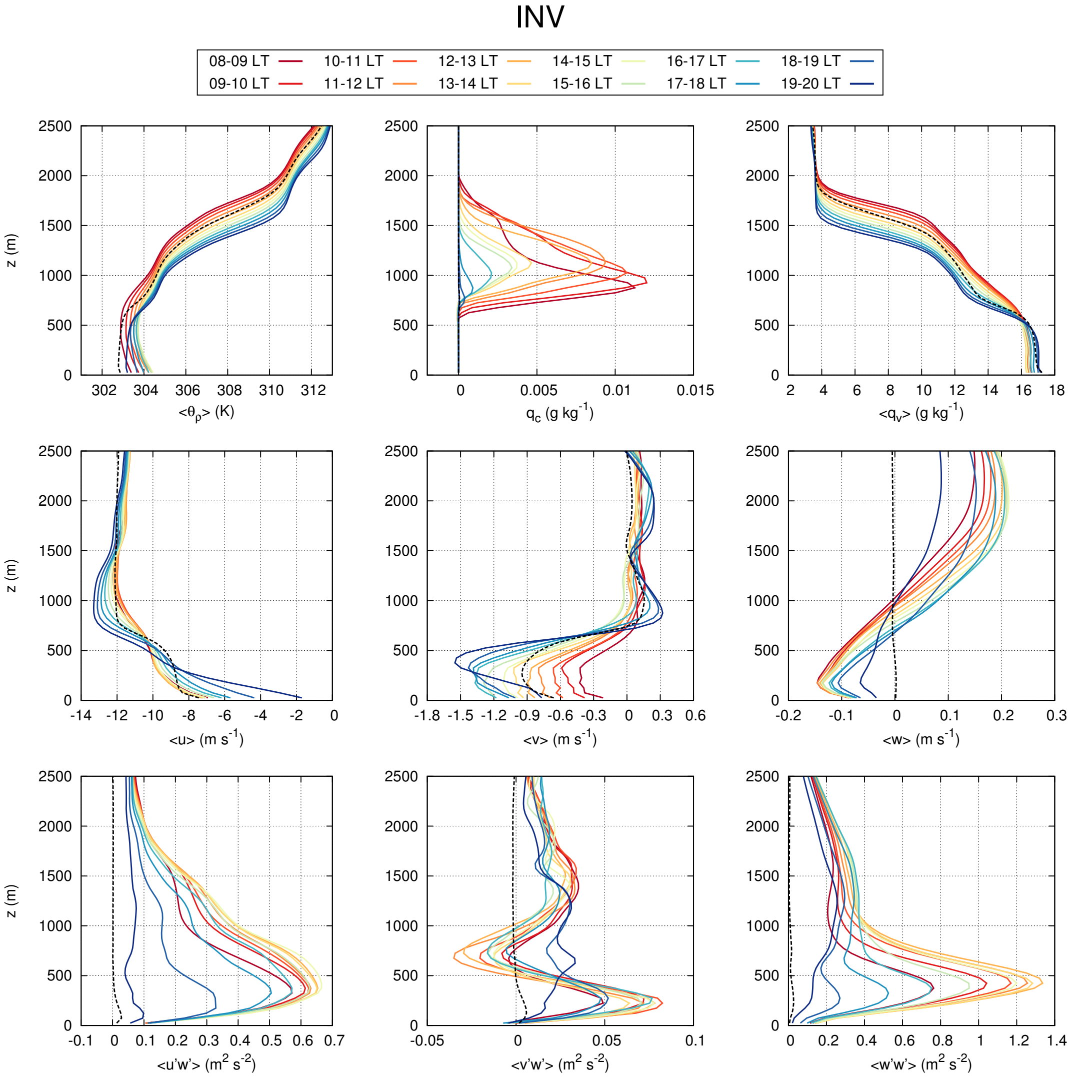

Figure B.2: Same as Fig. B.1, but for the INV case.

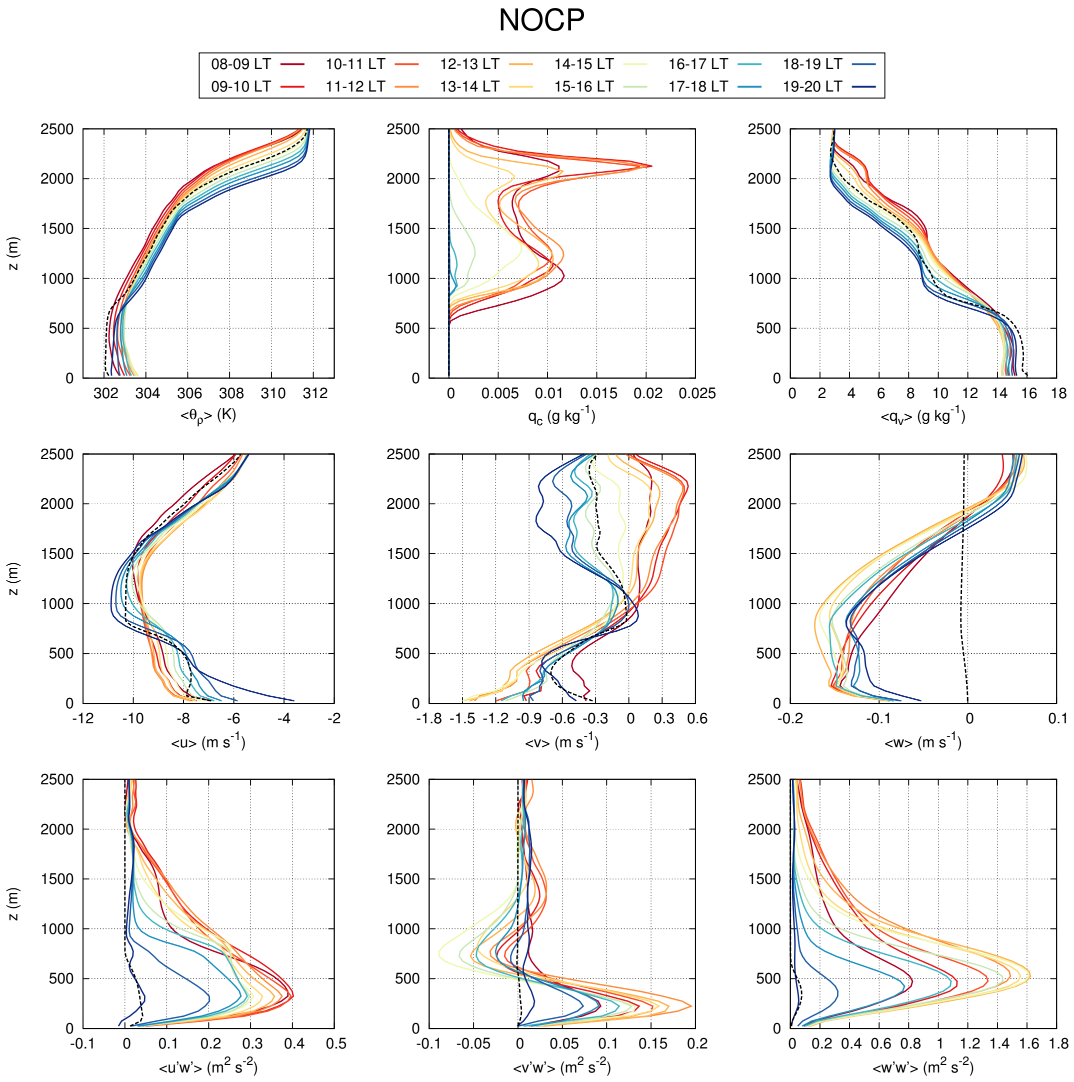

Figure B.3: Same as Fig. B.1, but for the NOCP case.

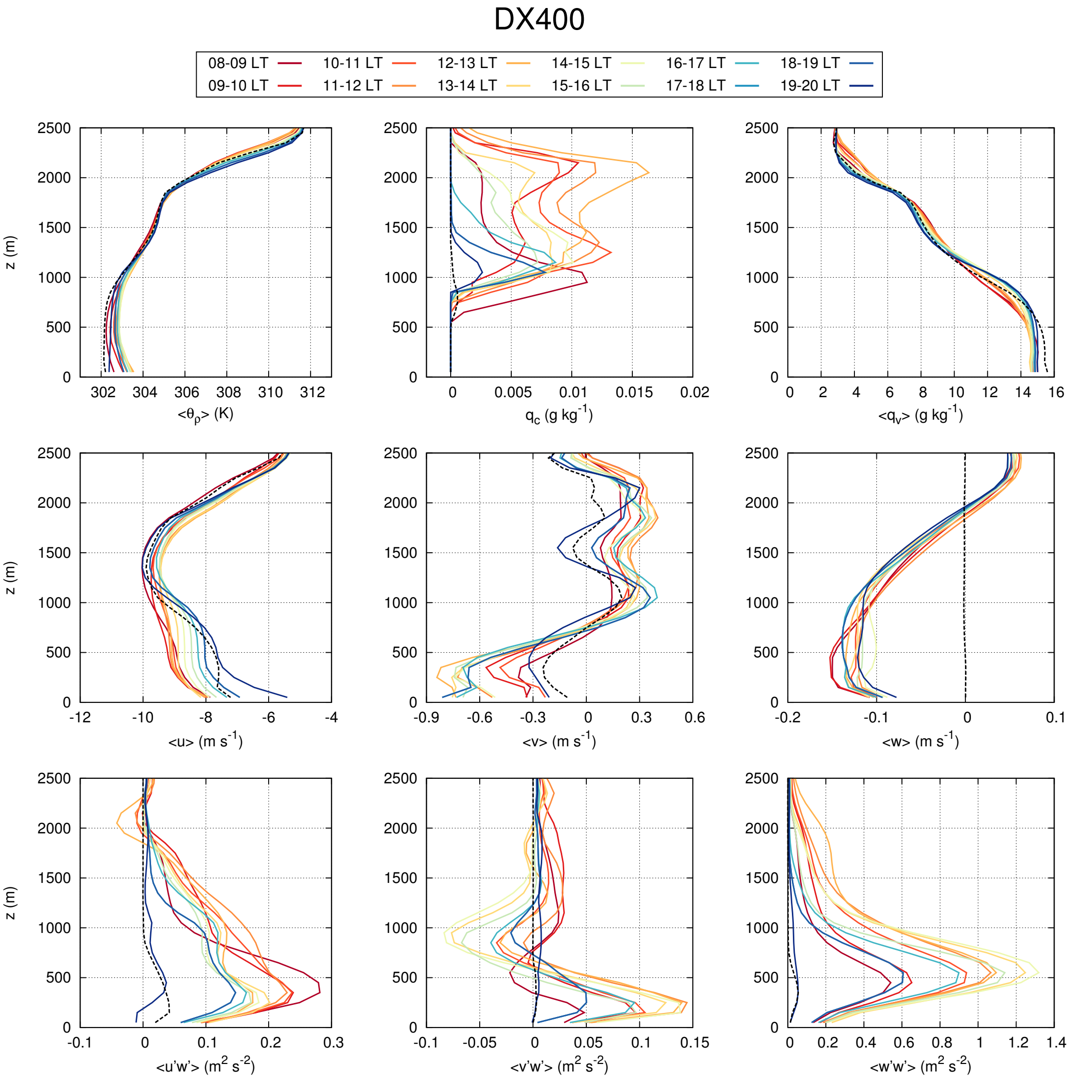

Figure B.4: Same as Fig. B.1, but for the DX400 case.

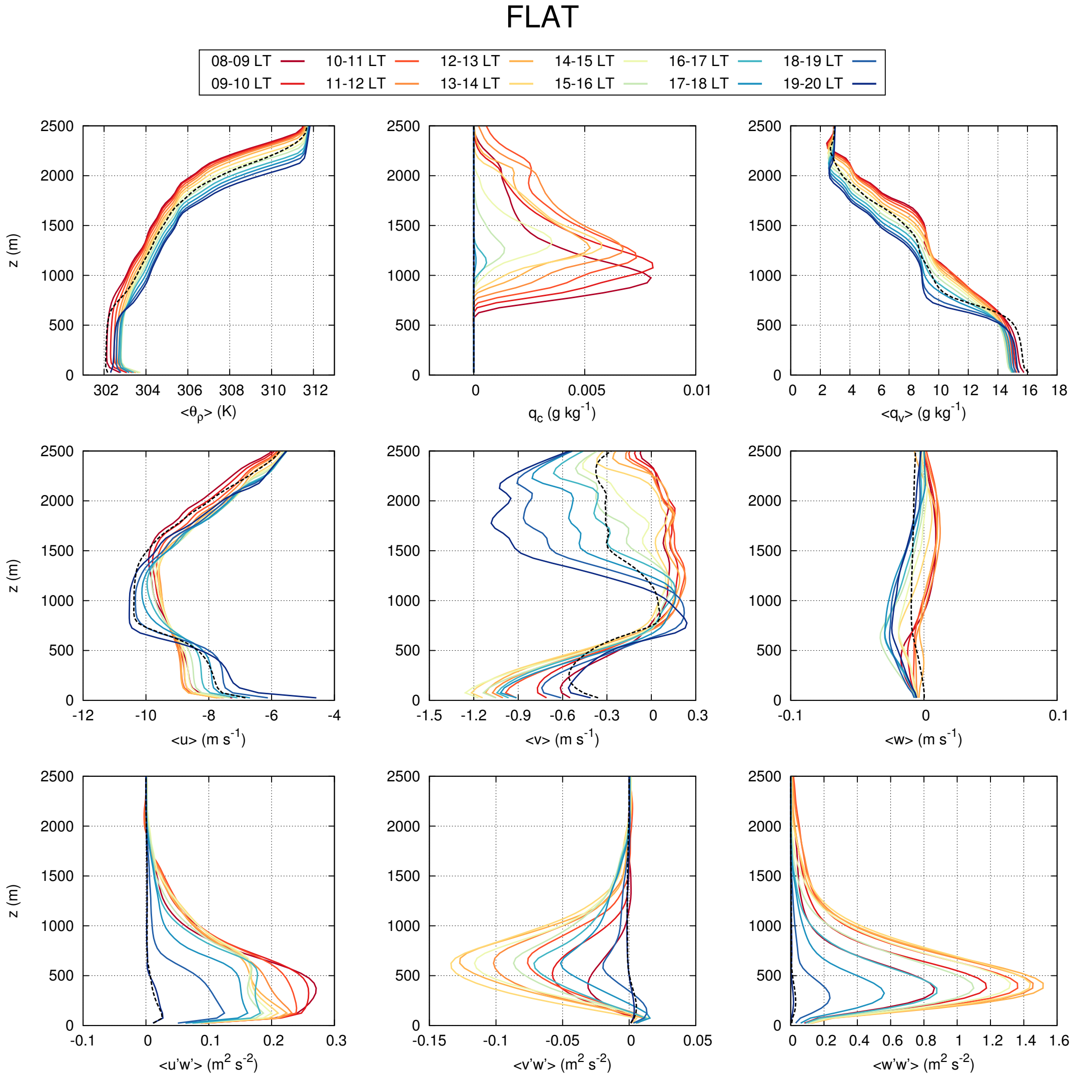

Figure B.5: Same as Fig. B.1, but for the FLAT case.

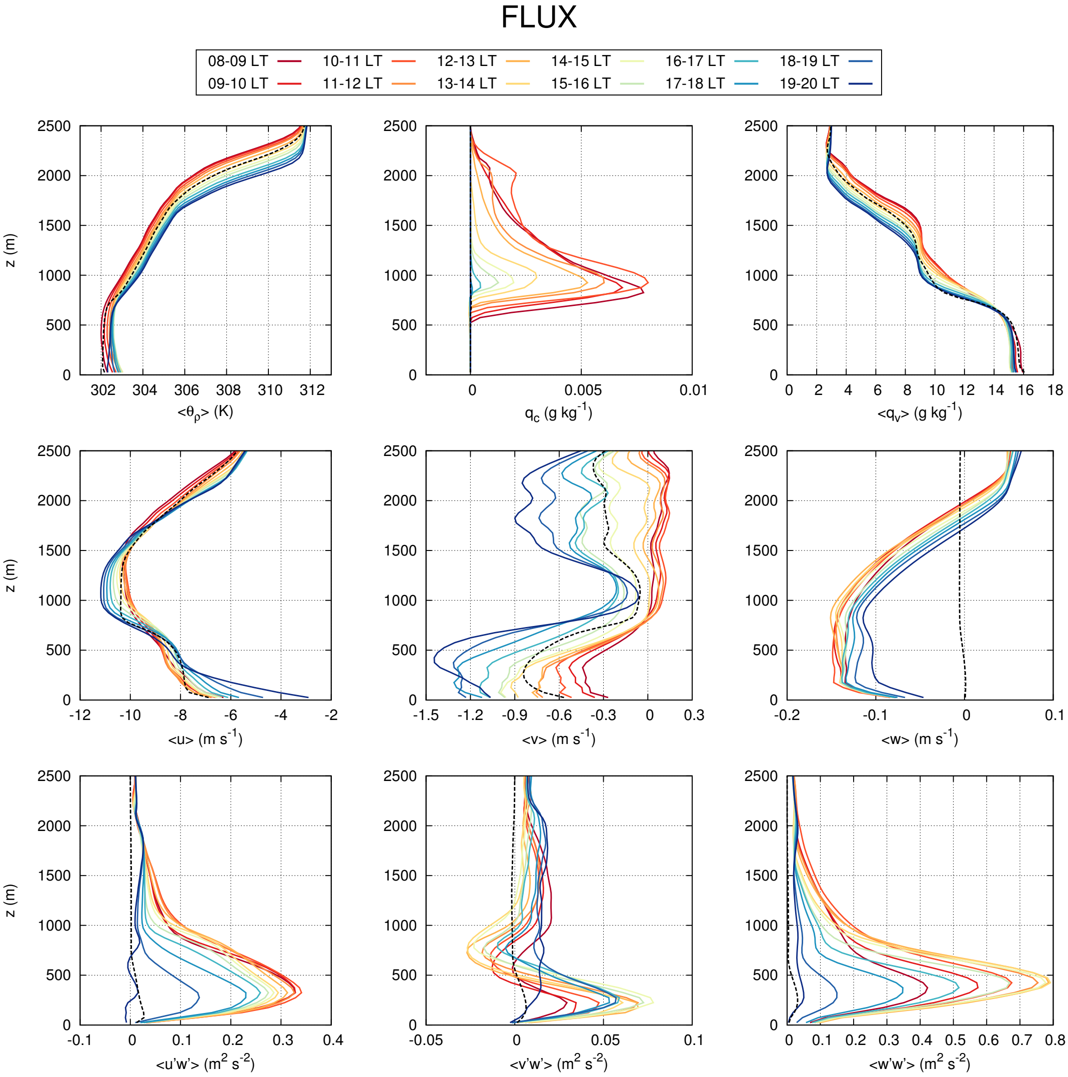

Figure B.6: Same as Fig. B.1, but for the FLUX case.

Bibliography

Ackerman, A. S., vanZanten, M. C., Stevens, B., Savic-Jovcic, V., Bretherton, C. S., Chlond, A., Golaz, J.-C., Jiang, H., Khairoutdinov, M., Krueger, S. K., Lewellen, D. C., Lock, A., Moeng, C.-H., Nakamura, K., Petters, M. D., Snider, J. R., Weinbrecht, S., and Zulauf, M. (2009). Large-eddy simulations of a drizzling, stratocumulus-topped marine boundary layer. *Mon. Wea. Rev.*, 137(3):1083–1110.

Adcroft, A., Hill, C., and Marshall, J. (1997). Rpresentation of topography by shaved cells in a height coordinate ocean model. *Mon. Weather Rev.*, 125:2293–2315.

Berger, M. and Helzel, C. (2012). A simplified h-box method for embedded boundary grids. *SIAM Journal on Scientific Computing*, 34(2):A861–A888.

Bott, A. (2008). Theoretical considerations on the mass and energy consistent treatment of precipitation in cloudy atmospheres. *Atmos. Res.*, 89:262–269.

Braun, F. J. (2002). Mesoskalige Modellierung der Bodenhydrologie. *Wiss. Berichte des Inst. f. Meteor. u. Klimat. d. Universität Karlsruhe*, 30.

Bryan, G. H. and Fritsch, J. M. (2002). A benchmark simulation for moist nonhydrostatic numerical models. *Mon. Weather Rev.*, 130:2917–2928.

Bryan, G. H., Wyngaard, J. C., and Fritsch, J. M. (2003). Resolution requirements for the simulation of deep moist convection. *Mon. Wea. Rev.*, 131(10):2394–2416.

Chen, F. and Dudhia, J. (2001). Coupling an Advanced Land Surface-Hydrology Model with the Penn State-NCAR MM5 Modeling System. Part I: Model Implementation and Sensitivity. *Mon. Weather Rev.*, 129:569–585.

Cheng, Y. and Brutsaert, W. (2005). Flux-profile relationships for wind speed and temperature in the stable atmospheric boundary layer. *Boundary-Layer Meteorol.*, 114:519–53.

Chouza, F., Reitebuch, O., Groß, S., Rahm, S., Freudenthaler, V., Toledano, C., and Weinzierl, B. (2015). Retrieval of aerosol backscatter and extinction from airborne coherent doppler wind lidar measurements. *Atmospheric Measurement Techniques*, 8:2909–2926.

Chow, F. K., De Wekker, S. F., and Snyder, B. J. (2013). *Mountain Weather Research and Forecasting*. Springer.

Deardorff, J. W. (1972). Numerical investigation of neutral und unstable boundary layers. *J. Atmos. Sci.*, 29:91–115.

DeSouza, R. L. (1972). *A study of atmospheric flow over a tropical island*. PhD thesis, Dep. of Meteorol., Fla. State Univ., Tallahassee.

Dipankar, A., Stevens, B., Heinze, R., Moseley, C., Zängl, G., Giorgetta, M., and Brdar, S. (2015). Large eddy simulation using the general circulation model icon. *Journal of Advances in Modeling Earth Systems*, pages 1–24.

Doms, G., Förstner, J., Heise, E., Herzog, H.-J., Mironov, D., Raschendorfer, M., Reinhardt, T., Ritter, B., Schrodin, R., Schulz, J.-P., and Vogel, G. (2011). *A Description of the Nonhydrostatic Regional COSMO Model*. Deutscher Wetterdienst.

Dongarra, J. J., Sorensen, I. S., and van der Vorst, H. A. (1998). *Numerical Linear Algebra for High-Performance Computers*. Society for Industrial and Applied Mathematics.

Doyle, J. D., Gaberšek, S., Jiang, Q., Bernardet, L., Brown, J. M., Dörnbrack, A., Filaus, E., Grubišić, V., Kirshbaum, D. J., Knoth, O., Koch, S., Schmidli, J., Stiperski, I., Vosper, S., and Zhong, S. (2011). An intercomparison of t-rex mountain-wave simulations and implications for mesoscale predictability. *Mon. Wea. Rev.*, 139(9):2811–2831.

Eisenstat, S. (1981). Efficient implementation of a class of cg methods. *SIAM J. Sci. Stat. Comput.*, 2:1–4.

Ellis, W. G. and Merrill, J. T. (1995). Trajectories for saharan dust transported to Barbados using stoke's law to describe gravitational settling. *J. Appl. Meteorol.*, 34:1716–1726.

Emanuel, K. A. (1994). *Atmospheric Convection*. Oxford University Press.

Engelmann, R., Ansmann, A., Horn, S., Seifert, P., Althausen, D., Tesche, M., Esselborn, M., Fruntke, J., Lieke, K., Freudenthaler, V., and Gross, S. (2011). Doppler lidar studies of heat island effects on vertical mixing of aerosols during samum-2. *Tellus*, 63B:448–458.

Esteban, M. A. and Chen, Y.-L. (2008). The impact of trade wind strength on precipitation over the windward side of the island of hawaii. *Mon. Weather Rev.*, 136:913–928.

Etling, D. (2008). *Theoretische Meteorologie: eine Einführung*. Springer, Berlin [u.a.], 3., erw. und aktualisierte aufl. edition. Dieter Etling.

Etling, D. and Brown, R. (1993). Roll vortices in the planetary boundary layer: A review. *Boundary-Layer Meteorol.*, 65(3):215–248.

Fairall, C. W., Bradley, E. F., Rogers, D. P., Edson, J. B., and Young, G. S. (1996). Bulk parameterization of air-sea fluxes for tropical ocean global atmosphere coupled-ocean atmosphere response experiment. *J. Geophys. Res.*, 101 (C2):3747–3764.

Fu, Q. and Liou, K. N. (1993). Parameterization of the Radiative Properties of Cirrus Clouds. *Journal of Atmospheric Sciences*, 50:2008–2025.

Galperin, B. and Orszag, S. A. (1993). *Large Eddy Simulations of Complex Engineering and Geophysical Flows*. Cambridge University Press.

Garstang, M., Tyson, P. D., and Emmitt, G. D. (1975). The structure of heat islands. *Rev. Geophys. Space Phys.*, 13:139–165.

Good, B., Gadian, A., Lock, S.-J., and Ross, A. (2014). Performance of the cut-cell method of representing orography in idealized simulations. *Atmospheric Science Letters*, 15(1):44–49.

Hairer, E. and Wanner, G. (2010). *Solving ordinary differential equations. II. Stiff and differential-algebraic problems*. Springer series in computational mathematics. Springer, Heidelberg, New York.

Heinze, R. (2013). *Large-Eddy Simulation von bewölkten Grenzschichten zur Untersuchung von Bilanzen der statistischen Momente zweiter Ordnung und zur Überprüfung von Turbulenzmodellen*. PhD thesis, Leibniz Universität Hannover.

Heus, T. and Seifert, A. (2013). Automated tracking of shallow cumulus clouds in large domain, long duration large eddy simulations. *Geoscientific Model Development*, 6(4):1261–1273.

Heus, T., van Heerwaarden, C. C., Jonker, H. J. J., Pier Siebesma, A., Axelsen, S., van den Dries, K., Geoffroy, O., Moene, A. F., Pino, D., de Roode, S. R., and Vilà-Guerau de Arellano, J. (2010). Formulation of the dutch atmospheric large-eddy simulation (dales) and overview of its applications. *Geoscientific Model Development*, 3(2):415–444.

Hickel, S. (2008). *Implicit Turbulence Modeling for Large-Eddy Simulation*. PhD thesis, Technische Universität München.

Hicken, J., Ham, F., Militzer, J., and Koksal, M. (2005). A shift transformation for fully conservative methods: Turbulence simulation on complex, unstructured grids. *J. Comput. Phys.*, 208:704–714.

Hinneburg, D. and Knoth, O. (2005). Non-dissipative cloud transport in Eulerian grid models by the volume-of-fluid (VOF) method. *Atmos. Environ.*, 39:4321–4330.

Holland, J. Z. and Rasmusson, E. M. (1973). Measurements of the atmospheric mass, energy, and momentum budgets over a 500-kilometer square of tropical ocean. *Mon. Wea. Rev.*, 101(1):44–55.

Horn, S. (2012). ASAMgpu V1.0–a moist fully compressible atmospheric model using graphics processing units (GPUs). *Geosci. Model Dev.*, 5:345–353.

Horn, S. (2015). *Simulations of complex atmospheric flows using GPUs - the model ASAMgpu -*. PhD thesis, University of Leipzig.

Hundsdorfer, W., Koren, B., Loon, M. V., and Verwer, J. G. (1995). A positive finite-difference advection scheme. *J. Comput. Phys*, 117:35–46.

Jähn, M., Knoth, O., König, M., and Vogelsberg, U. (2015a). Asam v2.7: a compressible atmospheric model with a cartesian cut cell approach. *Geoscientific Model Development*, 8(2):317–340.

Jähn, M., Muñoz Esparza, D., Chouza, F., and Reitebuch, O. (2015b). Investigations of boundary layer structure, cloud characteristics and vertical mixing of aerosols at barbados with large eddy simulations. *Atmospheric Chemistry and Physics Discussions*, 15(16):22637–22699.

Jebens, S., Knoth, O., and Weiner, R. (2009). Explicit two-step peer methods for the compressible euler equations. *Mon. Wea. Rev.*, 137(7):2380–2392.

Jebens, S., Knoth, O., and Weiner, R. (2011). Partially implicit peer methods for the compressible Euler equations. *J. Comput. Phys.*, 230:4955–4974.

Jimínez, P. A., Dudhia, J., Gonzalez-Rouco, J. F., Navarro, J., Montavez, J. P., and Garcia-Bustamante, E. (2012). A revised scheme for the wrf surface layer formulation. *Mon. Weather Rev.*, 140:898–918.

John, V. and Rang, J. (2010). Adaptive time step control for the incompressible navier–stokes equations. *Computer Methods in Applied Mechanics and Engineering*, 199(9,Äì12):514–524.

Kirshbaum, D. J. and Fairman, J. G. (2015). Cloud trails past the lesser antilles. *Mon. Wea. Rev.*, 143(4):995–1017.

Kirshbaum, D. J. and Grant, A. L. M. (2012). Invigoration of cumulus cloud fields by mesoscale ascent. *Quarterly Journal of the Royal Meteorological Society*, 138(669):2136–2150.

Kirshbaum, D. J. and Wang, C.-C. (2014). Boundary layer updrafts driven by airflow over heated terrain. *J. Atmos. Sci.*, 71(4):1425–1442.

Klein, R., Bates, K. R., and Nikiforakis, N. (2009). Well-balanced compressible cut-cell simulation of atmospheric flow. *Philosophical Transactions of the Royal Society of London A: Mathematical, Physical and Engineering Sciences*, 367(1907):4559–4575.

Kleissl, J., Kumar, V., Meneveau, C., and Parlange, M. B. (2006). Numerical study of dynamic smagorinsky models in large-eddy simulation of the atmospheric boundary layer: Validation in stable and unstable conditions. *Water Resour. Res.*, 42:W06D10.

Knoth, O. (2006). Compressible atmospheric modeling at all scales. In *Report No. 39/2006*. Mathematisches Forschungsinstitut Oberwolfach.

Knoth, O. and Wensch, J. (2014). Generalized split-explicit Runge–Kutta methods for the compressible Euler equations. *Mon. Weather Rev.*, 142:2067–2081.

Kong, L. C., Tuncel, L., and Xiu, N. H. (2010). The fischer-burmeister complementarity function on Euclidean Jordan algebras. *Pac. J. Optim.*, 6(2):423–440.

König, M. (2013). *Large-Eddy Simulation Modelling for Urban Scale*. PhD thesis, University of Leipzig.

Kunz, M. and Wassermann, S. (2011). Sensitivity of flow dynamics and orographic precipitation to changing ambient conditions in idealised model simulations. *Meteorol. Z.*, 20:199–215.

Lanser, D., Blom, J. G., and Verwer, J. G. (2001). Time integration of the shallow water equations in spherical geometry. *J. Comput. Phys.*, 171:373–393.

Lesieur, M., Metais, O., and Comte, P. (2005). *Large-eddy simulations of turbulence*. Cambridge University Press.

Lilly, D. K. (1962). On the numerical simulation of buoyant convection. *Tellus*, 14(2):148–172.

Lilly, D. K. (1967). The representation of small scale turbulence in numerical simulation experiments. *IBM Scientific Computing Symposium on environmental sciences*, pages 195–210.

Lock, S.-J., Bitzer, H.-W., Coals, A., Gadian, A., and Mobbs, S. (2012). Demonstration of a cut-cell representation of 3D orography for studies of atmospheric flows over very steep hills. *Mon. Weather Rev.*, 140:411–424.

Long, C. N. and McFarlane, S. A. (2012). Quantification of the impact of Nauru island on arm measurements. *J. Appl. Meteorol.*, 51:628–638.

Mahrer, Y. and Pielke, R. A. (1976). Numierical simulation of the airflow over Barbados. *Mon. Weather Rev.*, 104:1392–1402.

Maronga, B., Gryschka, M., Heinze, R., Hoffmann, F., Kanani-Sühring, F., Keck, M., Ketelsen, K., Letzel, M. O., Sühring, M., and Raasch, S. (2015). The parallelized large-eddy simulation model (palm) version 4.0 for atmospheric and oceanic flows: model formulation, recent developments, and future perspectives. *Geoscientific Model Development Discussions*, 8(2):1539–1637.

Matheou, G., Chung, D., Nuijens, L., Stevens, B., and Teixeira, J. (2011). On the fidelity of large-eddy simulation of shallow precipitating cumulus convection. *Mon. Wea. Rev.*, 139(9):2918–2939.

Matthews, S., Hacker, J. M., Cole, J., Hare, J., Long, C. N., and Reynolds, R. M. (2007). Modification of the atmospheric boundary layer by a small island: Observations from nauru. *Mon. Weather Rev.*, 135(3):891–905.

Minda, H., Furuzawa, F. A., Satoh, S., and Nakamura, K. (2010). Convective boundary layer above a subtropical island observed by c-band radar and interpretation using a cloud resolving model. *J. Meteorol. Soc. Japan*, 88(3):285–312.

Minder, J. R., Smith, R. B., and Nugent, A. D. (2013). The dynamics of ascent-forced orographic convection in the tropics: Results from Dominica. *J. Atmos. Sci.*, 70:4067–4088.

Moeng, C.-H., Dudhia, J., Klemp, J., and Sullivan, P. (2007). Examining two-way grid nesting for large eddy simulation of the pbl using the wrf model. *Mon. Wea. Rev.*, 135(6):2295–2311.

Monin, A. S. and Obukhov, A. M. (1954). Basic turbulence mixing laws in the atmospheric surface layer. *Tr. Inst. Teor. Geofiz. Akad. SSSR*, 24:163–187.

Muñoz-Esparza, D., Kosović, B., Mirocha, J., and van Beeck, J. (2014). Bridging the transition from mesoscale to microscale turbulence in numerical weather prediction models. *Boundary-Layer Meteorol.*, 153(3):409–440.

Muñoz-Esparza, D., Kosović, B., van Beeck, J., and Mirocha, J. (2015). A stochastic perturbation method to generate inflow turbulence in large-eddy simulation models: Application to neutrally stratified atmospheric boundary layers. *Physics of Fluids*, 27(3):035102. Erratum, Phys. Fluids 27, 039901 (2015).

Ng, Y., Chen, H., Min, C., and Gibou, F. (2009). Guidelines for poisson solvers on irregular domains with dirichlet boundary conditions using the ghost fluid method. *J. Sci. Comput.*, 41(2):300–320.

Noilhan, J. and Planton, S. (1989). A Simple Parameterization of Land Surface Processes for Meteorological Models. *Mon. Weather Rev.*, 117:536–549.

Nunalee, C. G., Horváth, A., and Basu, S. (2015). High-resolution numerical modeling of mesoscale island wakes and sensitivity to static topographic relief data. *Geoscientific Model Development*, 8(8):2645–2653.

Oke, T. (1973). City size and the urban heat island. *Atmospheric Environment (1967)*, 7(8):769–779.

Pielke, R. A. (1984). *Mesoscale Meteorological Modeling*. Academic Press, 2. edition.

Porté-Agel, F., Meneveau, C., and Parlange, M. B. (2000). A scale-dependent dynamic model for large-eddy simulation: Application to a neutral atmospheric boundary layer. *J. Fluid Mech.*, 415:261–284.

Prospero, J., Bonatti, E., Schubert, C., and Carlson, T. (1970). Dust in the caribbean atmosphere traced to an african dust storm. *Earth and Plan. Sci. Lett.*, 9:287–293.

Prospero, J. and Carlson, T. (1970). Radon-222 in the north atlantic trade winds: Its relationship to dust transport from africa. *Science*, 167:974–977.

Raasch, S. and Schröter, M. (2001). Palm – a large-eddy simulation model performing on massively parallel computers. *Meteorologische Zeitschrift*, 10(5):363–372.

Reitebuch, O. (2012). *Atmospheric Physics — Background, Methods, Trends. Springer Series on Research Topics in Aerospace*, chapter Wind Lidar for Atmospheric Research, page 487–507. Springer, Berlin/Heidelberg.

Riechelmann, T., Noh, Y., and Raasch, S. (2012). A new method for large-eddy simulations of clouds with lagrangian droplets including the effects of turbulent collision. *New Journal of Physics*, 14(6):065008.

Satoh, M., Matsuno, T., Tomita, H., Miura, H., Nasuno, T., and Iga, S. (2008). Nonhydrostatic icosahedral atmospheric model (nicam) for global cloud resolving simulations. *J. Comput. Phys.*, 227:3486–3514.

Savijärvi, H. and Matthews, S. (2004). Flow over small heat islands: A numerical sensitivity study. *J. Atmos. Sci.*, 61:859–868.

Schaer, C., Leuenberger, D., Fuhrer, O., Lüthi, D., and Girard, C. (2002). A new terrain-following vertical coordinate formulation for atmospheric prediction models. *Mon. Weather Rev.*, 130:2459–2480.

Scotti, A., Meneveau, C., and Lilly, D. K. (1993). Generalized Smagorinsky model for anisotropic grids. *Physics of Fluids A: Fluid Dynamics*, 5:2306–2308.

Seifert, A. and Beheng, K. D. (2006). A two-moment cloud microphysics parameterization for mixed-phase clouds. *Meteorol. Atmos. Phys.*, 92:45–66.

Siebesma, A. P., Bretherton, C. S., Brown, A., Chlond, A., Cuxart, J., Duynkerke, P. G., Jiang, H., Khairoutdinov, M., Lewellen, D., Moeng, C.-H., Sanchez, E., Stevens, B., and Stevens, D. E. (2003). A large eddy simulation intercomparison study of shallow cumulus convection. *J. Atmos. Sci.*, 60(10):1201–1219.

Siebesma, A. P. and Cuijpers, J. W. M. (1995). Evaluation of parametric assumptions for shallow cumulus convection. *J. Atmos. Sci.*, 52(6):650–666.

Skamarock, W. C., Klemp, J. B., Duda, M. G., Fowler, L. D., Park, S.-H., and Ringler, T. D. (2012). A multiscale nonhydrostatic atmospheric model using centroidal voronoi tesselations and c-grid staggering. *Mon. Wea. Rev.*, 140(9):3090–3105.

Skamarock, W. C., Klemp, J. B., Dudhia, J., Gill, D. O., Barker, M., Duda, K. G., Huang, X. Y., Wang, W., and Powers, J. G. (2008). A description of the Advanced Research WRF Version 3. Technical report, National Center for Atmospheric Research.

Smagorinsky, J. (1963). General circulation experiments with the primitive equations. *Mon. Weather Rev.*, 164:91–99.

Smith, R. B., Gleason, A. C., and Gluhosky, P. A. (1997). The wake of st. vincent. *J. Atmos. Sci.*, 54:606–623.

Smith, R. B., Schafer, P., Kirshbaum, D. J., and Regina, E. (2009). Orographic precipitation in the tropics: Experiments in Dominica. *J. Atmos. Sci.*, 66:1698–1716.

Sodoudi, S., Shahmohamadi, P., Vollack, K., Cubasch, U., and Che-Ani, A. I. (2014). Mitigating the urban heat island effect in megacity tehran. *Advances in Meteorology*, 2014:19.

Steppeler, J., Bitzer, H. W., Janjic, Z., Schättler, U., Prohl, P., Gjertsen, U., Torrisi, L., Parfinievicz, J., Avgoustoglou, E., and Damrath, U. (2006). Prediction of clouds and rain using a z-coordinate nonhydrostatic model. *Mon. Wea. Rev.*, 134(12):3625–3643.

Steppeler, J., Bitzer, H.-W., Minotte, M., and Bonaventura, L. (2002). Nonhydrostatic atmospheric modeling using a z-coordinate representation. *Mon. Weather Rev.*, 130:2143–2149.

Steppeler, J., Park, S.-H., and Dobler, A. (2013). Forecasts covering one month using a cut-cell model. *Geoscientific Model Development*, 6:875–882.

Stevens, B., Moeng, C.-H., Ackerman, A. S., Bretherton, C. S., Chlond, A., de Roode, S., Edwards, J., Golaz, J.-C., Jiang, H., Khairoutdinov, M., Kirkpatrick, M. P., Lewellen, D. C., Lock, A., Müller, F., Stevens, D. E., Whelan, E., , and Zhud, P. (2005). Evaluation of large-eddy simulations via observations of nocturnal marine stratocumulus. *Mon. Weather Rev.*, 133:1443–1462.

Stevens, B., Moeng, C.-H., and Sullivan, P. P. (1999). Large-eddy simulations of radiatively driven convection: Sensitivities to the representation of small scales. *J. Atmos. Sci.*, 56(23):3963–3984.

Stevens, B. and Seifert, A. (2008). Understanding macrophysical outcomes of microphysical choices in simulations of shallow cumulus convection. *Journal of the Meteorological Society of Japan. Ser. II*, 86A:143–162.

Straka, J. M., Wilhelmson, R. B., Wicker, L. J., Anderson, J. R., and Droegemeier, K. K. (1993). Numerical solutions of a non-linear density current: a benchmark solution and comparisons. *Int. J. Numer. Methods Fluids*, 17:1–22.

Stull, R. B. (1988). *An Introduction to Boundary Layer Meteorology*. Kluwer Academic Publishers.

Sweby, P. K. (1984). High resolution schemes using flux limiters for hyperbolic conservation laws. *SIAM J. Numer. Anal.*, 21(5):995–1011.

Tesche, M., Ansmann, A., Müller, D., Althausen, D., Mattis, I., Heese, B., Freudenthaler, V., Wiegner, M., Esselborn, M., Pisani, G., and Knippertz, P. (2009). Vertical profiling of saharan dust with raman lidars and airborne hsrl in southern morocco during samum. *Tellus B*, 61(1):144–164.

Tripoli, G. J. and Smith, E. A. (2014a). Introducing variable-step topography (vst) coordinates within dynamically constrained nonhydrostatic modeling system (nms). part 1: Vst formulation within nms host model framework. *Dynam. Atmos. Ocean*, 66:28–57.

Tripoli, G. J. and Smith, E. A. (2014b). Introducing variable-step topography (vst) coordinates within dynamically constrained nonhydrostatic modeling system (nms). part 2: Vst performance on orthodox obstacle flows. *Dynam. Atmos. Ocean*, 66:10–27.

Van Genuchten, M. T. (1980). A Closed-form Equation for Predicting the Hydraulic Conductivity of Unsaturated Soils. *Soil Sci. Soc. Am. J.*, 44:892–898.

Van Leer, B. (1994). Upwind-difference methods for aerodynamic problems governed by the Euler equations. In *Lectures in Applied Mathematics*, pages 327–336.

vanZanten, M. C., Stevens, B., Nuijens, L., Siebesma, A. P., Ackerman, A. S., Burnet, F., Cheng, A., Couvreux, F., Jiang, H., Khairoutdinov, M., Kogan, Y., Lewellen, D. C., Mechem, D., Nakamura, K., Noda, A., Shipway, B. J., Slawinska, J., Wang, S., and Wyszogrodzki, A. (2011). Controls on precipitation and cloudiness in simulations of trade-wind cumulus as observed during rico. *Journal of Advances in Modeling Earth Systems*, 3(2):1–19.

Walko, Robert L., R. A. (2008a). The ocean–land–atmosphere model (olam). part i: Shallow-water tests. *Mon. Weather Rev.*, 136:4033–4044.

Walko, Robert L., R. A. (2008b). The ocean–land–atmosphere model (olam). part ii: Formulation and tests of the nonhydrostatic dynamic core. *Mon. Weather Rev.*, 136:4045–4062.

Wensch, J., Knoth, O., and Galant, A. (2009). Multirate infinitesimal step methods for atmospheric flow simulation. *BIT*, 49(2).

Wicker, L. J. and Skamarock, W. C. (1998). A time-splitting scheme for the elastic equations incorporating second-order Runge–Kutta time differencing. *Mon. Weather Rev.*, 126:1992–1999.

Wyngaard, J. C. (2004). Toward numerical modeling in the “terra incognita”. *J. Atmos. Sci.*, 61(14):1816–1826.

Yamazaki, H. and Satomura, T. (2008). Vertically combined shaved cell method in a z-coordinate nonhydrostatic atmospheric model. *Atmospheric Science Letters*, 9(4):171–175.

Yamazaki, H. and Satomura, T. (2010). Nonhydrostatic atmospheric modeling using a combined cartesian grid. *Mon. Wea. Rev.*, 138(10):3932–3945.

Yamazaki, H. and Satomura, T. (2012). Non-hydrostatic atmospheric cut cell model on a block-structured mesh. *Atmospheric Science Letters*, 13(1):29–35.

List of Figures

List of Tables

List of Symbols

Abbreviations

ABL	Atmospheric boundary layer
AOD	Aerosol optical depth
ASAM	All Scale Atmospheric Model
BL	Boundary layer
BOMEX	Barbados Oceanographic and Meteorological Experiment
CBH	Cloud base height
CBL	Convective boundary layer
CCN	Cloud condensation nuclei
CFD	Computational fluid dynamics
CGIAR-CSI	Consortium for Spatial Information
CIMH	Caribbean Institute for Meteorology and Hydrology
CTH	Cloud top height
COSMO	Consortium for Small-Scale Modelling
CPU	Central processing unit
DALES	Dutch Atmospheric Large-Eddy Simulation
DLR	German Aerospace Center (Deutsches Zentrum für Luft- und Raumfahrt)
DWL	Doppler wind lidar
DYCOMS-II	Second Dynamics and Chemistry of Marine Stratocumulus
EOC	Experimental order of convergence
GCSS	GEWEX Cloud System Studies
GEWEX	Global Water and Energy Experiment
GPU	Graphics processing unit
HPC	High-performance computing
IBL	Internal boundary layer
ICON	ICOsahedral Nonhydrostatic
ITCZ	Intertropical Convergence Zone

LES	Large eddy simulation
LISA	Laboratoire Interuniversitaire des Systèmes Atmosphériques
LMU	Ludwig-Maximilians-Universität
LWC	Liquid water content
LWP	Liquid water path
MPI	Message Passing Interface
MPI-M	Max Planck Institute for Meteorology
NASA	National Aeronautics and Space Administration
NWP	Numerical weather prediction
OLAM	Ocean-Land-Atmosphere Model
PALM	Parallelized Large-Eddy Simulation Model
PBL	Planetary boundary layer
RAMS	Regional Atmospheric Modeling System
RICO	Rain in Cumulus over the Ocean
SAL	Saharan air layer
SALTRACE	Saharan Aerosol Long-range Transport and Aerosol-Cloud-Interaction Experiment
SCM	Source code management
SGS	Subgrid scale
TERRA_ML	Land surface parameterization scheme
TIBL	Thermal internal boundary layer
TKE	Turbulent kinetic energy
TROPOS	Leibniz Institute for Tropospheric Research
TU	Technische Universität
UBL	Urban boundary layer
UCLALES	University of California, Los Angeles Large-Eddy Simulation Code
UPR	University of Puerto Rico
UVa	University of Valladolid
VST	Variable-Step Topography
WRF	Weather Research and Forecasting

Simulation case names

BOMEX cases

DX200	Simulation with a horizontal grid spacing of 200 m
DX100	Simulation with a horizontal grid spacing of 100 m

DX050	Simulation with a horizontal grid spacing of 50 m

SALTRACE cases

REF	Simulation of the 22 June 2013 case (reference case)
INV	Simulation of the 27 June 2013 case (strong trade inversion)
NOCP	As REF, but without marine boundary layer forcing
DX400	As NOCP and with a horizontal grid spacing of 400 m
FLAT	As REF, but without island orography
FLUX	As REF, but with halved surface sensible heat flux over the island

Latin letters

a_i	Grid spacing ratio, $i \in \{1, 2\}$
c_{pd}	Specific heat capacity at constant pressure for dry air
c_{pl}	Specific heat capacity at constant pressure for liquid water
c_{pv}	Specific heat capacity at constant pressure for water vapor
C_{h}	Bulk transfer coefficient for heat
C_{m}	Bulk transfer coefficient for momentum
C_{q}	Bulk transfer coefficient for water vapor
C_{S}	Smagorinsky coefficient
c_{vd}	Specific heat capacity at constant pressure for dry air
c_{vv}	Specific heat capacity at constant pressure for water vapor
d	Wind direction
d_f	Damping layer parameter
d_w	Height above the damping layer is applied
D_{diff}	Diffusion coefficient
D_{mom}	Subgrid-scale stress for momentum
D_{pot}	Subgrid-scale stress for potential
E	Spectral energy density
Ec	Eckert number
E_d	Total energy in a dry atmosphere
E_t	Total energy
F	Face area
$\vec{g}$	Gravitational acceleration (vector)
g	Gravitational acceleration (scalar)

h	Mountain height
h_i	Virtual grid size, $i \in \{\mathrm{L}, \mathrm{C}, \mathrm{R}\}$
$\mathbf{J}$	Jacobian matrix
k	Wavenumber
k_Δ	Wavenumber at the spatial filter scale
k_K	von-Kármán-constant
L	Length scale
L_0	Latent heat of vaporization at 273.15 K
L_{00}	Latent heat of vaporization at 0 K
L_v	Latent heat of vaporization
N_{CCN}	Number concentration of CCN
N_{c}	Number concentration of cloud droplets
N_{r}	Number concentration of raindrops
n_i	Component of the normal vector, $i \in \{x, y, z\}$
p	Air pressure
p_0	Reference air pressure
Pr	Turbulent Prandtl number
R_d	Gas constant for dry air
R_v	Gas constant for water vapor
Ri	Richardson number
t	Time
t_p	Perturbation time
Q_{dif}	Direct radiative flux
Q_{dir}	Diffuse radiative flux
Q_{lat}	Latent heat flux
Q_{sens}	Sensible heat flux
$\vec{q}_\phi$	Subgrid scale term for a given scalar (vector)
q_{c}	Mass ratio of cloud water
q_{d}	Mass ratio of dry air
q_{l}	Mass ratio of liquid water
q_{r}	Mass ratio of rain water
q_{v}	Mass ratio of water vapor or specific humidity
r_{c}	Mixing ratio of cloud water
r_{d}	Mixing ratio of dry air
r_{l}	Mixing ratio of liquid water
r_{r}	Mixing ratio of rain water
r_{v}	Mixing ratio of water vapor

$\mathbf{S}$	Matrix in Rosenbrock method
S_ϕ	Source term of a scalar quantity
T	Absolute temperature
T_{soil}	Absolute soil temperature
U	Horizontal wind speed
u	Zonal wind component
u_g	Zonal component of geostrophic wind
V	Volume
V_{virt}	Virtual volume
$\vec{V}$	Density weighted three-dimensional velocity vector
$\vec{v}$	Three-dimensional velocity vector
v	Meridional wind component
v_g	Meridional component of geostrophic wind
W_{eff}	Effective soil wetness
W_{res}	Residual water content
W_{soil}	Volumetric water content
w	Vertical wind component
z	Height
z_0	Roughness length
z_{i}	Boundary layer height
$z_{\mathrm{inv,b}}$	Bottom altitude of trade-wind inversion
$z_{\mathrm{inv,t}}$	Top altitude of trade-wind inversion

Greek letters

α_1, α_2	Coefficients in Eq. (2.6)
Γ	Perturbation time scale
γ	Parameter in Eq. (2.19)
$\overline{\Delta}$	Length scale
Δ	Grid spacing
Δx	Grid spacing in x-direction
Δy	Grid spacing in y-direction
Δz	Grid spacing in z-direction
θ	Potential temperature
θ_v	Virtual potential temperature
θ_ρ	Density potential temperature

κ	Poisson constant
κ_m	Poisson constant for a moist and cloudy atmosphere
κ_{soil}	Hydraulic conductivity
λ	Wavelength
λ_{h}	Heat conductivity
ν_t	Viscosity
ρ	Total air density
ρ_{c}	Density of cloud water
ρ_{d}	Density of dry air
ρ_{l}	Density of liquid water
ρ_{r}	Density of rain water
ρ_{v}	Density of water vapor
ρ_{W}	Mass density of water
$\vec{\tau}$	Subgrid-scale stress term for momentum (vector)
τ	Time period
τ_{ij}	Subgrid-scale stress term for momentum (scalar)
Φ	Momentum
ϕ	Scalar quantity
ϕ_{BLT}	Boundary layer tracer
ϕ_{SDT}	Saharan dust tracer
$\Psi_{\mathrm{m,h}}, \phi_{\mathrm{m,h}}$	Integrated similarity functions
Ψ_{soil}	Matric potential
$\vec{\Omega}$	Angular velocity vector of the earth
ω	Angular velocity of the earth

Danksagung

Als erstes bedanke ich mich bei Prof. Dr. Ina Tegen für die Bereitstellung und die Möglichkeit der Durchführung der Arbeit an diesem sehr interessanten Thema. Bedanken möchte ich mich auch bei Prof. Dr. Bjorn Stevens für die Übernahme des Korreferats.

Einen besonderen Dank möchte ich Dr. Oswald Knoth aussprechen, der mich in meiner wissenschaftlichen Laufbahn bereits seit meiner Diplomarbeit begleitet und jederzeit als erster fachlicher Ansprechpartner zur Verfügung stand.

Meinen Kollegen der Abteilung Modellierung am Institut für Troposphärenforschung danke ich für die allzeit sehr angenehme Arbeitsatmosphäre.

Die rechentechnisch aufwändigen Simulationen, die in diese Arbeit einflossen, wurden am *Zentrum für Informationsdienste und Hochleistungsrechnen* (ZIH) der TU Dresden durchgeführt. Für die schnelle Lösungsfindung bei technischen Problemen danke ich den Mitarbeitern des ZIH.

Weiterhin möchte ich mich bei den Kollegen der Arbeitsgruppe *Bodengebundene Fernerkundung* bedanken, insbesondere Dr. Albert Ansmann, Moritz Haarig und Dr. Dietrich Althausen, welche mir die Teilnahme an der dritten SALTRACE-Kampagne auf Barbados ermöglichten.

Natürlich gilt mein Dank auch allen Personen aus meinem privaten Umfeld, die mir stets Unterstützung und das nötige Vertrauen entgegengebracht haben.

Publikationen

Journale

Jähn, M., Muñoz-Esparza, D., Chouza, F., Reitebuch, O.: Investigations of Boundary Layer Structure, Cloud Characteristics and Vertical Mixing of Aerosols at Barbados with Large Eddy Simulations, *Atmos. Chem. Phys. Discuss.*, 15, doi:10.5194/acpd-15-22637-2015, 22637–22699, 2015.

Jähn, M., Knoth, O., König, M., Vogelsberg, U.: ASAM v2.7: a compressible atmospheric model with a Cartesian cut cell approach, *Geosci. Model Dev.*, 8, 317–340, doi:10.5194/gmd-8-317-2015, 2015.

Jähn, M., Wolke, R., Sändig, B.: Detection of odor sources and high concentrations of pollutants in the Ore Mountains by modeling of air mass paths. *Meteorol. Z.*, 22(2), 213–220, doi:10.1127/0941-2948/2013/0389, 2013.

Sonstige Publikationen

Ansmann, A., Tegen, I., Müller, T., Althausen, D., Kristensen, T. B., Engelmann, R., Fomba, K. W., Haarig, M., Heinold, B., Hermann, H., **Jähn, M.**, Kanitz, T., Klepel, A., Macke, A., Rittmeister, F., Skupin, A., Wiedensohler, A.: Saharan Dust Long-range Transport and Aerosol-Cloud-Interaction Experiment SALTRACE: Observations and Modelling. *Biennial Report 2012/2013*, Leibniz Institute for Tropospheric Research, 2014.

Jähn, M., Wolke, R., Sändig, B., Renner, E.: Detection of odor sources and high concentrations of pollutants in the Ore Mountains by modeling of the air mass paths. *Biennial Report 2010/2011*, Leibniz Institute for Tropospheric Research, 2012.